Development of Novel Dynamic Indentation Techniques for Soft Tissue Applications

by

Asha Balakrishnan

B.S., University of Illinois (1997)
S.M., Massachusetts Institute of Technology (1999)

Submitted to the Department of Mechanical Engineering
in partial fulfillment of the requirements for the degree of

Doctor of Philosophy in Mechanical Engineering

at the

MASSACHUSETTS INSTITUTE OF TECHNOLOGY

September 2007

Signature of Author ....
Department of Mechanical Engineering
31 August 2007

Certified by ....
Simona Socrate
Assistant Professor of Mechanical Engineering
Thesis Supervisor

Accepted by ....
Lallit Anand
Chairperson, Department Committee on Graduate Students

Development of Novel Dynamic Indentation Techniques for Soft Tissue Applications

by

Asha Balakrishnan

Submitted to the Department of Mechanical Engineering
on 31 August 2007, in partial fulfillment of the
requirements for the degree of
Doctor of Philosophy in Mechanical Engineering

Abstract

Realistic material models to simulate the behavior of brain tissue at large deformations and high strain rates are necessary when designing equipment to protect against ballistic impacts. Acquiring experimental data for brain tissue response is critical to developing appropriate models. Current in vivo and in situ procedures for testing the material behavior of soft tissues are dominated by indentation techniques. The major challenge for this testing configuration is in finding a unique solution to the "inverse problem" i.e., obtaining material properties that are uniquely defined by the indentation force-displacement response. Much of the information related to the interplay between shear and bulk compliance in the deformation field beneath the indenter is lost when capturing the single force-displacement output.

To address this challenge, we propose a material testing technique that follows the well-proven path of conventional indentation methods, but also enriches the signal by acquiring displacement data for an offset, passive surface tracking sensor. We present the results of a finite element (FE) study to demonstrate that the addition of a secondary sensor can help to discern between materials with varying degrees of compressibility. To this end, a large displacement in vivo dynamic indentation surface tracking (DIST) tool was designed and manufactured. This tool incorporates the secondary sensor concept to measure the force-displacement response of brain tissue at strain rates up to 1000%/s. The technique is applied in vitro to measure the response of porcine brain tissue. To select an appropriate constitutive framework for porcine brain tissue in vitro, uniaxial compression tests measuring the corresponding lateral stretch response are performed. A three-dimensional large deformation constitutive model for brain tissue is developed. The model accounts for the observed features of the material response including non-linearity, conditioning, hysteresis, and strain-rate dependence. The model is incorporated into an FE simulation of the brain indentation tests performed with the DIST tool. The effectiveness of the DIST as a material-testing tool is assessed.

Thesis Supervisor: Simona Socrate
Title: Assistant Professor of Mechanical Engineering

Contents

List of Figures

List of Tables

Acknowledgements

We are not able to accomplish anything in a vacuum; without the help, support or guidance of others. I have been fortunate enough to have many people help me get here. To my labmates and colleagues: Petch, Tim, Bruce, Mike, Amy, Kristin, Anastassia and Una for always being there to listen and for keeping the lab environment lively and enriched. I have learned so much from them. I am particularly grateful to Thibault, who put an unbelievable amount of effort into helping me finish the work towards the end. I want to thank and acknowledge the help of Pierce in the Mechanics lab for always being available to lend a hand, and of Peter in the Central Machine Shop at MIT for teaching me the essence of design for manufacturing. To my colleagues at the Brigham and Women's hospital, Dan Kacher and Florin Talos, for teaching me about the medical aspects of this work, and providing a venue for the experiments to be carried out. Professor Alex Slocum was my enabler; he convinced me and paved the way for me to come back to MIT for a PhD, he encouraged and inspired me to keep going, and he taught me many lessons in not only engineering principles, but life principles that guide me today. My advisor, Professor Simona Socrate, is a person who cares for students far more than any professor I have met. She spent many hours teaching me and assisting me in this work. For all her help with my work and life outside work, I am truly thankful. To my friends and family, for showing their support in countless ways. To my parents, for encouraging me to keep going, and for their patience and unwavering support throughout this process. My father inspired me to be an engineer many years back and this thesis is dedicated to him for sowing the seed of curiosity in me at an early age. To Manish, who has stood by me through many of this year's trials and tribulations. His support and encouragement towards the end really helped me complete the PhD. At a particularly difficult time in my life, I feel blessed to have had so many people came together to help me. And to Sri Sathya Sai Baba, my spiritual teacher, who has taught me and continues to teach me the values by which I live.

Chapter 1

Introduction

1.1 Thesis objective and outline

The brain is a complex structure that exhibits both solid and fluid -like behaviors at the macroscopic scale. Characterizing the material behavior of brain tissue remains challenging because the requisite model must encompass the tissue response for relatively large deformations and frequency ranges. This nonlinear characterization is particularly pertinent for brain injuries sustained by dynamic loads in which criteria for damage and injury thresholds for the brain are of great interest. The focus of this thesis in briefly described in the following outline.

I. Thesis background and motivation

Chapter 2 develops the premise and motivation for this work. A literature review of the mechanical response and properties of brain tissue is presented. Characterizations of the nonlinear hyper- viscoelastic nature of this material will be included.

II. Development a portable in vivo dynamic indentation tool to measure properties of soft tissues

In Chapter 3, the development of several in vivo tools are discussed. In the initial phases of this project, a tool was developed to perform in vivo force-displacement experiments adapting procedures consistent with neurosurgery. To assess the high rate response of soft tissues, an in vivo spring-loaded one-shot tool was also developed. Lastly, an oscillating dynamic indentation tool capable of large deformations and high strain rates was developed. Although the other tools were designed and developed, the focus of subsequent work was on the portable in vivo dynamic indentation tool. Further development and troubleshooting of the other tools will be suggested future work.

III. Adaptation of designed tool with additional sensors to improve the characterization of material behavior

Chapter 4 describes the proof-of-concept of incorporating additional surface tracking sensors to characterize the behavior of soft tissues when the material cannot be removed from their original configuration (i.e. in vivo). Using three-dimensional finite element simulations, these additional sensors are shown to enrich the response by elucidating trade-offs between the bulk and shear responses.

IV. Validation of tool design with additional sensors on stable tissue-like simulants

In Chapter 5, the validation of the in vivo dynamic indentation tester is presented. After the modifications necessary for the addition of the secondary sensors are made, the concept presented in Chapter 3 is validated on stable tissue-like silicon gel simulants. The sensor characteristics (location, range of motion, stiffness, frequency response) are demonstrated and optimized for an in vivo testing configurations.

V. In vitro experimentation of large deformation mechanical response of porcine brain tissue

Chapter 6 describes efforts undertaken to gain insight into the mechanical response of porcine brain tissue. Because in vivo studies are costly and challenging to arrange, initial investigations to understand the specific features of the in vitro mechanical response to uniaxial unconfined compression and indentation are performed. Indentation experiments using the secondary sensor are also conducted. The results of these studies are presented.

VI. Determination of an appropriate constitutive model of porcine brain tissue

In this chapter, the constitutive framework for the mechanical behavior of in vitro porcine brain tissue is presented. Features of the experimental response such as nonlinearity, hysteresis, conditioning, and strain rate effects are considered when developing this model. A model, noted as the pre-conditioned model, that captures the nonlinearity, time dependence and strain rate dependence is first presented. Another model to capture the conditioning response of the material is placed in parallel with the first model. The model fit to the experimental unconfined compression and indentation results is presented and discussed. The indentation experiment with secondary sensor conducted in Chapter 6 is simulated. The displacement of the secondary sensor is predicted and compared with the experimental results.

Chapter 2

Background and Motivation

Understanding the mechanical behavior of brain tissue is of great interest for the purpose of injury simulation, surgical simulation, and medical diagnosis. Obtaining these properties is a significant challenge due to the mechanical and geometric nonlinearities, multi-constituent heterogeneity, viscoelastic nature, and poorly defined boundary conditions of soft tissues. Physically realistic models of brain tissue are used to simulate the effects of crash and projectile impacts upon body armor. New technologies for armor are being developed, but the mechanical behavior of brain tissue under high rate high deformation loading must be better understood. Additionally, surgical simulation and image-guided surgery strive to enhance the surgeon's capability to utilize advances in medical imaging and reduce the degree to which the surgery is invasive. During the last decade, physically realistic models for surgical planning have gained more favor and created a need for determining material properties of tissue.

Improvements in the understanding of soft tissue material behavior is undergoing rapid evolution; however major problems still remain. Due to cell death and lack of perfusion, excised tissue (in vitro) behaves differently from living tissue (in vivo) [26][49]. Limited access to living tissue, particularly soft tissue, catalyzes the need for accurate correlation between in vivo testing and in vitro testing. This also suggests that in vivo studies of soft tissues must be conducted; however to obtain useful parameters, finite element (FE) models must also be developed.

2.1 Traumatic brain injury

Traumatic brain injury (TBI) is a of the leading causes of death and disability among young people in the developed world [85]. In the United States, TBI is responsible for 500,000 people being hospitalized each year with 2 million reported cases worldwide per year [86]. In the western hemisphere, TBI represents 15% of all fatalities and disabilities [61]. According to Finfer *et al.*, this proportion will increase to 20% by 2020 and TBI will become the third leading cause of whole-population death and disability [22]. Head injuries largely result from falls, sporting accidents, and automobile accidents. In combat/blast-related situations, injuries most often occur due to a blast wave from detonated improvised explosive devices (IED) [77]. Such events are not well-documented or understood, and while ballistic helmets offer protection, injuries to the skull and brain matter still occur.

Mechanisms that cause TBI are largely unknown; investigations necessary to understanding links between physiological damage, physical damage and neurological impairments are ongoing. Taylor *et al.* [77] asserts that distinct cell damage mechanisms can occur when the cells are subjected to isotropic stress (i.e., pressure) and/or shearing stress. In other words, internal cell damage occurs when tensile and compressive pressures impose a volumetric change in the cell. The second mechanism is related to the shearing stress that causes the tearing of cellular membranes in neurons.

Gurdjian *et al.* [28] pioneered the field of head injury biomechanics by creating tolerance curves of acceleration and intracranial pressure. Through this work, the Wayne State University Tolerance Curve (WSUTC) was proposed and the Head Injury Criteria (HIC) was developed. Measures taken to improve protective head gear are typically evaluated against a measurement of HIC. HIC is said to be proportional to the intracranial pressure, shear stress, and skull von Mises stress [68]. However, this method has been criticized due to its limited ability to predict the probability of brain injury [87]. It is suggested that the specific deformation of brain tissue and the relative motion of the brain with respect to the skull would be a better means of assessing head protection [1]. In order to better understand brain injury biomechanics, mathematical models are employed. Over the past few years, several three-dimensional FE models of the human head have been extensively used to understand and to predict head injuries [1][3][14][37][68][76][90][91]. Ruan *et al.* and Zhou *et al.* focused on the deviatoric response as an injury indicator for diffuse axonal injury (DAI) [68][91]. Zhang *et al.* used head collision data to validate the FE model. Shear stresses around the brain stem were discovered to be a predictor for concussions. Through this work, a new brain injury tolerance level was suggested [89]. Klevien *et al.* developed a detailed and parameterized FE model of the human head, and used it to evaluate the effects of head size, brain size and impact directions [37]. Brain injuries are clearly associated with the large strains that result when shearing or tearing of biological tissue occurs. A major limitation that impedes the progress of FE modeling for dynamic applications is the lack of data on brain tissue behavior tested at large strains and high strain rates. To improve FE modeling of head injury and to develop effective brain injury prevention systems, better knowledge of the complex material properties and interface conditions of the human head, as well as more experimental data relating to brain motion and large strain deformation are needed.

2.2 Surgical simulation

Modeling the deformation of human organs for surgical simulation systems is a challenging undertaking. Not only is very little known about the physical properties of general human tissue but in addition, most conventional modeling techniques are not applicable because of the timing requirements of simulation systems. In the fields of elasticity and related modeling paradigms, the main interest has been the development of accurate mathematical models [11]. There has been much effort spent towards the development of image-guided surgical techniques in the area of minimally invasive neurosurgery over the past ten years. A major challenge in the field of neurosurgery is minimizing the removal of healthy tissue and maintaining the integrity of critical anatomical structures while resecting a tumor [83]. Algorithms to create enhanced visualizations of the tumor and critical brain structures by aligning high-resolution preoperative images (MRI, CT) with intraoperative images of the brain during surgery are being developed and refined to improve the arena of neurosurgical simulation.

Nimsky *et al.* observed that the cortical surface of the tumor margin was displaced up to 24mm in 2/3 of the cases studied [57]. These large displacements clearly exceed the accuracy desired for image-guided surgical procedures. Nabavi *et al.* [54] demonstrated that shifts of the tumor margins and cortical surfaces occur over time during the resection procedure. In order to observe these changes in real-time, intraoperative imaging techniques are employed in the form of either ultrasound (US), magnetic resonance (MR), computed tomography (CT) or stereoscopic microscopy [42]. These studies have made it clear that there is value in using biomechanical models to improve the utilization of intraoperative data [16][18]. Warfield *et al.* [83] present an analysis of inferring volumetric brain deformation through biomechanical simulations with boundary conditions established by matching the brain surface with the tumor margins. Predicted volumetric shifts of the brain are based on the form and accuracy of the material model applied to the simulation. Clearly, the advancement of the work in the field of surgical simulation is highly dependant on the accuracy of the biomechanical simulations that are predicting deformations. In the specific case of neurosurgery, accurate brain tissue properties are critical to improving FE models and simulations.

2.3 Anatomy of the human head

To aid in the understanding of traumatic brain injuries and surgical simulation, it is useful to present a basic anatomical and physiological background of the human head. The head consists of the facial portion on the anterior side and cranial skull that covers the brain on the posterior side. Between the scalp and the skull, there is a loose connective-tissue layer and a fibrous membrane surrounding the bones. Moving inwards, three membranes encase the brain: the dura mater, the arachnoid, and the pia mater. These membranes are collectively called the meninges, and are separated from each other by subdural and subarachnoidal spaces, respectively, and are filled with cerebrospinal fluid (CSF). This fluid is understood to play a role in absorbing impact to the head, and the presence of this fluid suggests that material behavior is partially governed by the permeability of the material. The water content of brain tissue is nearly 80%, and therefore the brain is often times modeled as nearly incompressible [73].

The brain consists largely of a combination of white matter and gray matter. Gray matter is primarily composed of nerve cell bodies (neurons) and glial cells. White matter is composed of myelinated nerve cells (axons). Blood vessels intertwine throughout the tissue. The brain is structurally separated in several parts. The most important ones are the cerebrum, the

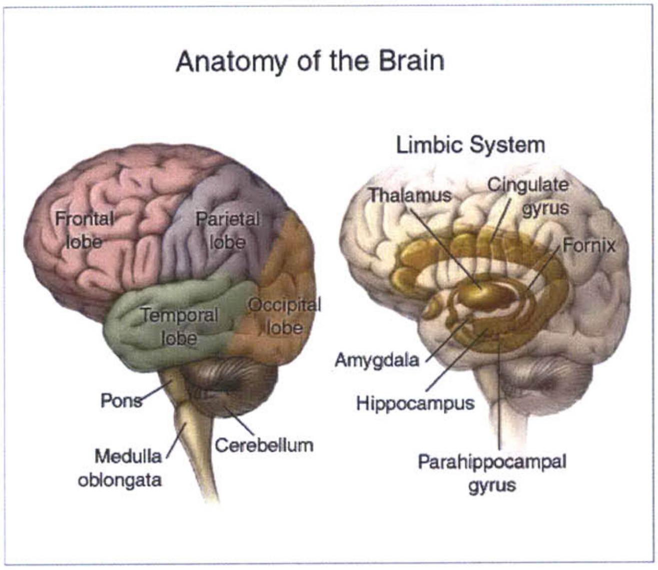

Figure 2-1: Basic anatomy of brain tissue

cerebellum, and the brain stem which consists of midbrain, pons and medulla oblongata. The cerebrum is divided into four different areas: the frontal lobe, the parietal lobe, the occipital lobe, and the temporal lobe as shown in Figure 2-1. Gray matter is often assumed to be isotropic in nature. White matter is often considered anisotropic as the myelinated axons of white matter demonstrate prominent directional differences [66]. However, the approximation of isotropy existing throughout the brain tissue is adopted by many investigators [17][20][49][70], especially when treating the white matter and gray matter as a mixed homogenous material.

2.4 Literature review of brain tissue properties

The mechanical response of brain tissue has been investigated for the past several years. Investigators have attempted to understand the mechanical response of brain tissue through variations and combinations of four different experimental parameters: loading configurations (compression, shear, indentation, tension); loading histories (cyclic, stress relaxation, creep); states (in vitro, in situ, in vivo); and testing regimes (high strain/low strain rate or low strain/high strain rate). Each test method is adept at revealing certain information about the material behavior of brain matter, but is not capable of fully characterizing brain tissue response. In the following section, a comprehensive literature review of experiments on brain tissue materials is discussed. Table 2.1 provides and overview of brain property experiments and their proposed constitutive models.

2.4.1 Testing brain behavior in shear

Much of the in vitro brain tissue work has been performed in the shear loading configuration [2][6][10][65][66][75][78]. Reported properties of brain tissue vary more than an order of magnitude. These differences may be attributed to testing at various post mortem times, testing different donor species, anisotropy of the tissue, and the non-homogenous nature of the brain. Animal tissue is often used as a substitute for human brain tissue. It is more easily available and can be tested at shorter post mortem times. Porcine and bovine tissue are well accepted animal models for human brain tissue [17][56].

Galford and McElhaney performed a viscoelasticity study of the scalp, brain, and dura to understand the time-dependence of the various major components of the head [24]. Fallstein and Hulce performed one of the first experiments to study mechanical phenomena associated with impact to the head [21]. Nicolle *et al.* [56] performed a series of in vitro experiments over a large frequency range. This work compared human brain tissue to that of porcine tissue, and concluded that there exists no significant difference between the two, thereby establishing porcine brain tissue as an acceptable model for human brain tissue. In addition, this group performed high frequency rheometry experiments in frequencies ranging from 0.1Hz to 10000Hz. The high frequency experiments were performed at low strain, and conversely the low frequency was performed at high strain. Typical frequencies below 1000Hz are associated with traffic accidents [3][65]. For non-penetrating ballistic impacts, frequencies over 1000Hz are assumed [8][30]. Nicolle *et al.* [56] also observed the influence of different test parameters: degeneration effect, slipping effect, precompression effect, and shearing plane effect.

Table 2.1: Literature review of brain tissue testing

Author	Mode	Strain level	Strain rate	Sample size	Species	Post-mortem Time (h)	Model
Estes and McElhaney	UCC	0.37	0.08 - 40 1/s	d = 12.6mm h = 10.9mm	Human (mixed matter)	6 - 10	
Shuck and Advani	OS	1.30%	5 - 350Hz	d = 12.6mm h = 3.1 - 12.6mm	Human (white and gray matter)	few	Four Parameter Viscoelastic
Mendis et al.			based on Estes and McElhaney (1970)				QLV
Donnelly and Medige	Shear	100%	0 - 90 1/s	d = 12.4 - 19mm h = 5.3 - 26.4mm	Human (mixed matter)	48	Power law based on standard linear solid
Miller and Chinzei	UCC	0.35	0.64e-5 - 0.64 1/s	d = 30mm h = 13mm	Porcine (mixed matter)	12	QLV
Thibault and Margulies	OS	2.5 - 5%	20 - 200Hz	d = 10 - 12mm h = 1 - 2mm	Porcine Front cerebrum	3	
Darvish and Crandall	OS	10%	0.5 - 2000Hz	d = 15 - 20mm h = 4.8mm	Bovine (mixed matter)	24	Multiple hereditary integral QLV
Bilston et al.	OS	0.10%	0.01 - 10Hz	d = 20mm h = 2mm	Bovine Corpus callosum	8	Differential form
Prange and Margulies	Shear Relaxation	5 - 100%	rise time = 0.05s	l = 10mm, w = 5mm h = 1mm	Porcine (white and gray matter) Human (gray)	5 3	QLV
Miller and Chinzei	Tension	1.3	0.64e-2 - 0.64 1/s	d = 30mm h = 10mm	Porcine (mixed matter)	12	QLV
Brands	OS, TTS	1%	1 - 1000Hz	d = 12mm h = 1-2mm	Porcine (mixed matter)	4	Differential form
Gefen and Margulies	Indentation relaxation	depth = 4mm	1mm/s - 3mm/s	N/A	Porcine in vivo / in situ		Stress relaxation function
Nicolle et al.	OS						

OS = Oscillatory shear
UCC = Unconfined compression

2.4.2 Compression testing

Galford and McElhaney performed a series of creep and stress relaxation tests in compression of monkey and human tissue [24]. This study was the basis for much of the subsequent work on brain tissue. Miller *et al.* has performed unconfined compression and tension studies in vitro [49][50]. The compression and tension tests were done at strain rates between 1e-5 s^{-1} to 1e0 s^{-1}. In compression, porcine tissue samples were tested in the large strain regime ($\varepsilon_{\max}$ =0.64) in loading. Unloading data was not given, however nonlinearities in the large strain response were observed. Incompressibility of the material is often assumed in models of brain tissue [20][45][64]. Cheng and Bilston investigated the behavior of brain tissue white matter under a stress relaxation loading input at three different rates [13]. To understand cerebrospinal fluid flow in the brain, they determined the permeability of the white matter and modeled the response of brain tissue white matter with a poroviscoelastic model.

2.4.3 In vitro vs. in vivo behavior

In the past few decades, some studies have conducted to understand differences between living and non-living tissue [26][51][50][56]. In vitro testing is the most accessible method to determining the material response of tissues; however research suggests that there are significant differences between in vitro and in vivo behavior. Gefen and Margulies [26] showed that there is a definite preconditioning effect between the first and fifth/sixth cycles of testing. In addition, it was found that there was a significant difference between the long-term shear modulus of in vivo and in situ stress relaxation curves, which suggest that at longer time constants in situ or in vitro tests do not compare well with the behavior of living tissue. Miller also reported compression tests performed in vitro resulted in a 30% decreased stiffness compared to indentation tests performed in vivo [51]. Neither of these studies show the unloading behavior of the material. Both perform stress relaxation tests; however, hysteresis effects of the unloading phase were not captured.

2.4.4 Effect of region and post-mortem time

A few studies on the differences between white matter and grey matter material properties have been conducted. Prange and Margulies [66] showed that the difference in mechanical response between white matter from the corpus callosum and grey matter from the thalamus region may reach up to 30%. In the same study, human samples obtained from temporal lobectomies performed on epileptic patients, were on average 29% stiffer than porcine samples. Moreover, they reported that differences attributed to anisotropy of grey matter and white matter were up to 10% and up to 50%, respectively. In this work, the effect of white and grey matter are not separated as the investigation aims to understand the global response to the tissue as a whole.

The differences in the aforementioned researchers' work are significant. Some of these differences may be attributed to variations post-mortem time of assessing the tissue. Metz *et al.* [46] have reported a 30-70% decrease in tissue response to the inflation of a balloon catheter between live samples and samples taken 3/4 hour post-mortem. McElhaney *et al.* [43] have reported no significant changes in sample properties up to 15 hours post-mortem, and Nicolle *et al.* [56] have reported only a 6% increase of shear modulus between samples measured at 24 and 48 hours post-mortem. Many authors suggest that the tissue would degenerate with increasing post-mortem time due to various reasons (e.g., autolytic processes, completion of rigor mortis, osmotic swelling, etc.). Due to interspecies and protocol testing differences, there are discrepancies in the literature regarding amplitude and frequency-dependence of the shear moduli in the linear field.

Most of the work performed on brain tissue has been conducted in the linear viscoelastic regime at high frequencies or at larger deformations at low strain rates. More testing needs to be conducted in the regime of large deformation at high strain rates. The work performed in this thesis aims to address this void in the literature. In addition, much of the work previously done on brain tissue is tested only in one mode of deformation. Often times in the case of unconfined compression only the loading data is recorded and the unloading data is ignored, thus losing valuable information as to the time dependent characteristics of the material. While it is widely accepted that brain tissue exhibits strain-rate dependence, efforts to quantify this dependence need to be investigated. This is especially the case if the characterization at the relatively lower strain rates is to be extrapolated into strain rate regimes consistent with those experienced in traumatic brain injury.

Chapter 3

In Vivo Tool Designs

In this section the design of several in vivo tools are discussed. The in vivo large displacement dynamic indentation tool is the only tool that has undergone full development. The control architecture and tool validation are also presented. Existing in vivo tools are limited to capturing the material response at small and high strain rates, or large strains at quasistatic loading rates. The tools presented in this section are designed to address and fill the gap in the literature for in vivo measurement.

3.1 Literature review of in vivo measurement tools

A number of small, portable in vivo tools have been proposed in the literature [34][55][63][80]. Ottensmeyer designed the TeMPeST 1-D, a 12mm-diameter minimally invasive instrument to measure the compliance of solid organ tissues [63]. A 5mm-diameter circular punch is driven to vibrate by a voice coil motor to displacements of ±0.5mm while in contact with the tissue. The tool simultaneously records the applied load and relative displacement. When in contact with organ tissues, the open loop bandwidth is approximately 80Hz and forces up to 300mN can be exerted. The tool has been used in in vivo studies to measure the mechanical response of porcine liver and spleen. The TeMPeST 1-D captures the small strain, relatively high frequency response of the tested material. To determine the compliance of the material, a closed form solution for the indentation of a circular punch on a semi-infinite body is employed. Kalanovic *et al.* designed ROSA-2, an in vivo rotary shear device with a range of motion of ±15°, that travels up to a frequency of 20Hz [34]. The ROSA-2 device has a 6mm circular contact that rotates relative to a concentric ring fixed to the tissue with a pin array or tissue sealant. The torque on the tissue is exerted by a galvanometer. This device was validated on a gel simulant and preliminary results for soft tissues were presented. Valtorta and Mazza designed an in vivo torsional resonator device to perform dynamic shear testing [80]. By controlling the vibration aplitude, shear strains of less than 0.2% are induced in the tissue so that the material response is within the linear elastic regime. The complex shear modulus is characterized in the range of 1 to 10kHz. The material response due to motions induced by this tester are considered in the linear viscoelastic regime. Nava *et al.* designed an in vivo aspiration device in which a cannula with a 10mm diameter hole is placed in contact with the tissue and vacuum is applied. The internal pressure in the tube is maintained according to the desired pressure profile [55]. As a result, the tissue lifts into the tube and the corresponding displacement profile is captured by digital images taken from the side view. Using a linear viscoelastic model, the experiment is simulated and the material properties are obtained through solving the inverse problem (i.e., matching the simulation response to the experimental response by adjusting the material parameters of the simulation). While these tools offer capabilities in measuring the material response in the linear viscoelastic regime, they do not address the need to understand the large deformation, high strain rate material response of soft tissue in vivo.

3.2 Proposed designs

3.2.1 In vivo retractor tester

A key challenge in the surgical removal of brain tissue tumors is to ensure the removal of only tumor tissue, while keeping healthy tissue intact. To achieve this goal, improvements in the areas of surgical visualization and surgical navigation have been made within the past decade [33]. Additionally, the development of intraoperative magnetic resonance image-guided surgery has improved the procedure for tumor resections, but has at the same time highlighted the problem of brain shift (brain shape deformation) that occurs during surgery [54]. During neurosurgery, a brain retractor is often used to constrain certain areas of the brain (see Figure 3-1). The position and function of the retractor offers an opportunity for force/displacement

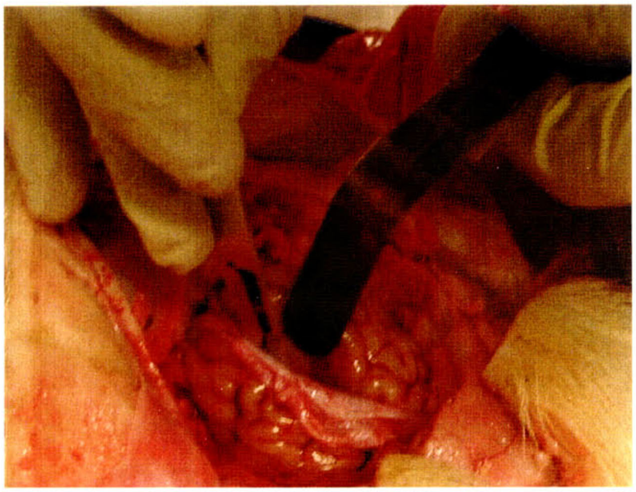

Figure 3-1: Image of normal use of a retractor on a porcine brain

measurements. Through these measurements, in vivo material properties can be inferred.

To test the forces applied to the brain by the retractor during neurosurgery, we equipped the brain retractor with a force sensing device, calibrated the device to measure the load at the end of the retractor and built the apparatus. The surgery will occur on a porcine brain, a well-accepted animal model to simulate human brain tissue [26][51]. To understand the location of the retractor relative to the other structures in the brain, we planned to use Magnetic Resonance Imaging (MRI). MRI of the brain will allow us to capture the entire volume of the brain as well as visualize the deformation of the volume due to the positional changes of the retractor. A resulting design specification was that all components of the device had to be MRI-compatible and could not contain ferrous materials. The retractor had to be kept as thin as possible, or at least as thin as existing retractors, and had to fit between the two hemispheres of the brain without damaging any surrounding tissue. This constraint was particularly challenging as most force sensors are attached at the point where the force that is to be measured, and traditional force sensors do not offer such thin profiles. To address these constraints, we designed a retractor tester that measures the force applied to the tissue at a location away from the contact point (see Figure 3-2). The retractor contacts the brain tissue with a cylindrical disk that sits at the end of a telescoping set of hollow copper tubes. This assembly was to be placed in between the left and right hemisphere of the brain. Once the placement (depth and lateral locations) of the

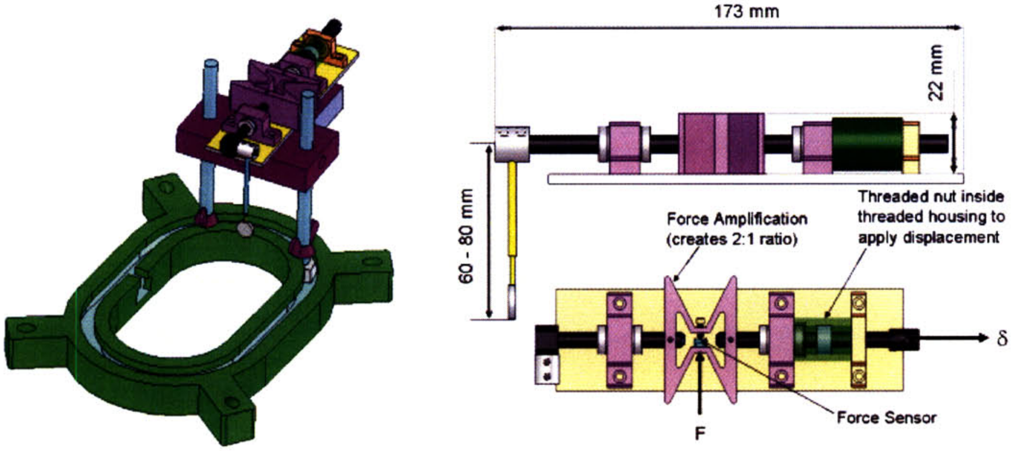

Figure 3-2: Retractor assembly designed to measure in vivo static forces applied to the brain during neurosurgery

retractor was determined, the end of the shaft would be attached to the remaining assembly. In order to orient the entire assembly to the skull of the pig, a delrin head coil (see Figure 3-2) was designed. This ring not only allowed for the entire assembly to move along the slotted profile, but may also be fitted to house a copper MRI head coil that focuses the MRI field around the brain of the pig. The four outriggers of the coil frame allowed for four brass skull pins to be inserted into the skull of the pig, and thereby fix the assembly relative to the skull.

The force measurement from the assembly comes from the flexure placed in between the two carbon fiber shafts. The distal end of the shaft (away from the retractor) is actuated by an externally threaded nut internal to an internally threaded collar. The two shafts are allowed to slide axially, but are held radially by two ceramic bearings that have very tight clearances. Adjoining the two shafts is a flexure containing a small force sensor (Allied Electronics, Tempe, AZ) preloaded by a thumb screw. After inserting the retractor into the brain, it is attached to the rest of the assembly and actuated axially using the threaded collar. The force sensor is initially preloaded by a screw and upon loading the brain, the flexure deforms and the force on the screw is relieved. The flexure is designed so that the measured force is amplified by a factor of 2. Although this design was built, the attachment mechanism between the retractor and the assembly must be redesigned before the system is fully functional.

Spring stiffness range	0.6 - 5.0N/mm
Moving mass	20.0g - 50.0g
Tip excursion range	0 - 9mm
Velocity	0.1 - 2.0m/s
Strain rate (tip dia = 12.5mm for 9mm of travel)	160s^{-1} - 320s^{-1}

Table 3.1: Specifications of in vivo spring-loaded tool

3.2.2 In vivo spring tester

Another in vivo tool, a spring-loaded indentation tester with an excursion range of 0 to 9mm, was designed and built. The actuation of the indenter tip occurs when energy stored in the compression of a spring is released and transmitted into kinetic energy; launching the indenter into the tissue. The pre-compression for the spring is adjusted by using a micrometer, and the total excursion of the tool can be varied by adjusting an internal stop. Both the depth of indentation (using internal stop adjustment) and the velocity of the indenter (using precompression of the spring) can be independently varied. The device acquires displacement and force data throughout its motion. The displacement is measured by a miniature Differential Variable Reluctance Transducer (DVRT) (MicroStrain, Willston, VT) with an unfiltered frequency response of 7kHz and a repeatability of $+4\mu$m. The force sensor (Honeywell, Columbus, OH) has a range of 0 - 5N and operates at an unfiltered frequency of 1kHz. Spring stiffnesses ranging from 0.6 - 5N/mm have been selected. The tip of the tool is interchangeable to any appropriate shape and size. By varying the spring stiffness, inertial mass, and displacement, the velocity of the tool can be prescribed. The spherical tip shown in Figure 3-3 has a diameter of 10mm, and footprint of the tool is 200mm x 75mm x 50mm. Table 3.1 outlines the design parameters of the tool, while Figures 3-3 and 3-4 show a schematic of the tool as well as the interface with the data acquisition system.

Although this tool may be mounted in multiple configurations (vertical or horizontal), it was designed to be vertically mounted as shown in Figure 3-4. The actuating spring is precompressed and held in the compressed position by a trigger-release mechanism. Upon activating this flexural release, motion of the indenter into the tissue is initiated. The motion comes to an abrupt stop when the stop on the shaft meets the adjustable endstop of the tool.

This tool was tested against foams and silicone gel simulants to demonstrate its capabilities.

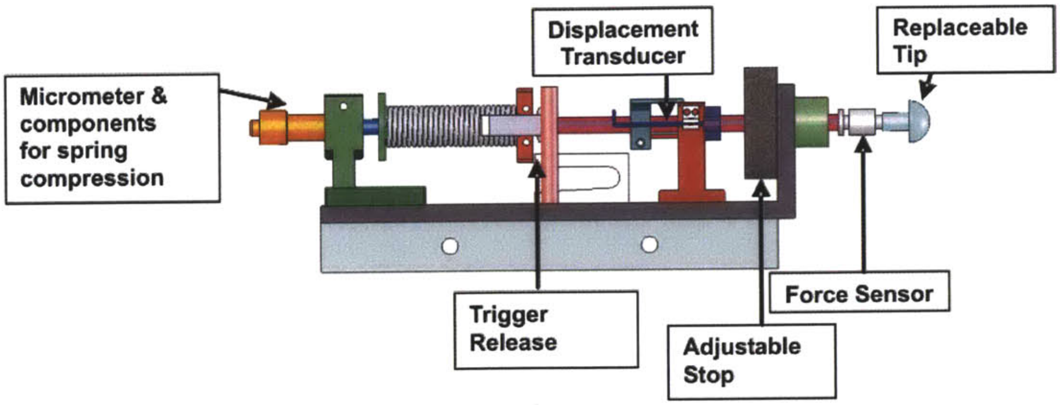

Figure 3-3: Design details of in vivo spring-loaded material testing device

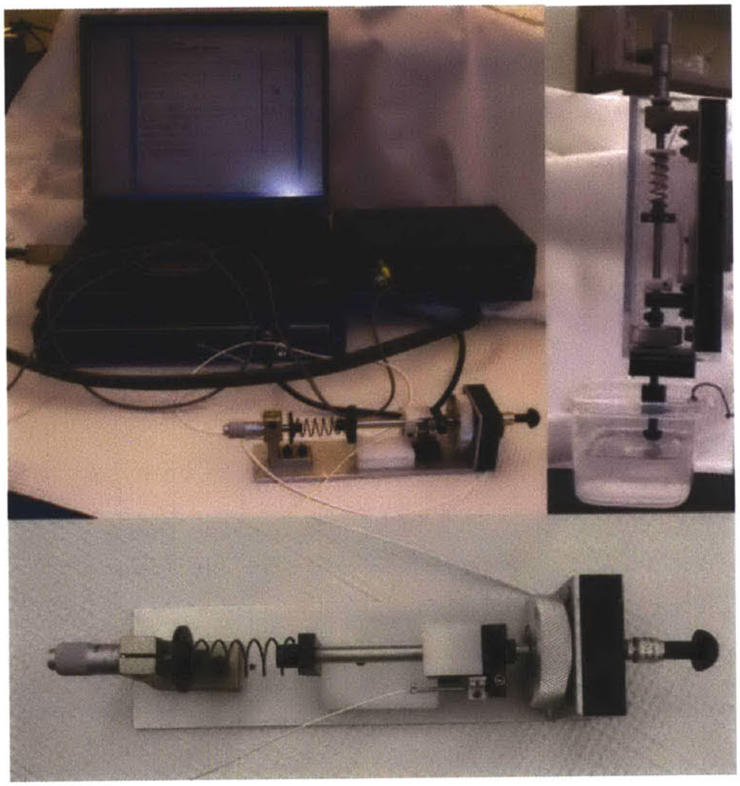

Figure 3-4: Portable spring-loaded mechanical tester shown with data acquisition system

The force data were collected through the entire range of motion. However, upon impact the force response spiked sharply; the force sensor was not designed to handle such impact forces. We incorporated an accelerometer to better understand the inertial loads, but unfortunately, the 50g accelerometer also saturated upon impact. This finding poses a significant design challenge. In order to implement this tool, sensors more tolerant to impact conditions must be incorporated.

3.2.3 In vivo dynamic indentation tool

For applications of interest to the current study, i.e. in-vivo testing of biological tissue, a compact, portable testing tool is necessary: the final tool design presented is a large excursion adaptation of an approach proposed by Ottensmeyer [62].

Components

In order to measure the behavior of the tissue under large strain and high strain rate conditions, we chose a voice coil motor (H2W Technologies, Valencia, CA) with an excursion of 12.5mm. The selected voice coil is a moving magnet actuator supplied with internal bearings and a moving shaft. The main advantage of the moving magnet actuator is that there are no moving leads, since the coil assembly is stationary. Voice coils operate on the principle of the Lorentz Force Equation (see Equation 3.1), where B is the flux density (Tesla) and I is the current (amps) running through the coil.

$$F = B \times I \tag{3.1}$$

Simply stated, a current-carrying conductor placed in a magnetic field will have a force exerted upon it. This force is proportional to the direction and magnitude of the current and the flux density field. Since the permanent magnet flux density field is fixed, the direction of the linear displacement depends on the polarity of input current. The amount of force produced is directly proportional to the magnitude of the input current. The chosen voice coil motor (NCM-05-08-0052JBT) can provide a maximum continuous force of 2.25N and a transient peak force of 6.75N. The motion of the motor is driven through a linear power amplifier (Quanser, Ontario, Canada). The amplifier is designed to drive inductive loads such as DC-motors and voice coil

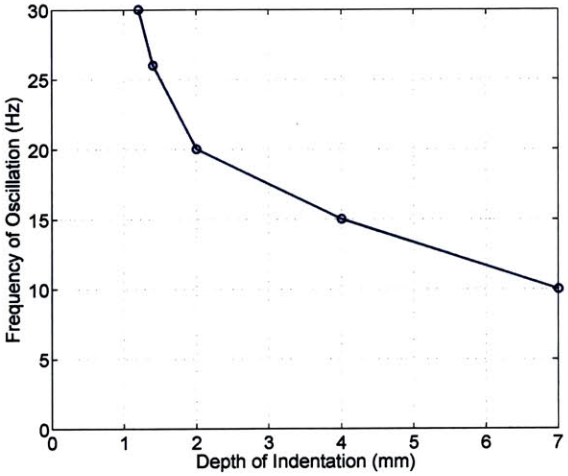

Figure 3-5: Tool capabilities given by the frequency of oscillation versus the depth of indentation travelling in air

actuators. The unit operates from a 30V power supply and provides a maximum continuous current of 7A. Springs (k=350N/m) were installed on the proximal and distal ends of the shaft between the motor end stops and the motor housing. The springs transform the system from a nearly pure inertial system to a spring-mass system that has a natural equilibrium point and can be controlled more easily. The force output (current capacity) limits the operational frequency of the system for sinusoidal oscillations: with the current moving mass of 40.0g, the tool can operate at a maximum frequency of 30Hz for 1mm displacement amplitude. For larger displacement amplitudes, the maximum frequency decreases (e.g. at a 7mm amplitude the frequency is limited to ~10Hz). Figure 3-5 describes the tool's capabilities when operating in air.

An excursion of 7mm at 10Hz roughly corresponds to a maximum velocity of 70mm/s and incorporating a 12.5mm diameter spherical indenter corresponds to a strain rate of approximately $\dot{\varepsilon}_{tool} = 11.2\text{s}^{-1}$ where strain is defined as the ratio between the excursion and the radius of the indenter. To measure the shaft displacements, a sensor known as a linear variable differential transducer (LVDT) (TransTek, Ellington, CT) is placed at the proximal end of the tool, and shares a shaft with the voice coil motor. The LVDT consists of a primary coil and two

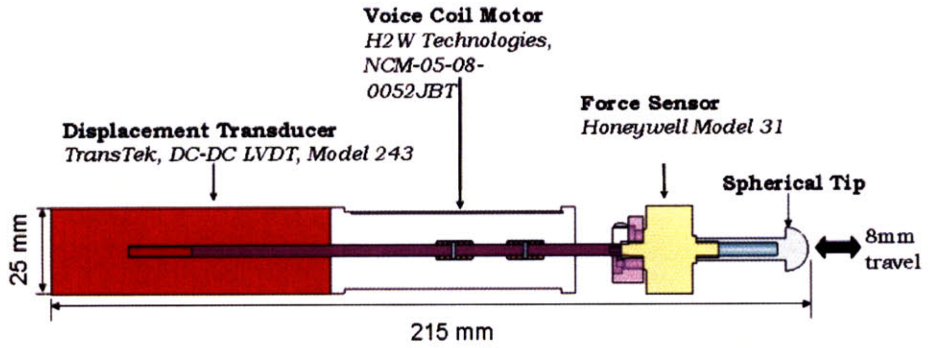

Figure 3-6: A cross-sectional view of the in vivo dynamic indentation tool

Inertial mass	40.0 g
Voice coil motor	
Continuous output force	2.25N
Maximum peak force	6.75N
Force sensor max load	10.0N
Displacement sensor	
Full range	12.5mm
Working range	8.0mm

Table 3.2: Specifications of dynamic indentation surface tracking (DIST) tool design

secondary coils wound on an armature. The primary coil is excited and induces a voltage in the secondary coils. The difference between the voltage of these output coils results in motion of the core (armature) with respect to the coils. A 1000g subminiature compression/tension load cell (Honeywell, Columbus, OH) is attached at the distal end of the tool. The force sensor is mounted as closely as possible to the indenter tip to minimize measuring the inertial loading of components beyond the tip itself. This bonded foil strain gage sensor is excited using a 12V DC power supply. The force sensor differential output signal passes through a universal in-line amplifier (Honeywell, Columbus, OH), which amplifies ±15mV output signal to ±10V. The indenter tip is interchangeable; in the current design, a 12.5mm diameter hemispherical indenter tip has been selected. The total moving mass of 40.0g consists of the motor/LVDT shaft, the force sensor, the tip and the attachment components. Figure 3-6 illustrates the tool, while Table 3.2 describes the operating characteristics. For an imposed indenter displacement history the force sensor measures the corresponding reaction force exerted by the material on the indenter tip.

Control and data acquisition system

The original tool design proposed to run the displacement of the device open loop and output the resulting force exerted on the tissue. Although this approach is reasonable, we felt that by building a closed-loop system, the motion could be controlled much more effectively and the motion frequency could be driven to higher regimes than if operated in open loop mode. To achieve closed-loop control, a motion control board (Galil, Rocklin, CA) was selected. This motion controller can operate 2 axes simultaneously and can capture up to 40 digital and 8 analog inputs. It contains a 32-bit microprocessor that runs independently of the laptop thereby not interfering with or causing clock speed delays. The motion control communication with the laptop occurs via an RS232 port. The force sensor output and displacement of LVDT shaft are recorded using the analog input channels of the data acquisition system. Data may be acquired at a maximum of 250 samples/s for up to 8000 available array elements. This closed-loop control system operates in displacement-control mode for arbitrary loading histories (stress relaxation, constant strain rate load/unload ramps, sinusoidal oscillation, etc) within a range of frequencies. The tool capabilities are described in Figure 3-5. Figure 3-7 describes the architecture and wiring for the motor, linear amplifier, controller, and sensors. The ground loop is reinforced by ensuring that the power supplies and amplifier are connected to the same ground lug. This is a particularly important feature to reduce noise in the system.

3.3 Mounting configurations

3.3.1 MRI frame configuration

Both the spring tool and the dynamic indentation tool may be mounted to a testing frame constructed of 6061-T6 aluminum profiles (MiniTec Framing Systems, LLC Victor,NY). The system design was motivated by the in vivo study that will be performed; this entailed providing a range of motion for the tool that allows for adjustments to accomodate a 50kg porcine animal. The study was also designed so that brain MRI images of the porcine animal model may be acquired between each testing sequence. For this reason, the frame accommodates the MRI table from the General Electric 3.0T MRI system (GE Healthcare, Chalfont St. Giles, UK).

Details of the system footprint and ranges of motion may be found in Figure 3-8. The first axis of motion is provided in the y-direction using two linear rails. The x-axis is mounted to the y-axis and contains one linear rail. These two axes (x- and y-) are free floating and do not have encoders, motors or ballscrews to dial-in the precise location. The intent was to grossly locate the x- and y- axes and use locks on each rail to fix the position at the desired location. The vertical z-axis motion is actuated using a manual BiSlide with counter (Velmex, Bloomfield, NY). This positioner was selected to provide 250mm of manually adjusted linear motion. Because of the delicate nature of the in vivo porcine brain tissue, we chose to manually actuate the z-axis such that the initial position of the indenter relative to the brain tissue could be precisely adjusted (screw pitch=1turn/cm). Attached to the z-axis is a 3-axis rotary positioner (Newport Corp, Irvine, CA) that provides 360° rotation along its axes and ±25° of rotational adjustment in the other two axes. This additional feature allows the instrument to be aligned orthogonal to the measurement surface. Designing the frame to be fully adjustable in six axes (3-linear, 3-rotational) enables the user to accurately position the tool to the desired testing location.

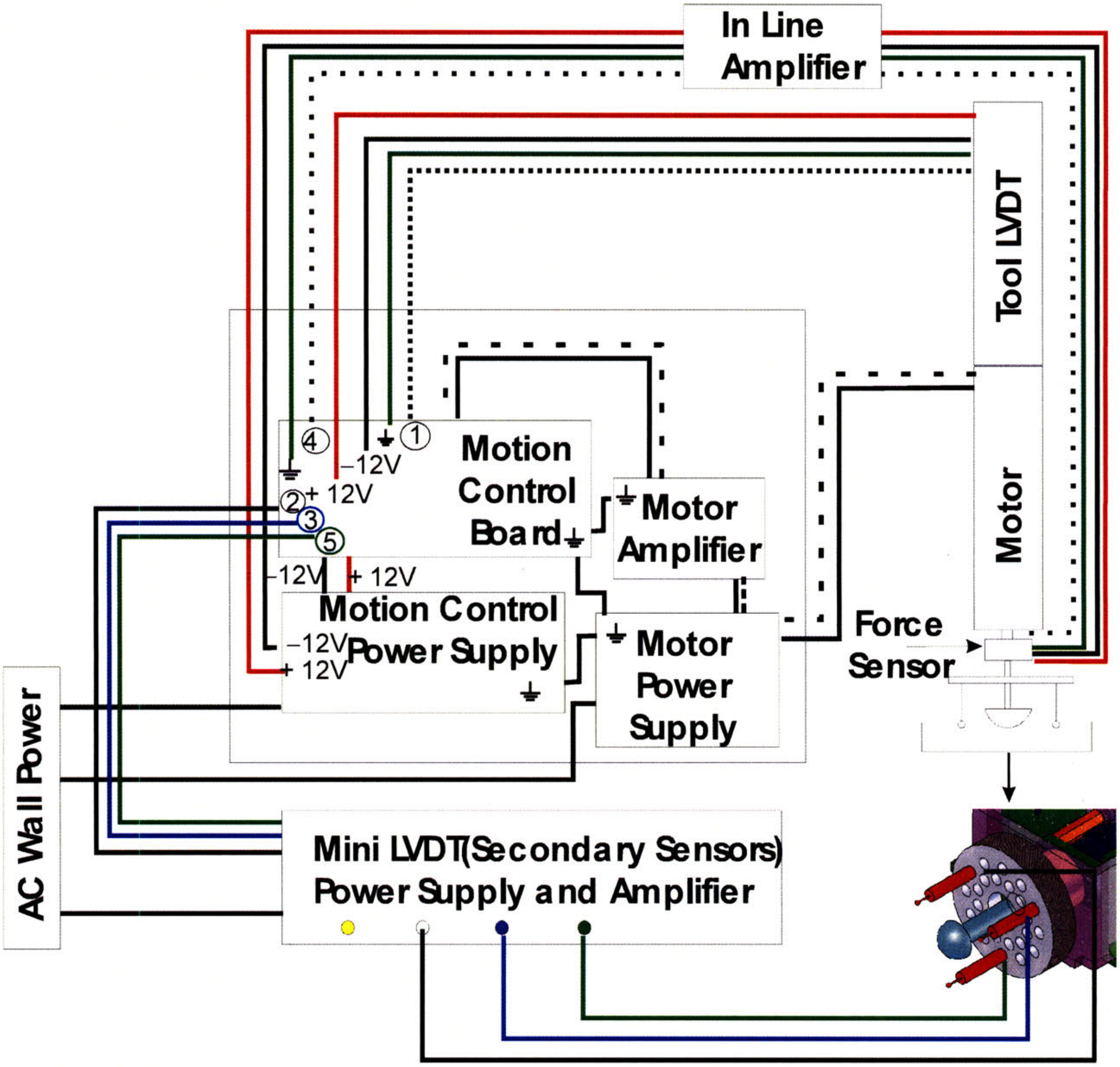

Figure 3-7: Schematic of data acquisition and motion control architecture for indentation device

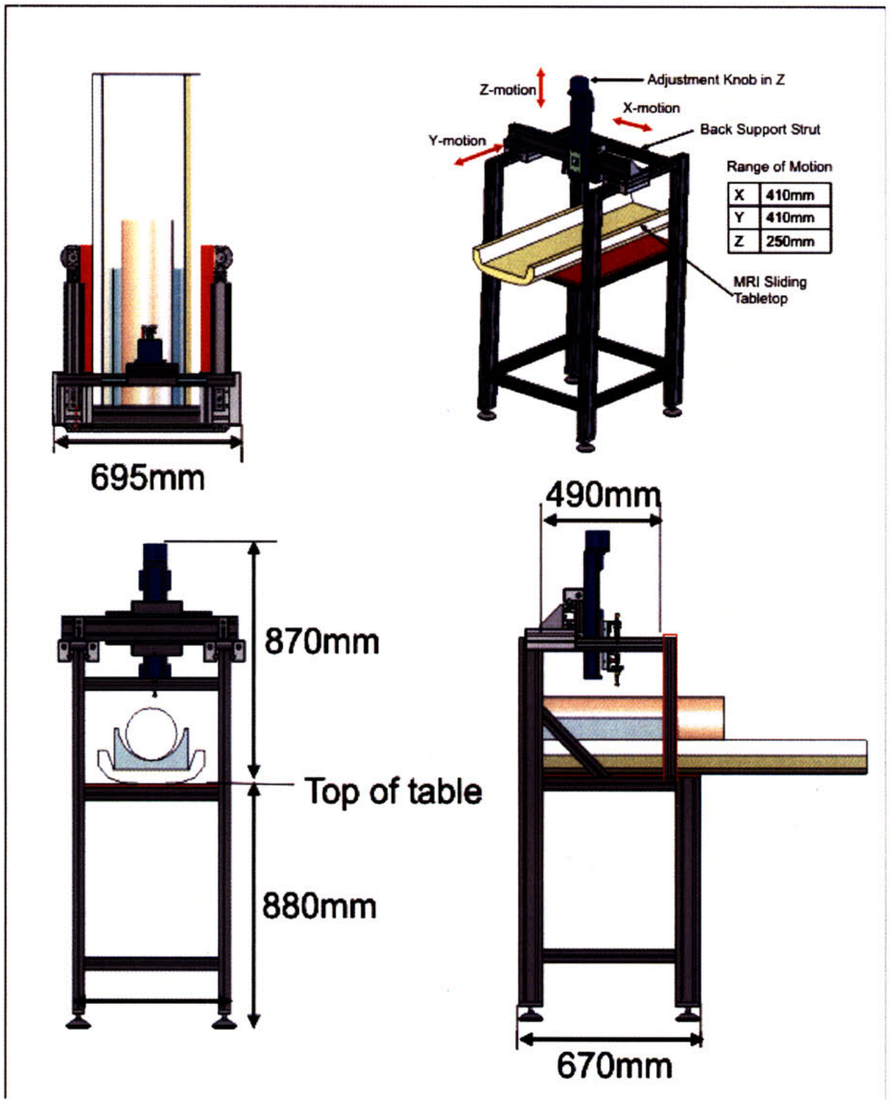

Figure 3-8: Detailed drawings of frame footprint and the ranges of motion in the linear axes

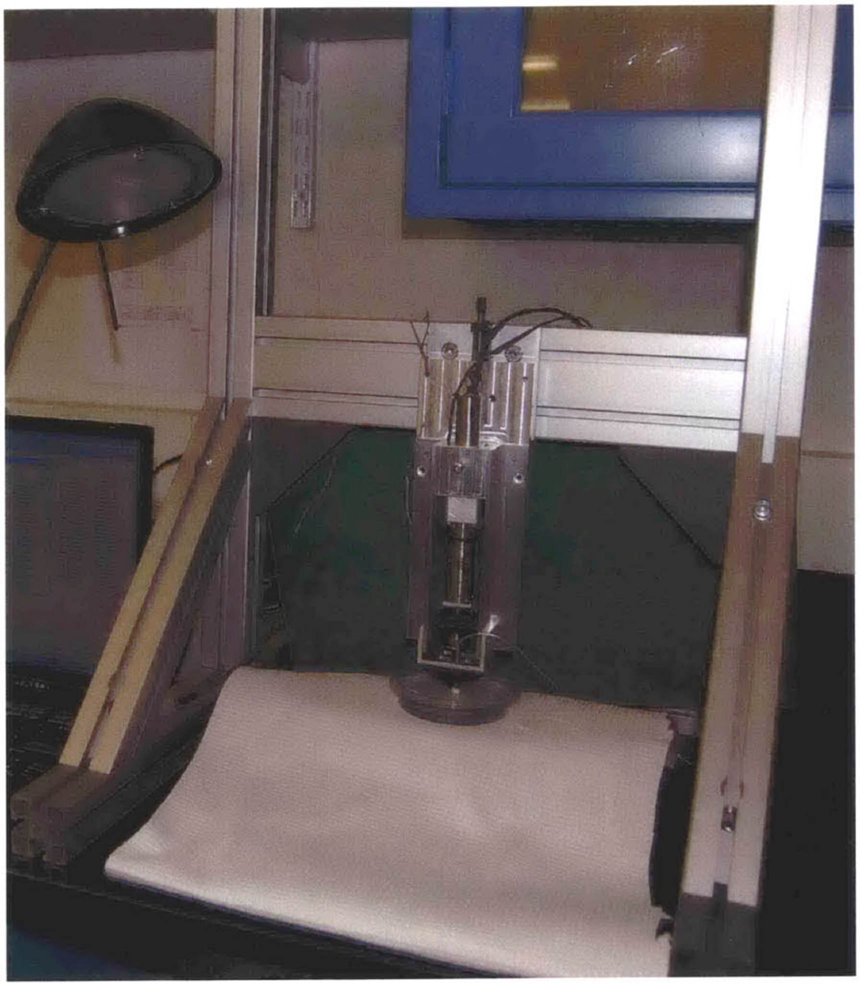

Figure 3-9: Frame for mounting tool in the laboratory

3.3.2 Benchtop frame configuration

To perform calibration and validation on the tool, a smaller frame constructed from 6061-T6 aluminum profiles (MiniTec Framing System, LLC Victor, NY) was built. The configuration of this frame is shown in Figure 3-9. The gross motion of the center beam, to which the tool is attached, can be manually adjusted in the vertical direction by loosening the fastening bolts. The fine motion is achieved using a 1in travel manual linear slide (Newport Corp, Irvine, CA) with an adjustable leadscrew (pitch=3.2 turns/mm). This frame is rigidly mounted to the lab bench using C-clamps.

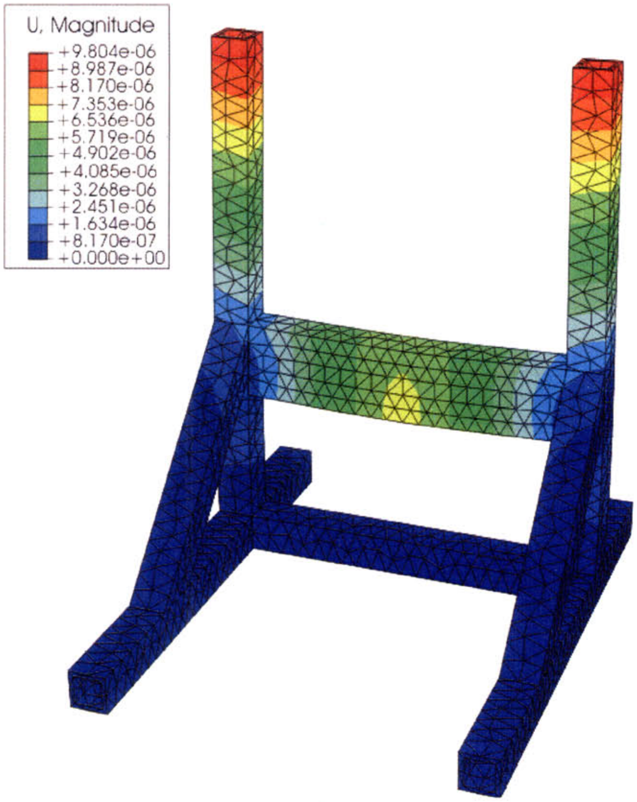

Figure 3-10: Contour plot of the frame deflection under static loading

To assess the stiffness of the frame, a finite element analysis (FE) of the frame was performed. Each aluminum profile was assumed to be rigidly attached to one another, and a force of 6.25N (maximum peak force output of the motor) was used to determine the maximum deflection of the frame at the tool mounting location. The maximum deflection of the frame was found to be 6.5μm (see contour plot in Figure 3-10). The deflection is taken to be 13μm to account for the stiffness of the bolted joints in the model (the FE model was built on the assumption that the profiles are rigidly attached to one another) [71].

Based on the specified load and the computed displacement, the stiffness of the machine was found to be four orders of magnitude stiffer than the tool itself. The total stiffness of the tool was found by combining the stiffness of the shaft (axial stiffness), the stiffness of the load cell, the stiffness of the tip, and the stiffness of the springs installed within the tool in parallel. This value was primarily governed by the stiffness of the installed springs (k_{total}=700N/m). Taking the

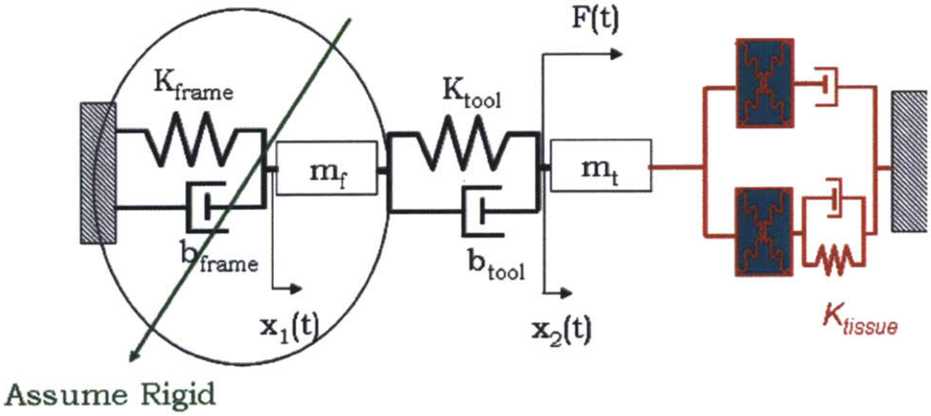

Figure 3-11: Model used to assess the stiffness of the mechanical system

K_{tool}	700N/m
m_{tool}	40.0 g
b_{tool}	1N-s/m
ω_n	$\sim$ 20 Hz

Table 3.3: Dynamics of tool

moving mass to be 50g, the resonant frequency of the system is found to be approximately 21 Hz, assuming open-loop control. The system model is shown in Figure 3-11 and the specifications are given in Table 3.3. Upon driving the motion of the indenter to this frequency, we observed the resonant frequency to occur around 22Hz. Because the operating frequency is beyond 20Hz, closing the loop with position control helps to ensure stability of the system.

3.4 Tool validation and calibration

The dynamic indentation testing tool was validated by applying a sinusoidal displacement input (amplitude=6.5mm, frequency=1Hz) to a stable, tissue-like simulant called RTV 6166 (GE Silicones, Wilton, CT). RTV is a two-part silicone gel that, when mixed in a 1:1 ratio produces a soft elastic material, exhibits behaviors similar to the material response of brain tissue reported in the literature.

The experiment was performed using the ElectroForce (ELF) Machine (Bose, Natick, MA),

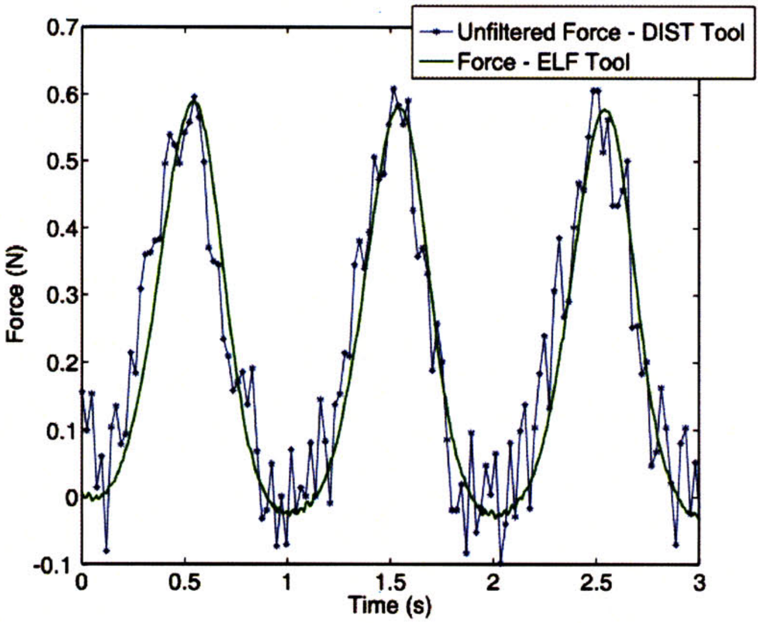

Figure 3-12: Results of a validation study comparing the force output on the ElectroForce machine and the dynamic indentation tool

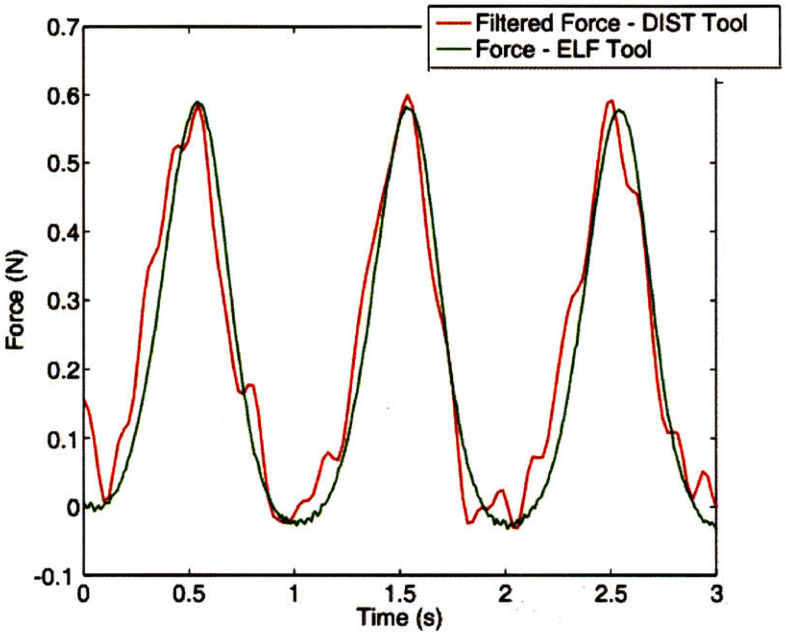

Figure 3-13: Filtered force signal from the in vivo tool compared with the force signal from the ElectroForce Machine

a dynamic mechanical analyzing machine with a range of motion of ±6mm and a closed loop bandwidth of 0 to 60Hz. A 12.5mm diameter spherical tip was placed on the shaft of the ELF Machine and the aforementioned protocol was initiated. The same procedure was performed using the dynamic indentation testing tool. The force output of the two machines were compared; results are shown in Figure 3-12. The higher frequency noise in the in vivo tool's force signal may be reduced using a 4th-order Butterworth low-pass filter with a cutoff frequency of 10Hz. When the filtered force from the in vivo tool is compared to the output force of the ELF machine, the results correspond well as shown in Figure 3-13. This validation process demonstrates the capabilities and efficacy of the in vivo tool; however, efforts to identify the source of noise in the tool are ongoing.

3.5 Tool design conclusions

The description and details of three different tool designs were presented in this chapter. All three tools were built, however given certain design challenges associated with the retractor tester and the spring-loaded tool, we focused efforts on the dynamic indentation tool. Some design revisions are necessary to go forward with the two other tools, and we are hopeful that work with the retractor instrument and spring-loaded instrument may be continued in the future.

Chapter 4

Secondary Sensor Design

The mechanical response of soft tissue can be significantly different in its in vivo and in vitro states [6][20][24][26][45][49][51][61][64][70]. The importance of collecting material responses in vivo is becoming increasingly recognized in the realm of soft tissue mechanics. Current in vivo and in situ testing procedures are dominated by indentation techniques due to the simplicity of the tool configuration, the limited access requirements, and the small risk of injury associated with the testing. This technique is derived from traditional hardness tests, often performed on metals, rubbers, and thin films when the materials cannot be removed from their original environment. The indentation force-displacement history is a single integrated output governed by the material response over the whole domain of deformation, combining large-strain effects (in the near-field) and small-strain response (in the far-field). The major challenge for this testing technique is in finding a unique solution to the "inverse problem" i.e.; obtaining material properties consistent with the indentation force-displacement data. Much of the information related to the interplay between shear and bulk compliance in the complex deformation field beneath the indenter is lost when capturing this single output. In most conventional applications, bulk/shear relationships are simply inferred based on typical mechanisms of deformation for a given material class; i.e., incompressibility for plastic deformation in metals [79], typical values for Poisson's ratio in the linear elastic regime for oxides/ceramics [4], or incompressibility of hyperelastic deformation in rubbers [82]. Researchers have been attempting to address this innate limitation and distinguish volumetric and isochoric (shear) compliances by comparing results for indenters with different shapes [31], or measuring both normal and tangential contact moduli [41] and measuring the geometrical feature of the residual indenter imprint [9].

The mechanical behavior of biological tissue is complex, with nonlinear, time-dependent features, and marked differences between shear and bulk responses. When applying indentation testing approaches to hydrated soft biological materials, where the bulk response is controlled by entirely different physics (i.e., the diffusion of hydrating fluids), the value of a single load-displacement response diminishes. Approaches proposed for conventional applications [31] [41] to distinguish between the material volumetric and isochoric responses suffer from the noise inherent in comparing results of sequential tests. In particular, for biological materials, there is an intrinsic lack of repeatability due to variations in the material response if tests are performed on different sites, and to conditioning effects if tests are performed on the same site at successive times. Any technique based on analyzing slight differences between the results of two tests (i.e., tests conducted with indenters of different shape) will be impaired by the noise in the data.

We propose a material testing technique that follows the well-proven path of conventional indentation methods, but enriches the signal by acquiring displacement data not only for the actuated indenter, but also for a set of offset, passive secondary sensors. These devices are brought in contact with the material and used to record the history of surface displacement in the region immediately surrounding the (actuated) indenter. The advantage of this technique is that, by combining the indenter force response with the displacement responses of the passive secondary sensors, a signal that directly captures the deformation of the material in the near field is obtained. This is particularly relevant when testing materials in their large-strain nonlinear regime. A primary advantage of this approach is that it can provide additional information to deconvolute the shear and bulk contributions to the indenter force-displacement response from a single test, without adding substantial complexity to the tool.

The objective of this chapter is to provide a proof-of-concept for the aforementioned technique. We consider a fully synthetic testing scenario in a finite element framework. We simulate indentation tests performed on three classes of materials: linear elastic, nonlinear hyperelastic, and time-dependent. We demonstrate how the single indenter load-displacement response is not sufficient to differentiate, within the same class, between materials with very different balances between their shear and bulk compliance. In contrast, we show that the secondary signal from the passive sensors reflects these differences, and can therefore be used to better characterize the material response.

4.1 Literature review of indentation

A comprehensive review of the development of testing techniques using indentation is provided by Gouldstone et.al [27]. While earlier applications were mainly directed to characterize the response (hardness) of metallic alloys [74] and elastomeric materials [23], indentation techniques have experienced a resurgence due to their convenience in testing materials at small length-scales and their ability to provide in-situ properties through a minimally invasive approach. Indentation techniques are widely used to measure the behavior of materials such as thin films, coating for MEMS applications, and biological tissues. Oliver and Pharr [59] pioneered the field of nanoindentation by establishing a systematic method to determine the stiffness of linear elastic materials. In the following years, the method underwent several refinements and its applicability was extended to elastic-plastic materials (see an extensive review as provided in [60]). Indentation methods were also applied to obtain linear viscoelastic properties of polymeric materials [12][32][40][58]. The aforementioned studies mostly relied on (approximate) analytical treatments of the boundary value problems to solve the corresponding inverse problems and determine the best fit to material parameters. When the material behavior demands the use of more complex constitutive models, numerical techniques such as finite element simulations are required to obtain the force-depth response to indentation, as in the study performed by Qi et al [67] to determine a relation between hardness values and nonlinear hyperelastic material properties. A computational approach is also required when considering materials for which the resistance to deformation is controlled by mechanisms with length-scale dependence. A recent example of this approach is given by the study in [28], where a linear biphasic poroviscoelastic (BPVE) constitutive model was used to characterize the response of an agarose gel.

Biological materials such as brain [26][49][47][48], liver [36], and cartilage [39][81] have been tested using indentation methods. The conditions of the tissue greatly affect its response, as demonstrated by a number of studies comparing in vivo and in vitro measurements [26][51][25]. Depending on the objectives of the specific application, models used to represent biological tissue response range from isotropic linear elastic, to anisotropic nonlinear poroviscoelastic; the determination of the corresponding material properties becomes very challenging for the more complex models [47][72][84]. A number of indentation tools have been proposed in the literature [26][47][62] for in vivo applications. Typically, the motion of the main indenter is driven by an actuator, and the in-line force and displacement responses are measured accordingly. To characterize the time-dependent large-strain response of soft tissues the following loading histories are commonly used: creep response to a step load e.g. [36], stress relaxation under a step displacement e.g. [26], and constant strain rate ramp loading and unloading e.g. [47]. Though not applicable to investigate large-deformation behavior, the dynamic response to sinusoidally oscillating small displacements is also commonly measured to provide insight into the balance between energy storage and dissipation mechanisms [62]. Each of these tests captures different aspects of the behavior of the material at different time scales and often more than one test is necessary for complete characterization of the time-dependent indentation response.

It is always challenging to reconstruct the 3D constitutive response of a material based solely on 1D force-displacement data. Typically this problem is solved by postulating relationships between the bulk and shear material response. In the case of linear elasticity, material behavior is characterized by two independent material properties such as the Young's modulus and Poisson's ratio, or the shear and bulk moduli. For homogeneous, simple modes of deformation, such as uniaxial tension and compression, the 1D force-displacement data can be readily complemented by lateral stretch measurements, thus providing sufficient information to realize the 3D formulation. For indentation tests, the material displacement field is complex and inhomogeneous. Most of the large-strain deformation is confined to a small region around the indenter. Interpretation of the corresponding force-displacement response in terms of bulk and shear contributions is not easily attained. To address this challenge, Lucas *et al.* [41] developed a bench-top multi-dimensional contact mechanics system to measure normal and tangential elastic contact moduli. To measure both normal stiffness and tangential stiffnesses along two orthogonal directions, three sequential tests were needed for each material considered in the study. This technique was used to test relatively stiff materials such as silica, aluminum and copper, and provided good measurement for Poisson's ratios. Huang *et al.* [31] used both a Berkovich and a spherical nanoindenter to perform experiments on polymeric materials. Differences between the responses in sequential tests performed with the two indenters allowed them to obtain two independent viscoelastic functions (bulk and shear relaxation). For the special case of linear elasto-plasticity (and constant elastic Poisson's ratio), Huber *et al.* [52][53] describes a theoretical model using neural networks to derive Poisson's ratio by comparing sequential loading-unloading indentation responses. A fundamental limitation for the aforementioned approaches is that they rely on separate tests to reconstruct the 3D nature of the material response. For biological tissue, the material response to a fixed configuration/history of deformation can vary substantially between sites and, for the same site, at successive times (due to conditioning effects, changes in hydration, etc). Any approach that relies on differences between the results of two (different) tests can be rendered ineffective by this intrinsic variability. Bolzon *et al.* proposed to measure geometrical features of the residual indenter imprint by an optical or scanning probe device (such as an AFM) [9]. This approach appears promising in bench-top measurements for elastic-plastic materials but it is not suitable for biological tissue applications. In the following section we propose an approach where both the primary time-force-displacement measurement and complementary data to characterize the 3D material response are obtained in the course of a single test.

4.2 Novel design addition

We believe there is opportunity to gain additional data by measuring the response of the material both at the indentation site and in the near field. The novel design addition to the tool is the incorporation of passive displacement sensors, placed at a set radial distance from the main indenter. By placing captive spring-guided linear variable differential transducers (LVDTs) at an optimal offset from the main indenter, the near field surface displacement of the tissue can be measured. The secondary LVDT sensors are not actuated by the motion of the main indenter, thereby not adding inertial mass to the actuated system. Figure 4-1 illustrates the current embodiment of this design addition, which relies on three secondary LVDTs. These secondary sensors are threaded into a moving collar and placed at a radial distance of approximately 11mm from the main indenter. The collar is threaded onto the frame of the machine and, immediately prior to testing, the LVDT free tips are brought in contact with the test material by advancing the collar. The collar is further advanced by approximately half of the excursion range of the

LVDT springs (preloading) and held at this fixed position while the main indenter is actuated and displaces into the tissue. As the tissue is displaced by the main indenter, the secondary sensor tips, located in the "near region", record the history of normal surface displacement (Secondary Output).

Three sensors allow the determination of a surface "tangent" plane at the indentation site with a good degree of confidence and can be used to orient the axis of the main indenter orthogonal to the tissue surface. For this design, the LVDTs are spring-loaded to allow the tips of the secondary sensors to remain in contact with the material surface throughout the indentation history. Depending on the class of materials being tested (elastomers, metals, and tissues) the tip geometry and the stiffness of the LVDT springs can be optimized to best capture the near field surface displacement. The LVDT stiffness must be sufficient to overcome any frictional effects that might prevent the tips from maintaining contact with the material surface. On the other hand, disproportionate stiffness can lead to excessive preloading/displacement of the material at the secondary locations, and reduce the range of tip excursion during testing. The location of the secondary sensors with respect to the main indenter is also an important design parameter in optimizing the quality of the near field signal. In the current design, the moving collar that houses the secondary sensors has several discrete positions where the sensors can be threaded, with distances from the indenter axis ranging between 10mm and 16mm. The collar is interchangeable and offset distances can be optimized to best suit specific applications. For complex material behaviors, finite element (FE) simulations are most effective to determine optimal design parameters. As the details of the material response are not known a-priori, an iterative approach may be needed. The current configuration of this integrated Dynamic Indentation Surface Tracking (DIST) tool is illustrated in Figure 4-1.

We argue that, by matching both primary and secondary experimental measurements to the corresponding predictions of a numerical (FE) model of the test, a more accurate and reliable characterization of the 3D response of the material can be attained. To illustrate the advantages and effectiveness of the proposed approach, we constructed a synthetic testing scenario. We considered different classes of materials, performed FE simulations of indentation tests, and generated "experimental data" for primary and secondary outputs. In the following sections we demonstrate that the single traditional primary output from the indenter is not

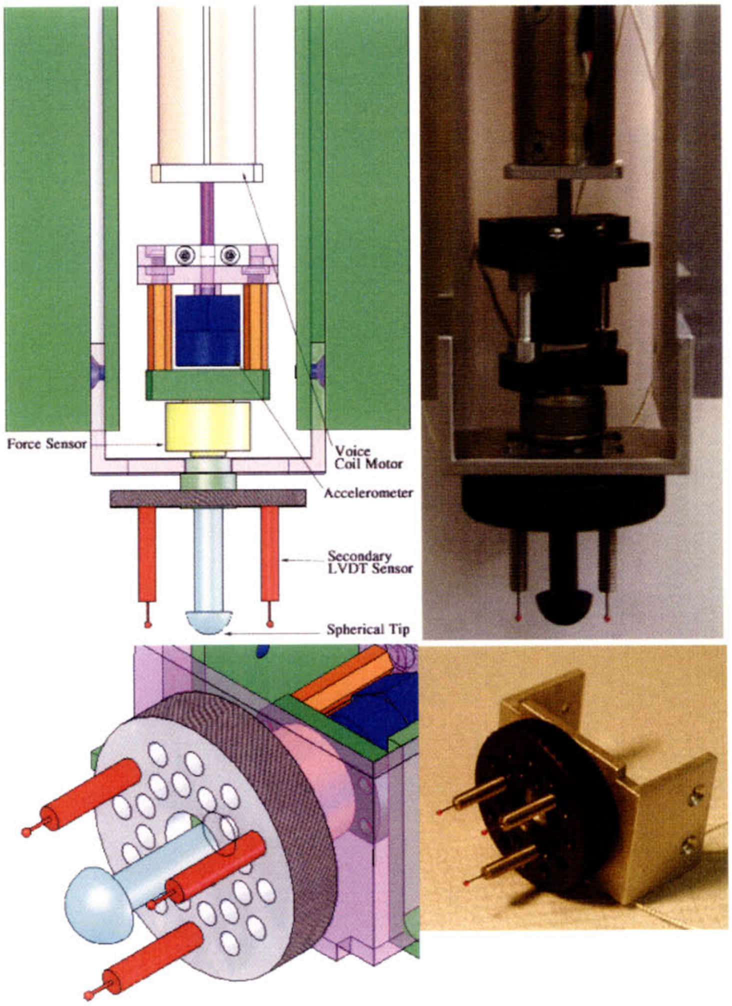

Figure 4-1: Dynamic indentation surface tracking (DIST) tool configuration

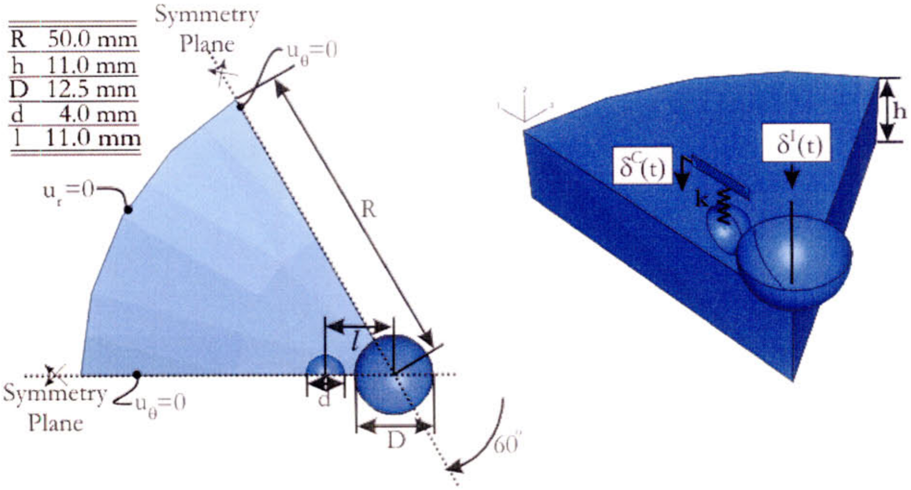

Figure 4-2: Three-dimensional finite element model

able to differentiate between the responses of materials with different constitutive responses. These differences can be captured by considering the additional data provided by the secondary sensors.

4.3 Methods

Finite element analyses were performed to investigate the effectiveness of combining secondary sensors with traditional indentation tests. A commercial finite element program (ABAQUS/Standard [29]) was chosen to perform the simulations. The extensive ABAQUS built-in material library allowed us to simulate material responses for constitutive frameworks relevant for soft tissue applications, ranging from nonlinear hyperelasticity, to viscoelasticity and poroelasticity.

For the current configuration of the tool, with three secondary LVDTs, symmetry arguments can be invoked to reduce the numerical model to one sixth of the actual geometry (Figure 4-2). Values for the geometrical parameters for this 3D model, given in Figure 4-2, were chosen to represent typical ranges for whole organ indentation testing.

The tissue lies on a flat rigid substrate. Radial displacement at the outer diameter of the tissue is constrained. The indenter tip and the secondary LVDT tips are spherical, and

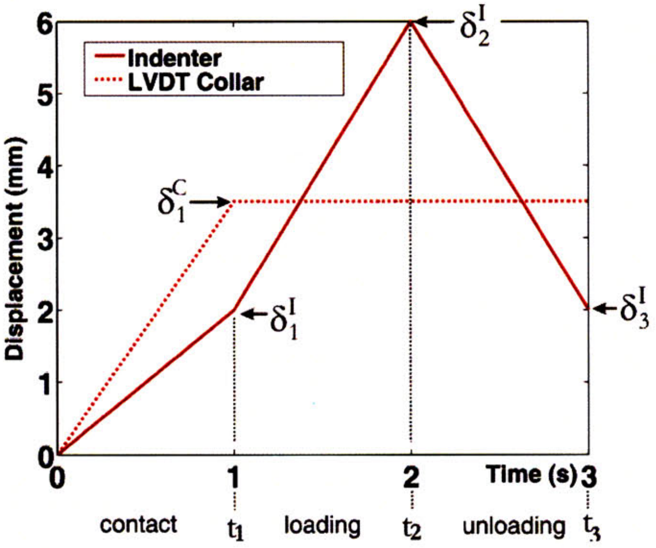

Figure 4-3: Imposed displacement history for indenter and for secondary sensor

modeled as analytical rigid surfaces. Contact between the tool and the tissue surface is modeled as frictionless, with an exponential normal compliance. The tissue FE mesh consists of 2092 linear, hexahedral elements (C3D8). The LVDT spring is modeled by a single truss element (T3D2) so that the spring stiffness is defined by the area and length of the truss, and by a linear elastic modulus. For all simulations we selected values for these parameters to provide an LVDT stiffness k_{LVDT}=3.5N/m.

For all simulations, the loading history was defined as shown in Figure 4-3. In the initial configuration (t=t0=0), the indenter and LVDT contact surfaces are located 2mm above the tissue surface.

Over the time interval between t0 and t1=1s (contact step), the indenter is brought in contact with the tissue (δ_1^I=δ^I(t1)=2mm); the collar is advanced by 2mm plus a 1.5mm offset (collar interference) to a distance δ_1^C=δ^C(t1)=2mm, so that the secondary tip is pushed against the tissue by the compressed LVDT spring. The secondary tip indents the tissue to an initial depth δ_1^T, and the LVDT spring shortens by δ_1^S= 1.5mm-δ_1^T. The relative magnitudes of δ_1^S and δ_1^T depend on the stiffness ratio between the tissue and the LVDT spring. The collar position is held constant for the remainder of the loading history (δ^C(t)=δ_1^C=3.5mm for t>t_1). Over the

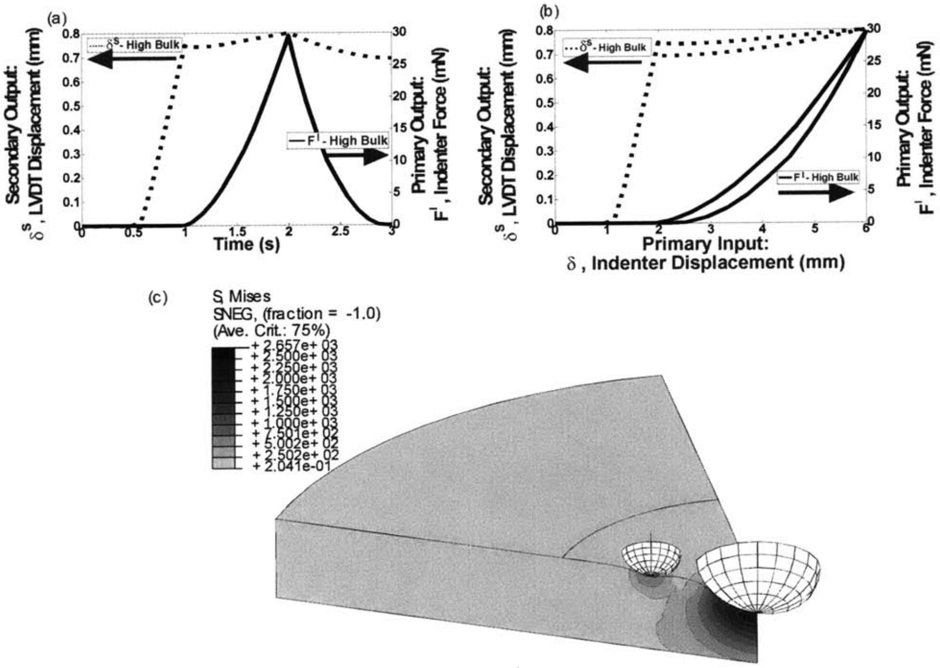

Figure 4-4: Typical simulation output based on input conditions

time interval between t_1=1s and t_2 =2s (loading step), the main indenter is displaced into the tissue at a constant displacement rate to a maximum indentation depth of 4mm corresponding to a total displacement $\delta_2^I=\delta^I(t_2)$=6mm. The indenter is then retracted over the time interval between t_2=2s and t_3=3s (unloading step) to a position $\delta_3^I=\delta^I(t_3)$=6mm, corresponding to the initial tissue surface position.

Given the imposed indenter displacement history, a conventional indentation tool will only measure the corresponding history of indenter force. The DIST tool complements the force history on the indenter with the displacement history of the secondary sensors. Therefore, for each indentation simulation, we generate an "experimental output" comprising a Primary output (Indenter force history) and a Secondary output (LVDT displacement history). For illustration purposes, in Figure 4-4, we show a typical "synthetic experiment" output. Figure 4-4(a) shows the force history on the indenter, $F^I(t)$, and the displacement history measured by the LVDT sensor, $\delta^S(t)$, for a simulation where the tissue was modeled as a viscoelastic material (E=2500Pa and ν=0.4, with a time-dependant Prony series where G1=0.4 and τ_1=0.5). The LVDT displacement output, $\delta^S(t)$, measures the magnitude of the net tip displacement with respect to the collar i.e., the decrease in length of the LVDT spring. The LVDT tip comes in contact with the tissue during the contact step. At time t1, the main indenter is just at the surface of the tissue, with zero force, the LVDT tip is pushed into the tissue, and the LVDT spring is compressed by δ^S. As the indenter is displaced into the tissue and retracted, between t1 and t3, the near-field tissue deformation changes the force balance at the LVDT tip, so that the tip position adjusts, and the LVDT output measures the history of net tip displacement $\delta^S(t)$. Figure 4-4(b) shows the same response plotted against the primary input, i.e., the main indenter displacement. For a viscoelastic material, hysteresis effects are visible both in the indenter load-displacement curve, as well as in the LVDT displacement curve. Figure 4-4(c) illustrates the configuration of the FE model at the end of the loading step, with a contour plot of the Mises stress levels in the tissue.

In the following section we present the results of synthetic experiments conducted on three classes of materials: (I) linear elastic; (II) non linear hyperelastic; and (III) time dependent, with a comparison between a viscoelastic and a poroelastic response.

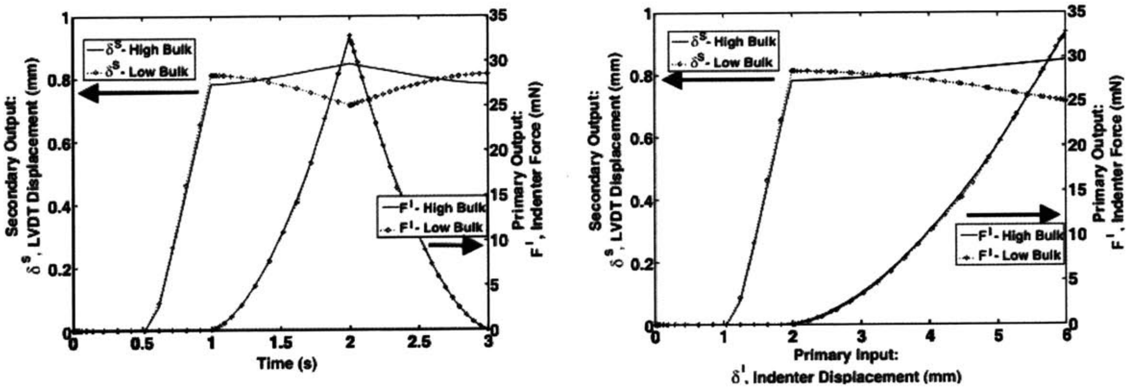

Figure 4-5: Linear elastic results

4.4 Simulations results of secondary sensor additions

4.4.1 Case I: Linear elastic response

Simulations of indentation tests with the integrated secondary sensors were performed for two linear elastic materials with different degrees of compressibility. Material A was modeled as nearly incompressible, with a shear modulus G=1kPa and bulk modulus K=100kPa, corresponding to a Young's modulus E=3kPa and a Poisson's ratio ν=0.495. For Material B, we considered a much higher volumetric compliance, with a shear modulus, G=2kPa and bulk modulus K=1.8kPa, corresponding to a Young's modulus E=4.4kPa and a Poisson's ratio ν=0.1. We selected a combination of elastic properties for the two materials which result in nearly identical force versus displacement responses at the indenter, as shown in Figure 4-5. A conventional indentation test would rely on this information only and would not be able to discern between the two materials. In Figure 5 we also show the displacement signals from the secondary sensors, which clearly reflect differences between the two cases. In the high-bulk case (Material A), the material resists any change in volume and flows in the radial direction towards the region underneath the secondary sensor. The secondary sensor tip is displaced upwards (shortening the LVDT spring) during the loading step, as recorded by the increase in δ^S(t). In the compressible case, the material accommodates the displacement imposed by the indenter with a volume change, the secondary sensor tip travels downwards, and δ^S(t) decreases.

4.4.2 Case II: Hyperelastic response

Compressibility effects were also investigated for a nonlinear hyperelastic constitutive response. The ABAQUS built-in model for Arruda-Boyce hyperelasticity was used in these simulations. The constitutive relation is based on an eight chain representation of the underlying macromolecular network structure, with non-Gaussian statistics for the behavior of individual chains. The eight chain model accurately captures the cooperative nature of network deformation while requiring only three material parameters, an initial shear modulus, limiting chain extensibility, and a bulk modulus [29].

Material A was modeled as nearly incompressible, with an initial shear modulus, μ=0.8kPa, a bulk modulus, K=100kPa and a locking stretch, λ_m=1.25. In the small strain regime, these properties correspond to a Young's modulus, E=2.4kPa and a Poisson's ratio, ν=0.496. The properties for material B were selected to provide nearly identical indenter response, with a similar initial shear modulus μ=1kPa, a much lower bulk modulus, K=1kPa, and a tighter locking stretch λ_m=1.1. In the small strain regime, these properties correspond to a Young's modulus, E=2.25kPa and a Poisson's ratio ν=0.125.

The force versus displacement response of the indenter, as shown in Figure 4-6, is similar for the two materials. Differences between the secondary sensor signals are pronounced, following trends analogous to the linear case, with the secondary sensors displacing upwards for the incompressible case and downwards for the compressible case.

4.4.3 Case III: Poroelastic vs. Viscoelastic Response

In the final study, two different dissipative responses, viscoelastic and poroelastic, were investigated. Deformation resistance in these two material types is controlled by different mechanisms which give rise to the time-dependent behavior. For Material A, a built-in viscoelastic model was used, with elastic properties G=1kPa and K=4.2kPa, and a time-dependent shear response implemented using a single time-domain Prony term (G_1=0.4, τ_1=0.5). For the poroelastic case, Material B, the analysis was performed using the SOILS procedure in ABAQUS [29][88]. A shear modulus and bulk modulus G=1.56kPa and K=1.27kPa were assigned to the porous elastic matrix. Permeability was considered dependent on void ratio. The permeability was set to k=1.8e-4kg/N-s for the initial void ratio ϕ=3, and varied linearly to a value k=1e-7kg/N-s

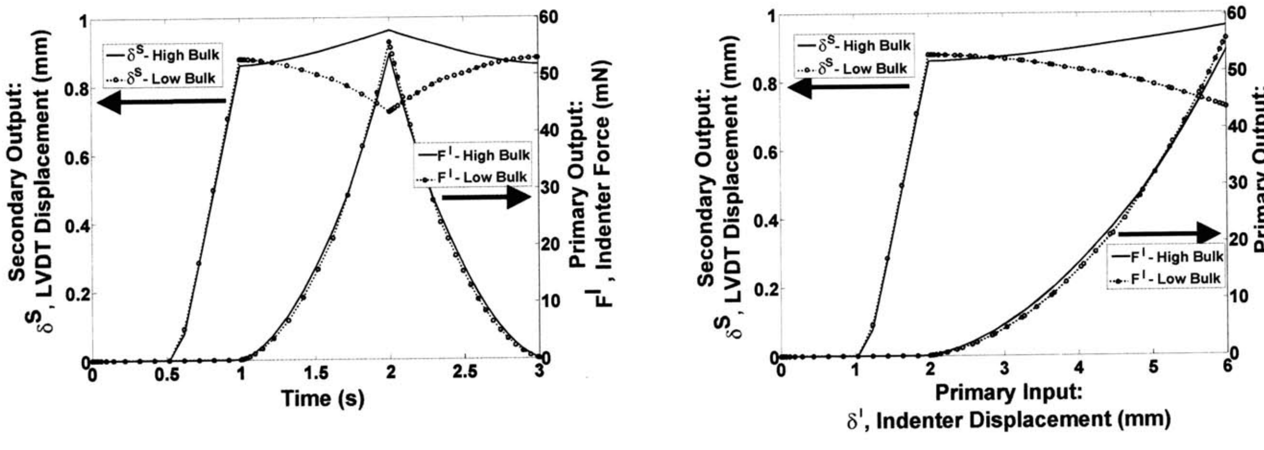

Figure 4-6: Hyperelastic simulation results

for a void ratio ϕ=1. The results for these simulations are shown in Figure 4-7. Again, the two sets of properties were selected to provide matching indenter response, and differences between the two materials are only manifested in the secondary output.

4.5 Secondary sensor discussion

The essential steps of material characterization through traditional indentation techniques are: (1) collect a set of force-displacement histories; (2) based on the characteristics of the experimental data, select an appropriate constitutive framework; (3) solve the "inverse problem", i.e., identify the corresponding material properties by fitting constitutive model prediction to the time-force-displacement data. The synthetic-experiment results presented in the previous section illustrate the inability of the force-displacement output to differentiate between bulk and shear contributions to the material response. The "inverse problem" is inherently under constrained, and the full 3D material response cannot be reconstructed based on these data alone. Even in the simplest case of a linear elastic isotropic constitutive framework, two materials (A and B) with bulk moduli that differed by two orders of magnitude were indistinguishable. For materials with a time-dependent response, the underlying mechanism (visco- vs. poro-) governing the material dissipative behavior cannot be discerned. We believe that these shortcomings

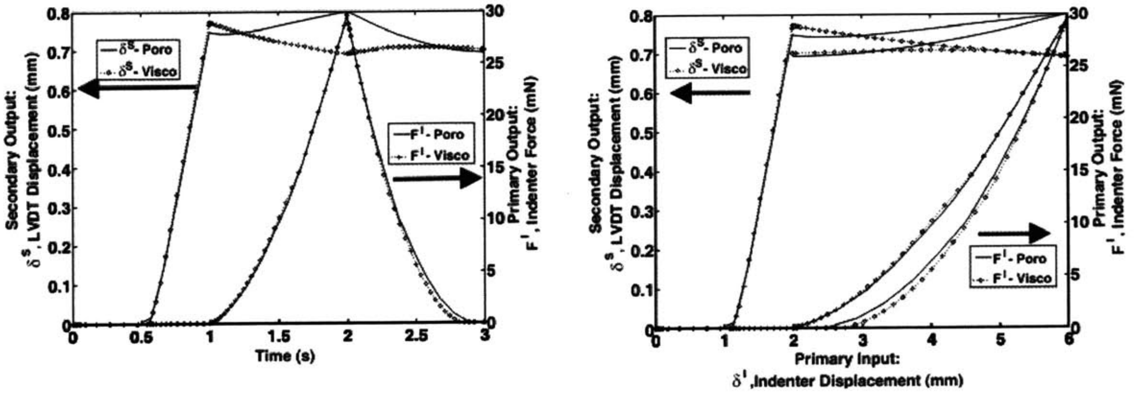

Figure 4-7: Poroelastic and viscoelastic simulation results

can be addressed by the proposed modification to the conventional indentation protocols.

The testing protocol using the DIST tool mirrors the traditional one, but primary and secondary outputs are recorded, and the inverse problem is further constrained by the requirement of fitting both sets of data simultaneously. The quality of the signal from the secondary sensors can be improved by "tuning" the LVDT spring stiffness to the properties of the tested material. In the sample tests presented in the previous section, the imposed initial interference between the material and the secondary sensor was 1.5mm (3.5mm collar displacement - 2.0mm initial clearance). By examining the LVDT displacement output, we note that the selected LVDT stiffness (3.5N/m) resulted in an initial spring compression equal to, approximately, half of the imposed interference. We found this to be a good compromise between two conflicting constraints. If the LVDT spring stiffness is too high, the initial interference is predominantly accommodated by indenting the material, and the change in length of the spring is small. Subsequent changes in the LVDT displacement caused by small movements of the material surface might be below the sensitivity of the sensor. On the other hand, reducing the LVDT spring stiffness to very low levels provides diminishing advantages as, in the limit of zero stiffness, the LVDT would simply measure the displacement of the (unloaded) free surface. This advantage has to be weighted against the need to overcome frictional effects between the plunger and the housing of the LVDT sensor. For high-frequency applications, inertial effects need to be considered as well when selecting appropriate stiffness levels. For the case of time-dependent

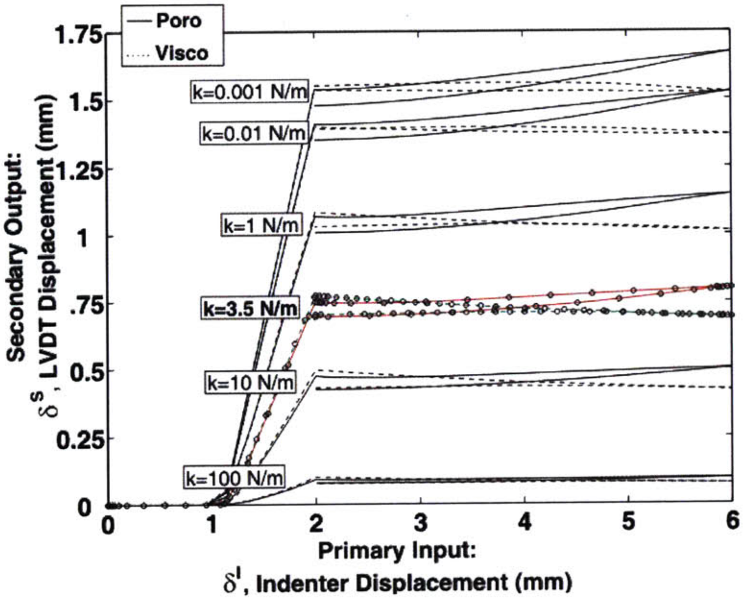

Figure 4-8: Parametric study to determine optimal spring stiffness

material response (poroelastic vs. viscoelastic), Figure 4-8 illustrates the secondary output corresponding to levels of LVDT stiffness ranging over five orders of magnitudes.

For the highest stiffness level (k_{LVDT} = 100N/m) the initial LVDT change in length is only 0.1mm. The difference (poro- vs. visco-) in LVDT displacements at the end of the loading step is, approximately 20 μm, which is starting to approach the resolution levels ($\sim$1 μm) of commercial miniature LVDTs. Decreasing the LVDT stiffness to k_{LVDT} = 1N/m increases the magnitude of the displacement signal, with a difference in LVDT displacements of 150 μm. Further decreases in stiffness provide diminishing improvements in the magnitude of the signal. Similar considerations led to the positioning of the LVDT sensors in the FE simulations and to the selection of an appropriate level for the initial collar interference.

This chapter provides a preliminary proof-of-concept for an innovative design addition to be integrated with a conventional indentation testing tool.

Among the advantages of the proposed technique are the following:

- The secondary sensors are not independently actuated: the displacement measured by the secondary sensors is directly caused by the material deformation. No additional motors or controllers are needed, so that the tool retains its simplicity and ease of operation.

- The secondary sensors measure deformation in the indenter's near field, so that the combination of primary (indenter force) output and secondary (sensors) output provide a more distinctive "signature" for the material response.
- The conventional indenter force output and the secondary sensor output are obtained in the course of the same test at one material location: the two responses are synchronized, thus avoiding complexities arising from tissue conditioning.
- The three sensors are arranged around the main indenter at 120 degrees from each other, thus providing additional information as to the orientation of the indenter axis with respect to the material.
- The method is modular, whereby the secondary sensor location with respect to the indenter and the LVDT spring stiffness can be adapted to different testing conditions and material compliances.

Chapter 5

Validation of Secondary Sensor Concept

In the previous chapter, we introduced the concept of adding a secondary displacement sensor to track surface deformations as the main indenter deforms the material. The proof of concept was presented; the concept has yet to be validated on a material with known properties. The objective of this chapter is to incorporate this design addition into the large deformation dynamic indentation tool and utilize the secondary sensor when testing brain tissue in vivo.

5.1 Design of validation tools

In order to validate the concept, a testing apparatus to house the secondary sensors around the main indenter was designed. The apparatus was designed to accommodate the ElectroForce (ELF) tester and to fit within the footprint of the ELF machine. As discussed in the previous chapter, the simulations were done with the sensors arranged around the main indenter at 120° from each other. The apparatus design allows for the sensors to be placed 120° from one another at 40 discrete locations radially (ranges from 10mm to 40mm) from the main indenter (Figure 5-1). It was important that each secondary sensor mounting bracket was designed to be stiff enough so as to not deflect upon indenter motion into the tissue. The objective of the secondary sensors is to measure the surface deformation and therefore the mounts were designed to minimize any error due to frame deflection. A FE analysis for the mount was performed

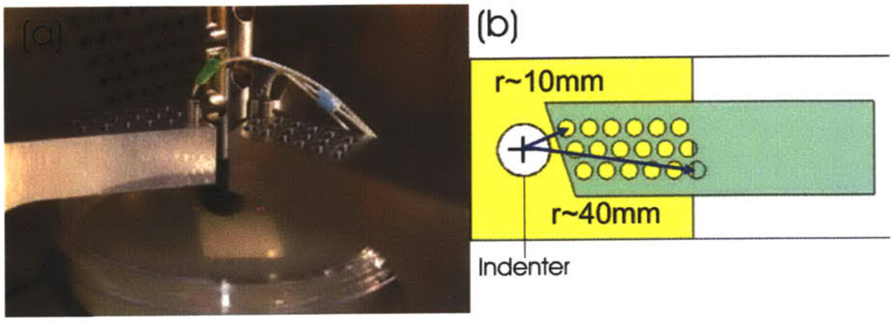

Figure 5-1: Experimental setup for validating secondary sensors on ElectroForce Machine: (a) Isometric view (b) Top view showing discrete sensor position locations

to ensure that deflections were small (on the order of .8μm) compared to the measurement resolution (1.5μm) of the secondary sensor. A contour plot of this analysis is shown in Figure 5-2.

In addition, the design maintains tight tolerancing and minimized the tolerance error stack up in the vertical direction so that the bottom face of the sensing portion were all within a 10μm tolerance of each other. Each sensor is threaded individually into the bracket and can be advanced or retracted by simply turning the sensor. In a three-sensor scenario each sensor should be advanced to approximately the same vertical position as the other two sensors such that the initial starting positions of each sensor is the same. This ensures adequate range of motion to capture the surface deformation of the material.

5.2 Validation on stiff materials

5.2.1 Spring sensor

In the previous Chapter, the theoretical effect of varying the spring stiffness of the secondary sensor in the simulations shown (Figure 4-8). It is clear from this figure that a sensor with a larger stiffness would compress or extend a smaller amount than a sensor of a smaller stiffness. The necessary stiffness depends highly on the compliance of the material being tested. In addition, there is a lack of commercially available sensors within the appropriate stiffness range (k=0.001N/mm to k=0.01N/mm) for testing soft tissues. The initial secondary sensors chosen

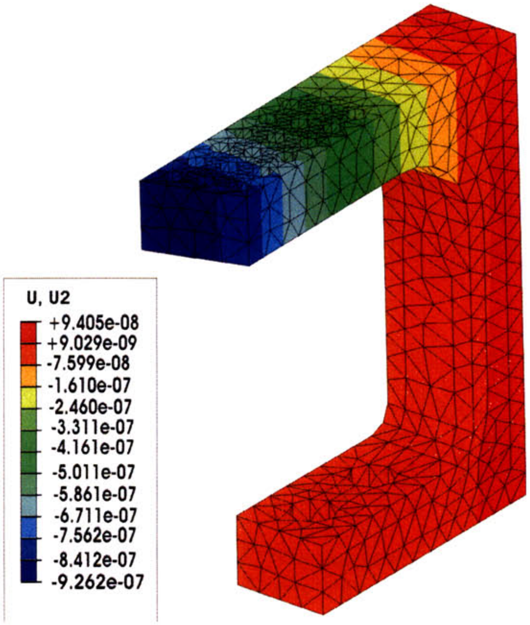

Figure 5-2: Finite element contour plot of vertical displacement of secondary sensor mounting bracket

were the 3mm microminiature gaging differential variable reluctance transducers (DVRTs) from Microstrain (Williston, VT). The resolution of the sensor is on the order of 1.5μm and contains a spring constant with stiffness=0.2N/mm. This stiffness is higher that the spring stiffness of the simulations from Chapter 4, but this sensor is the only LVDT commercially available with a low stiffness and with miniature geometry. A description of the sensor and its configuration when integrated into the ELF tool is provided in Figure 5-3.

5.2.2 Aquaflex

As a first-pass experiment, only one sensor was used to validate the concept. A material that of the same order of stiffness as the sensor was selected. Because the load capacity necessary to test this material can only be accommodated by the ELF Machine, experiments were conducted on the ELF tool apparatus The ELF Machine has a load capacity on the order of 10N, whereas the load capacity of the DIST Tool is limited to 2.25N for continuous motion. The DIST tool was designed for softer materials such as brain tissue, and would not accommodate materials

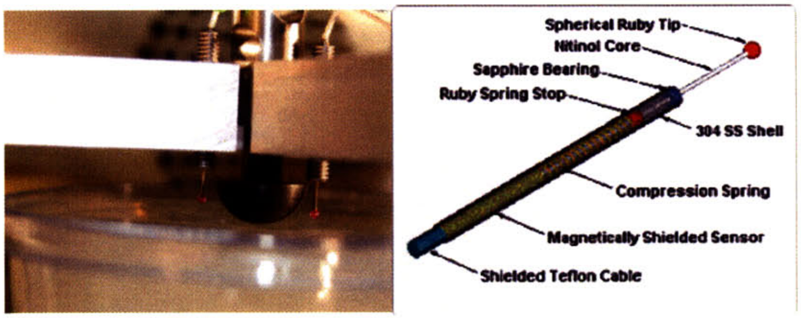

Figure 5-3: Image and description of spring-loaded sensor integrated into ElectroForce apparatus

with a higher stiffness. The material chosen was a water-based gel called Aquaflex (Parker Laboratories, Fairfield, NJ), which is an ultrasound gel pad that is used to calibrate ultrasound probes. Initial uniaxial compression tests indicate that the Young's Modulus is on the order of 200kPa for this nearly incompressible material and the forces on the indenter for imposed strains were on the order of 5 to 15N. A spherical indenter of diameter 12.5mm was used in all experiments.

Indentation experiments without the sensor were initially performed to get a baseline force-displacement response of the material. Data was recorded for indenter displacements ranging from 4 to 8mm (Figure 5-4). The same experiments were performed adding the secondary sensor at 12mm away from the indenter tip. The results showed that while the rate of change of the secondary sensor displacement varied with the depth of indentation, the change in depth did not vary greatly. This is likely because the stiffness of the sensor spring is too high. Even on a stiffer material, the change in displacement of the spring was minimal. Figure 5-5 shows the results of the secondary sensor displacement (right axis) for a given indenter force (left axis). From the results of this study, it became apparent that a sensor with a much smaller stiffness, or no stiffness would be the most ideal; especially when testing softer materials such as brain tissue.

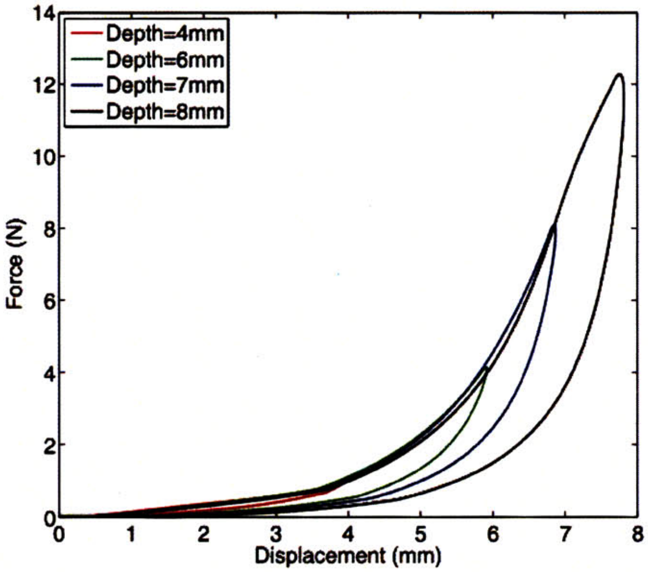

Figure 5-4: Force-displacement response for indentation testing to different depths on Aquaflex

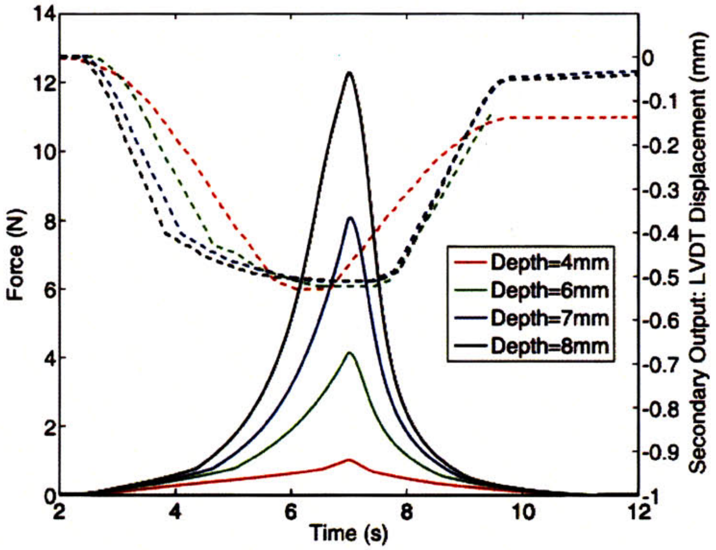

Figure 5-5: Force history for indenter (left axis) and displacement history (right axis) for secondary sensor

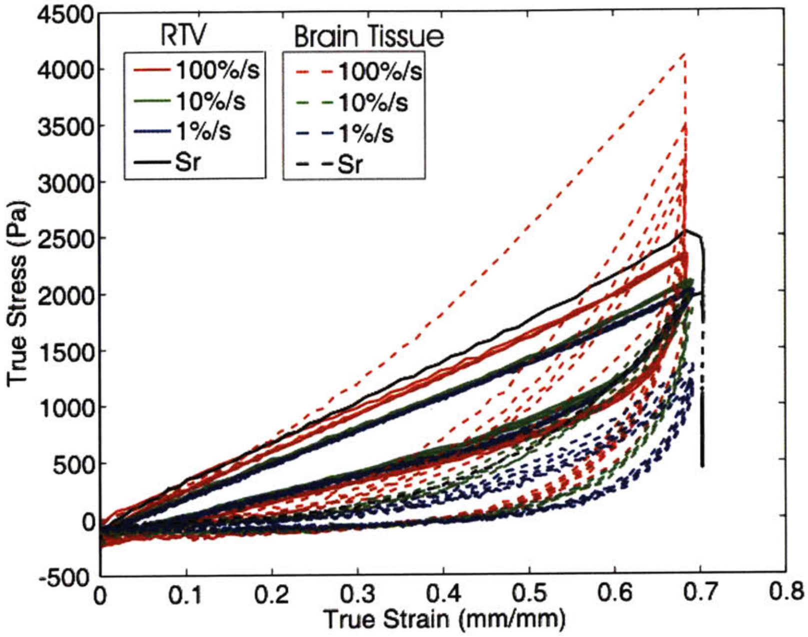

Figure 5-6: Stress-strain response for RTV and brain tissue tested in uniaxial unconfined compression

5.3 Validation on soft tissue simulant

In the next step of validating the addition of the secondary sensor, we chose a gel phantom material, RTV 6166 (GE Silicones, Wilton, CT) cast in a 1:1 composition. The material is of the same order of stiffness as brain tissue and is repeatable in nature. RTV 6166 is a well-accepted soft-tissue simulant often used in the literature to mimic the behavior of soft tissue [34][35]. Figure 5-6 shows the stress-strain curve of both brain tissue and RTV 6166 (1:1) tested in unconfined compression. Although the behavior is not identical, the stiffness of the RTV is very similar to that of brain tissue making it an adequate stable simulant for verifying instrument designs.

The material was cast to make unconfined compression and indentation specimens. To validate the experiment, the following process was used: assuming a linear elastic material, a range of material properties from the uniaxial compression tests was identified. A simulation of the indentation experiment with the secondary sensor was performed and the material properties of the simulation were adjusted to fit the experimental response. These material properties were then compared to the range of material properties determined using uniaxial compression.

5.3.1 Unconfined compression

Specimens of the RTV 6166 (1:1) were tested in uniaxial unconfined compression using the ELF machine. The size of each specimen was 25.4mm by 25.4mm and the height was between 5-7mm. A series of loading and unloading displacement cycles were applied to each sample. A nominal strain of 50% for each sample was applied at three different loading rates for five cycles at each rate, with no settling time between cycles. The first 5 cycles were tested at 100%/s (1.00Hz), the next 5 cycles were tested at 10%/s (0.10Hz) and the last cycles were tested at 1%/s (0.01Hz). Immediately following the load-unload protocol, a stress relaxation test was performed at the highest loading rate (100%/s or 1Hz) and held at a strain of 50% for 5 minutes (300s). Figure 5-7 graphically describes the strain history for this protocol.

The stress-strain response for the RTV 6166 for the strain history of Figure 5-7 is presented in Figure 5-8. The results show some degree of hysteresis, rate dependence, and nonlinearity; however there seems to be no conditioning of this material as seen in biological materials [26]. The stress relaxation results are given in Figure 5-9.

Although the results do not indicate that a linear elastic model will capture all aspects of the material behavior, as a first pass, we approximated the response as isotropic linear elastic to determine the material constants. To obtain three-dimensional behavior, a video extensometer system was used. Lateral displacement data was collected with a Qimaging Retiga 1300 CCD camera equipped with a 200mm f/4 Nikon lens. Strain data were, obtained with Digital Image Correlation (DIC) techniques using the Correlated Solutions VIC-2D (version 4.4.0) software. A more detailed description of the experimental procedure is given in Chapter 6.

$$\varepsilon_{vol} = \frac{\Delta V}{V_o} \tag{5.1}$$

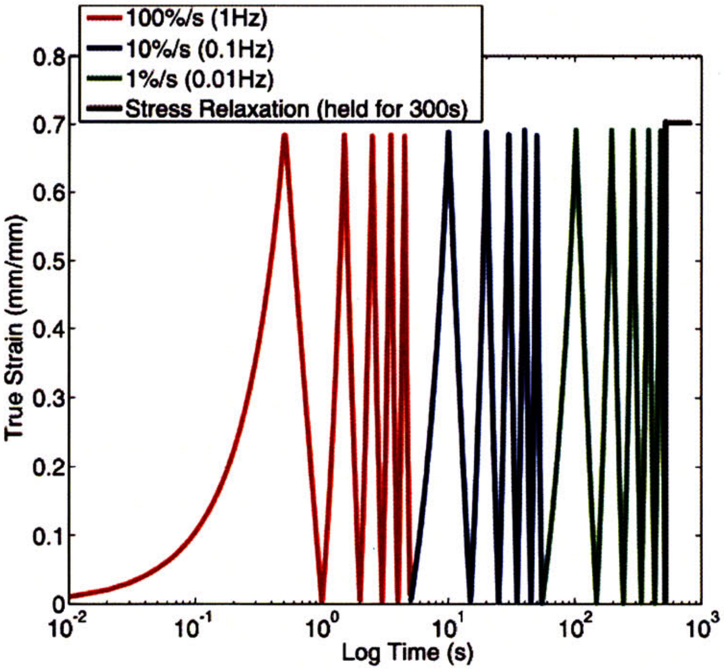

Figure 5-7: Strain history for uniaxial unconfined compression experiments for RTV 6166 specimens

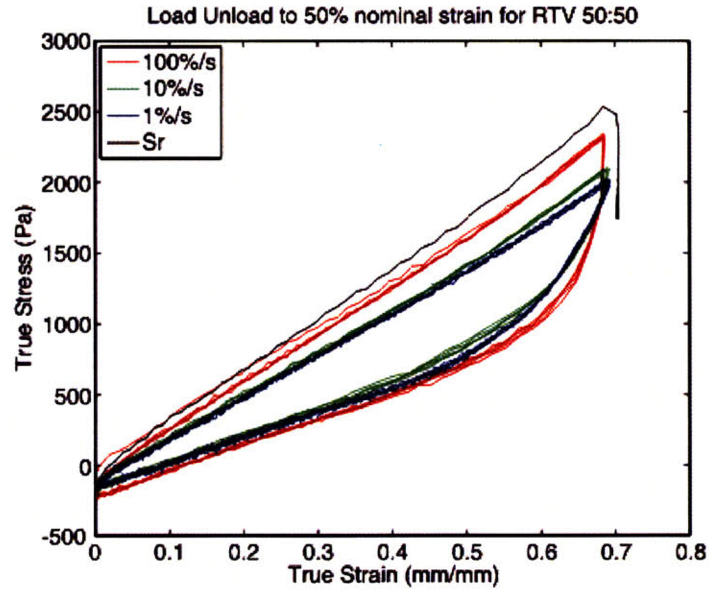

Figure 5-8: Stress-strain behavior for RTV 6166 (50:50) tested in uniaxial unconfined compression

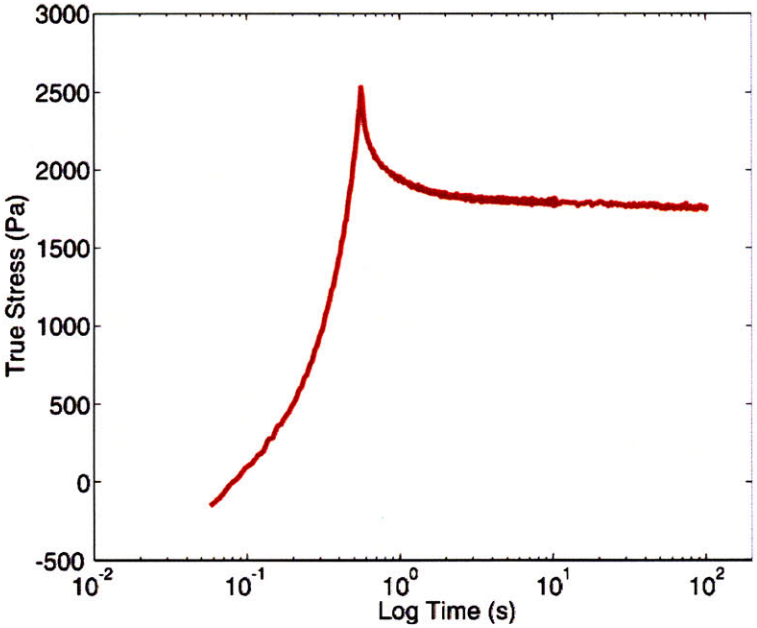

Figure 5-9: Stress relaxation response for RTV 6166 (50:50) tested to 50% strain in unconfined compression at 100%/s loading rate

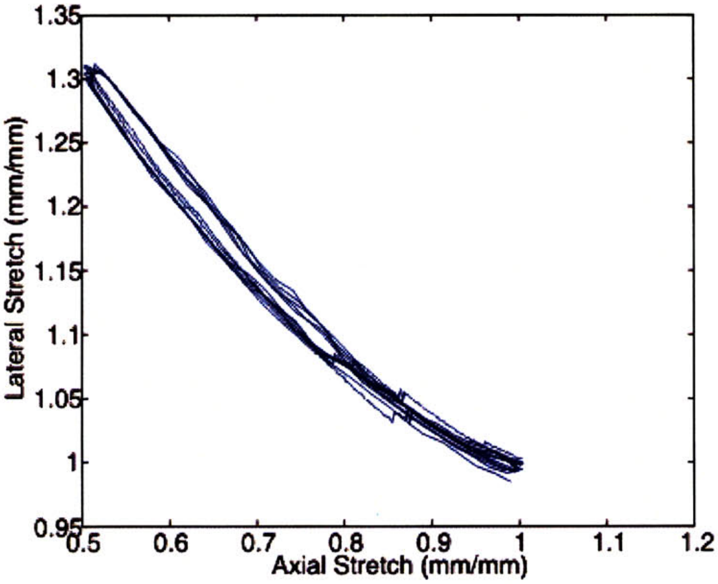

Figure 5-10: Lateral vs. axial stretch response for RTV 6166 50:50 tested to 50% nominal strain

$$K = \frac{P}{\varepsilon_{vol}} \tag{5.2}$$

The resulting lateral stretch for the RTV uniaxial compression tests (50% nominal strain) are given in Figure 5-10. The volumetric strain, ε_{vol}, is given by Equation 5.1 and determined from the lateral stretch data. The bulk modulus, K, is defined as the ratio of hydrostatic pressure, P, to the relative volume change, ε_{vol}, as shown in Equation 5.2.

$$G = \frac{3K}{9(\frac{K}{E} - 1)} \tag{5.3}$$

$$\nu = \frac{E}{2G} - 1 \tag{5.4}$$

For isotropic, linear elastic materials, the shear modulus, G, is related to the bulk modulus, K, and the Young's modulus, E, based on Equation 5.3, and Poisson's Ratio, ν,is given by Equation 5.4. The calculated material property constants based on this linear elastic assumption

Volumetric Strain, ε_{vol}	0.14
Bulk Modulus, K	4800-5000Pa
Young's Modulus, E	3000-4000Pa
Shear Modulus, G	1100-1250Pa
Poisson's Ratio, ν	0.4-0.49

Table 5.1: Estimated RTV 6166 (50:50) material properties

are given in Table 5.1.

To assess the linear viscoelastic properties of RTV 6166 (1:1), rheometry tests on 25.4mm diameter specimens were conducted on the AR2000ex rheometer (TA Instruments, New Castle, DE). Frequency sweeps at different strains were first performed to determine when the response is no longer within the linear elastic regime. For this material, the response remained linear for strains up to 10%. Figure 5-11 plots the frequency sweep for RTV 6166 at strains of 1-10%. At low frequencies (~0.1-1Hz), the shear modulus is 1250Pa, a value consistent with the calculated shear modulus using linear elastic theory.

5.3.2 Indentation experiments

Following the uniaxial unconfined compression experiments, the RTV 6166 (1:1) was tested in indentation. Indentation experiments similar to those performed for the Aquaflex were conducted. For the indentation experiments, the RTV 6166 (1:1) was cast to a diameter of 90mm and a height of 14mm in a round dish. Because of the tacky nature of the material, it remained in contact with the side of the dish, and no vertical sliding was allowed. A new secondary sensor was also placed at a pre-determined distance away from the 12.5mm-diameter spherical indenter. The selected secondary sensor was a smooth running sensor (no spring) with a displacement range of 9mm (MicroStrain, Williston, VT). A 6mm diameter cylindrical tip was added to the #00-90 threaded end of the sensor to assist in keeping the sensor in contact with the material (see Figure 5-12).

Initial indentation experiments were conducted, but due to the tackiness of the surface, the repeatability of the experiments was unsatisfactory. To smooth out the indentation response and improve the repeatability, a thin paraffin film was added to the top of the material and the experiments were repeated. The addition of the paraffin film appeared to address the repeata-

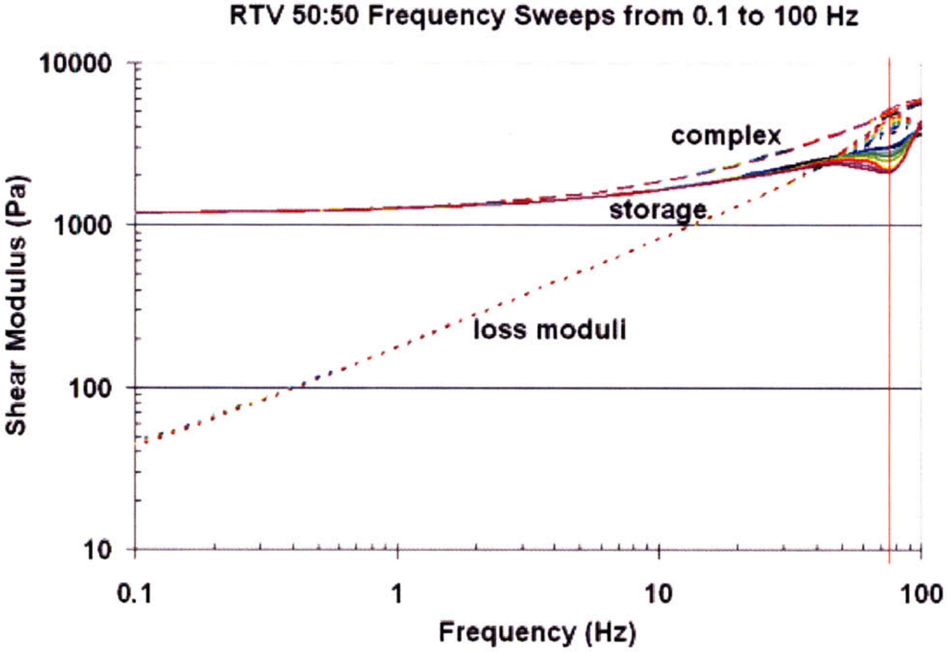

Figure 5-11: Rheometer data for RTV 6166 at small strains (1-10%)

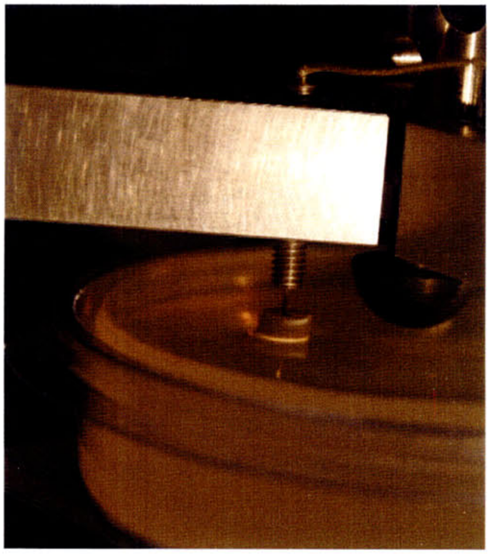

Figure 5-12: Indentation apparatus with secondary sensor (without spring)

bility issue and the experiments were conducted using this thin film. To better understand the effectiveness of the secondary sensor addition, the following parametric studies were performed: a) depth of indentation study, b) frequency study and c) sensor location study. For the depth of indentation study, the sensor was placed at 17.5mm away from the indenter and the indenter was loaded with a sinusoidal input at a frequency of 0.1Hz. The force-time responses for four depths of indentation were recorded. As expected, the change in displacement of the secondary sensor increased as the depth of indentation increased (see Figure 5-13). Additionally, the direction of displacement change should be noted. A positive change in displacement of the sensor corresponds to a compression (or shortening) of the displacement sensor. Interpretation of this data suggests that the sensor compressed as the depth of indentation increased. The material displayed a behavior more consistent with an incompressible material. For the frequency study, the indentation experiment was performed at a location 17.5mm away from the main indenter, a depth of indentation of 4mm and at 4 different frequencies of oscillation (0.01Hz, 0.1Hz, 1Hz and 5Hz). The objective of this study was to show that the secondary sensor would respond through a wide range of operating frequencies for the main indenter. The results of the study are shown in Figure 5-13, on a log time scale.

Lastly, a study of the sensors location radially away from the indenter was performed. These results are more material dependent, and indicated information about the compressibility of the material and the optimal placement of the sensors to measure the motion of the surface at their maximum amplitude. Results for this study are shown in Figure 5-14 and indicate that for all the locations tested, the location of 17.5mm away from the main indenter was optimal. The study was performed at both 0.1Hz and 1Hz to demonstrate that changes in frequency would not alter the results. The visual correlation to each of the sensor locations tested is shown in Figure 5-15. The colors at the different locations correspond to the colors of the locations on Figure 5-14. The sensor was able to record displacements at locations ranging from 12.5mm to 22.8mm; however when placed at 28mm away from the indenter, the sensor no longer tracked surface deformations.

These three parametric studies were done to validate the secondary sensor as a device for measuring surface deformation, and results from all three studies verify the concept. The next step is to simulate the indentation and show that by solving the inverse problem and using

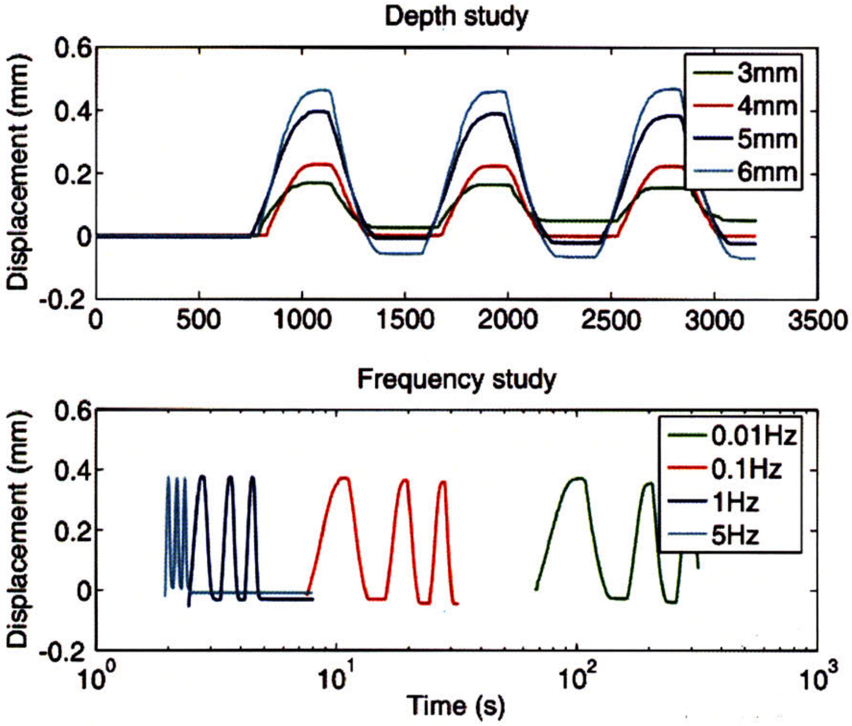

Figure 5-13: Depth and frequency dependence studies of the secondary sensor testing for indentation testing of RTV 6166 (50:50)

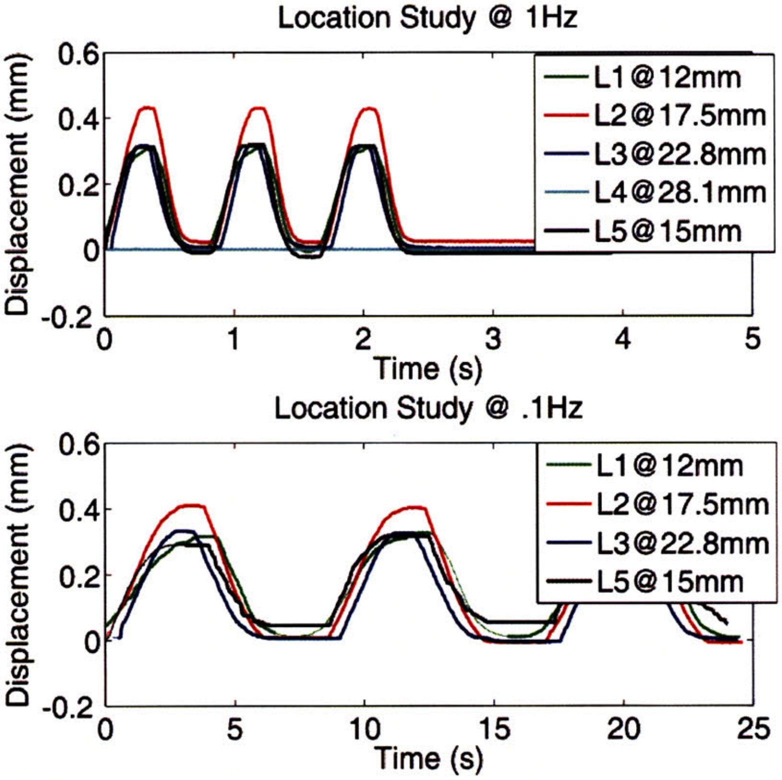

Figure 5-14: Secondary sensor location study

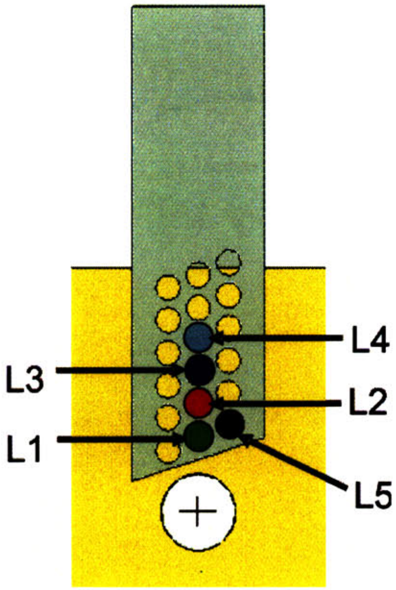

Figure 5-15: Top view of the secondary sensor mounting bracket describing sensor locations

the experimental force and secondary displacement measurements, material properties may be obtained.

5.3.3 Indentation simulation

After determining the material properties from the uniaxial unconfined compression experiments of the RTV 6166 (1:1) (see Table 5.1 in Section 5.3.1), a simulation of the indentation experiments was conducted. A three-dimensional ABAQUS simulation of the indenter and secondary sensor was built to be dimensionally consistent with the indentation experiments described in the previous section. To reduce computation time, 1/6 of the model was simulated. To simulate the thin paraffin film that was added to the material during experimentation, a thin skin made of shell elements was added to the model. The stiffness of the sensor spring was set to 0.001N/m, which simulated a smooth running sensor. The input parameters to the simulation included: a 5mm depth of indentation, a location of indentation at 17.5mm away from the main indenter and a frequency of indentation of 0.1Hz. Consistent with the linear elastic assumption made for RTV 6166 (1:1), a linear elastic material for the indented material

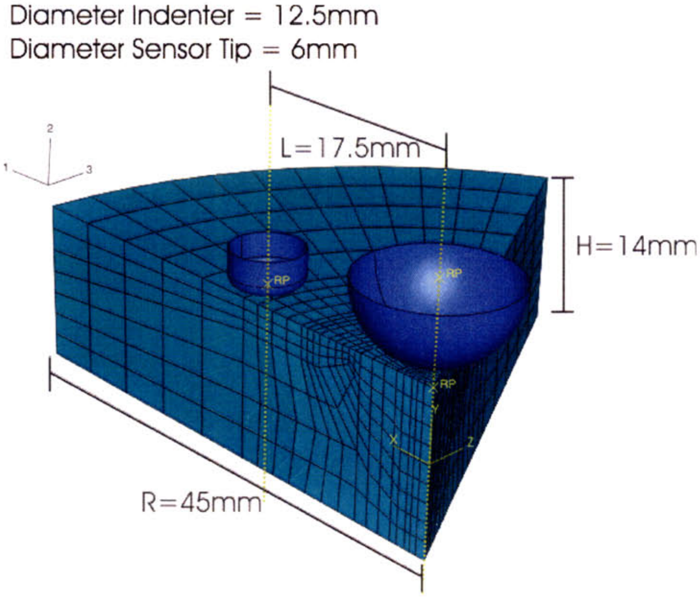

Figure 5-16: Three-dimensional simulation of indentation with secondary sensor experiment

in the simulation was also assumed. Figure 5-16 shows an image of the three-dimensional model used in the simulation.

The addition of the skin resulted in an increased experimental force, and using a linear elastic model for a surface film, we simulated the effects of the skin and checked the prediction against the experiment. To determine the model's material properties of the skin, indentation experiments without the secondary sensor were performed on the RTV 6166 both with and without the skin. First, the simulation was performed without the skin and the material properties of the gel were adjusted until the force-displacement response of the material matched the experimental force-displacement response. Once those properties were determined, they remained constant and the skin was added. The skin's linear elastic properties were then determined such that the force-displacement response of the simulation matched the indentation experiment with skin. Figure 5-17 shows the experimental results and the simulation fit with and without the skin added to the top of the gel material.

The model fit agrees well with the experiments. To obtain this fit, $\mathrm{E}_{gel} = 4000Pa$, $\nu_{gel} = 0.49$, $\mathrm{E}_{skin} = 100000Pa$, and $\nu_{skin} = 0.49$. After determining these material properties, the secondary sensor was added to the simulation as shown in Figure 5-16. A contour plot of the

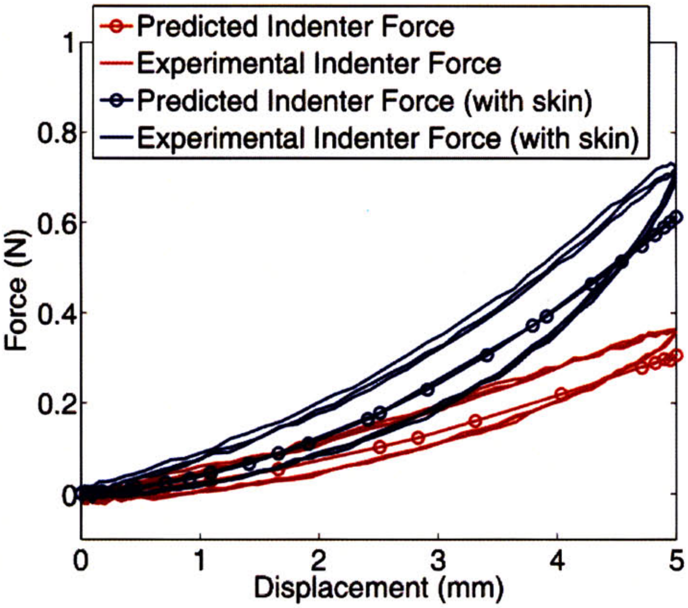

Figure 5-17: Experimental and model results for pure indentation tests with and without the skin

simulation is shown in Figure 5-18.

A comparison plot between the experiment and predicted indenter force-time and secondary sensor displacement-time output is shown in Figure 5-19. The force output on the main indenter matches quite well and the result of the secondary sensor displacement are within 15% of each other. The error or discrepancies in this result can be attributed to the fact that a linear elastic model was assumed, there is friction in the LVDT shaft, that the complexities of adding the paraffin film as a skin are not completely understood, that the indentation tool operates in sinusoidal mode while the simulation was done for the indenter motion at a constant displacement rate, and there was a frictionless contact assumption made in the model. To obtain this fit, the material properties of the gel were adjusted to $E_{gel} = 4500$Pa with a $\nu = 0.49$ to match the experimental result.

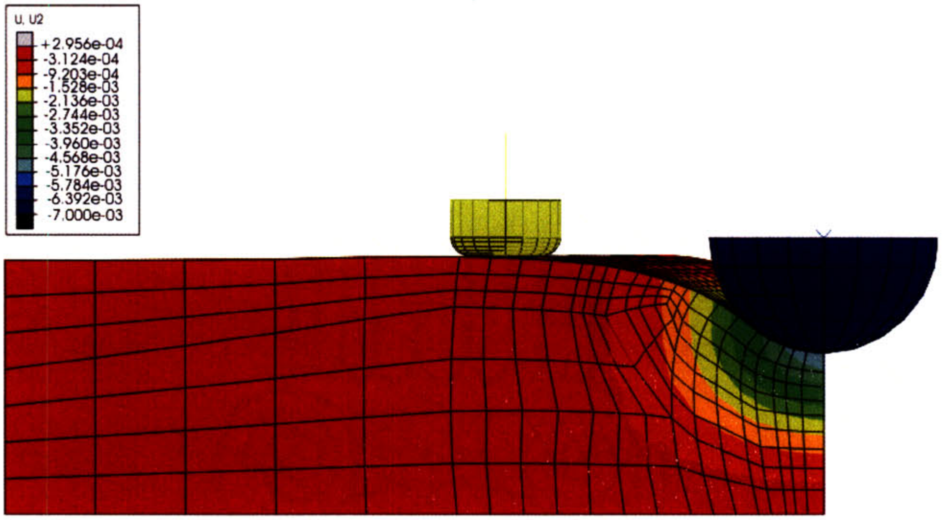

Figure 5-18: A contour plot of the indenter at the fully extended position

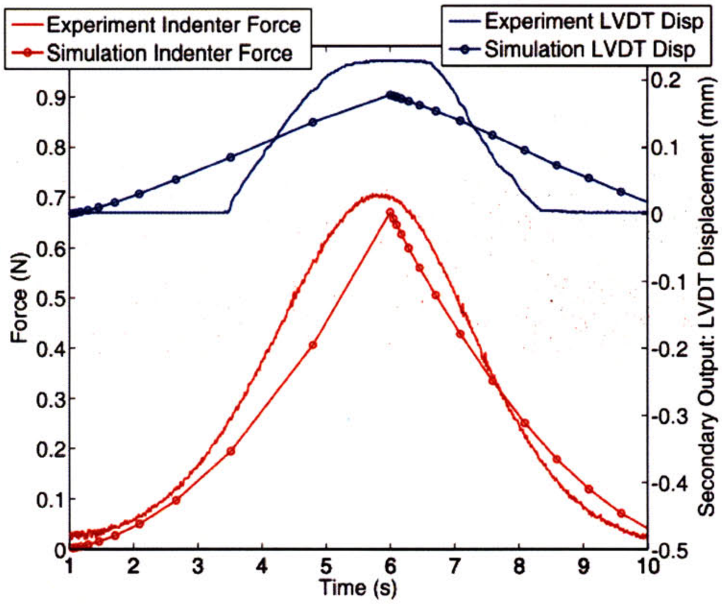

Figure 5-19: Comparison between the experimental results, and simulated indenter force and secondary sensor displacement response on RTV 6166 (50:50)

5.4 Conclusions

The procedure used to determine the material properties by matching the simulations of the indenter and secondary sensor to the experimental response is consistent with the simulation performed in the previous chapter. The results of this validation study indicate that adding the secondary sensor to enrich the indentation force signal during classical indentation tests of soft materials (i.e. biological tissues) will aid in understanding the interplay between the bulk and shear responses of the material. The example used in this chapter focused on a material of higher incompressibility, and the mere direction of the secondary sensor response assists in establishing general assumptions about the compressibility of the tested material. The actual displacement of the secondary sensor helps determine the finer details of the material's compressibility.

Chapter 6

In Vitro Porcine Brain Tissue Testing

In order to gain insight into the mechanical response of porcine brain tissue, experiments on tissue samples were conducted. Because in vivo studies are costly and challenging to arrange, initial investigations to understand the specific features of the in vitro mechanical response to uniaxial unconfined compression and indentation are performed.

6.1 Methods of in vitro testing

In vitro experiments were performed on 3-month-old yorkshire pigs obtained from a local slaughter facility (include average weight, age, gender, and time of death as seen in Table 6.1). Brain halves were kept on ice during transport and upon arrival at the laboratory, they were placed in a 1X solution of Phosphate Buffered Saline (1X PBS) to prevent dehydration and to impede tissue degradation. The brain was sectioned down the mid-sagittal plane and one half was retained for indentation testing while the other half was sectioned for uniaxial compression testing. We conducted a preliminary study on samples from the cortical region to identify optimal specimen sizes and configuration. Samples containing both white and gray matter were selected in order to obtain approximate homogenized properties of the cortical regions. The samples were prepared from tissue located in corpus callosum region within 6 hours of sacrifice. The compression specimens were sectioned in the sagittal plane, and a portion of white matter from the mid-sagittal region of each half was removed from the specimen.

6.1.1 Compression experiments

Investigations of ideal sample size were conducted. Cylindrical samples varying from 8mm to 20mm were initially investigated. Smaller cylindrical samples were made on 10mm thick slices using an 8mm biopsy punch. Due to a large thickness to diameter ratio, this method created samples that were more hourglass-shaped than cylindrical. Using a custom-made coring device, larger samples of 20mm were attempted. The coring device was actuated using a hammer and samples were punched from one of the brain hemispheres. This method is less than ideal in that the resulting samples were still too small to create a relatively homogenous specimen, and the folds of the fissures were often found to be unfolding rather than staying intact while loading the specimen. The next specimen preparation attempt was done using a hinged cutting device with a stainless steel surgical cutting blade that made larger (25.4mm x 25.4mm) specimens. This method proved to be the most repeatable and the straight blade made cleaner edges than the other coring methods. The base mat used for cutting the brain hemisphere shows a quarter-inch grid, allowing for the sample to be accurately cut into 25.4mm-square specimens in length and width. Figure 6-1 shows the freshly cut brain tissue specimen as well as the position of the sample while being tested. The height of each specimen varied slightly and was recorded using the displacement measurement of the testing machine.

The samples were tested on the ElectroForce 3200 (Bose Corporation, Natick, MA); a dynamic mechanical analyzer with a load capacity of 22N and displacement range of 12mm. The load cell was positioned below the sample and thus did not record inertial forces induced by the test. In order to assess volumetric effects of the tissue, a video extensometer was used. This allowed us to visualize the lateral strains thereby allowing for insight as to the volumetric behavior of the tissue. Video extensometer data were collected using a Qimaging Retiga 1300 CCD camera equipped with a 200mm f/4 Nikon lens. Strain data were obtained through Digital Image Correlation (DIC) techniques using the Correlated Solutions VIC-2D (version 4.4.0) software. The image setup is shown in Figure 6-2. The bottom platen in the system is manually adjusted whereas the top platen is attached to the shaft of the motor and is controlled using the machine. To accurately measure the height of each sample, the top

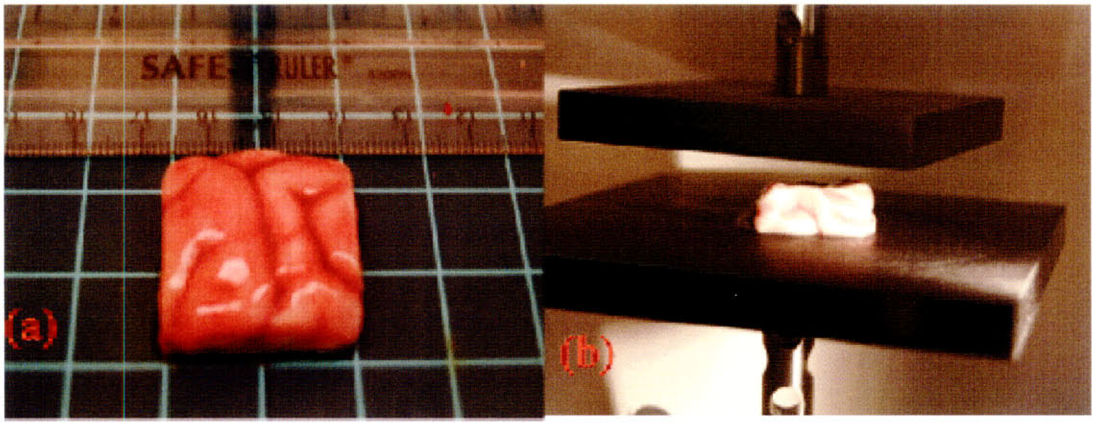

Figure 6-1: Brain Tissue: (a) Freshly cut square brain tissue specimen, (b) Brain tissue specimen prior to loading in ElectroForce machine

platen was lowered to its minimum height and the bottom platen was brought into contact with the top to determine the zero position. After the top platen was raised to a nominal position, the specimen was placed on the bottom platen and the force was zeroed (Figure 6-3). The top platen was then brought into contact with the top of the specimen until the force measurement changed 0.010N, and this location was then taken as the initial height of the specimen. The video extensometer also proved to be a useful verification tool for measuring the initial lateral dimension of the specimen. Prior to testing, the samples were kept in PBS to maintain hydration. During testing, the platens were coated with PBS to create frictionless conditions.

A series of loading and unloading displacement cycles was applied to each sample. The specimens were loaded to 50% nominal strain at three different loading rates, for five cycles at each rate, with no settling time in between cycles. The first 5 cycles were tested at 100%/s (1.00Hz), the next 5 cycles were tested at 10%/s (0.10Hz) and the final cycles were tested at 1%/s (0.01Hz). Immediately following the load-unload protocol, a stress relaxation test was done at the highest loading rate (100%/s or 1Hz) and held at a strain of 50% for 5 minutes (300 s). Figure 6-4 shows the displacement history profile of this protocol. The aim of this protocol was to investigate the effects of pre-conditioning and strain rate dependence of samples tested at high strain on the load-unload behavior of the material. Initially, this investigation tested

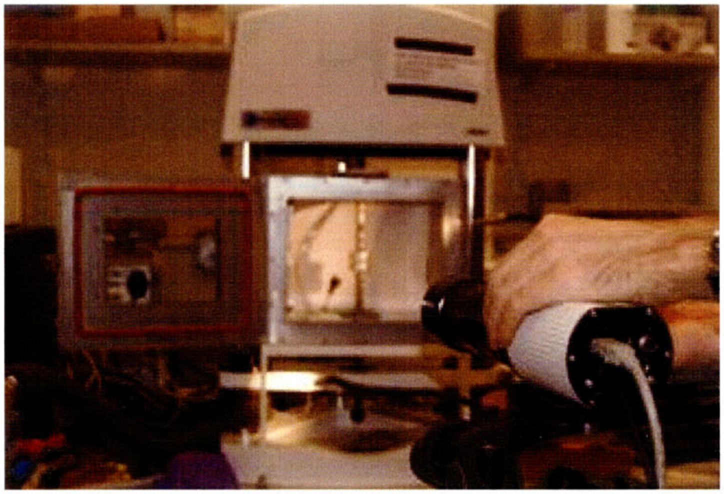

Figure 6-2: Bose ElectroForce 3200 dynamic mechanical tester with video extensometer

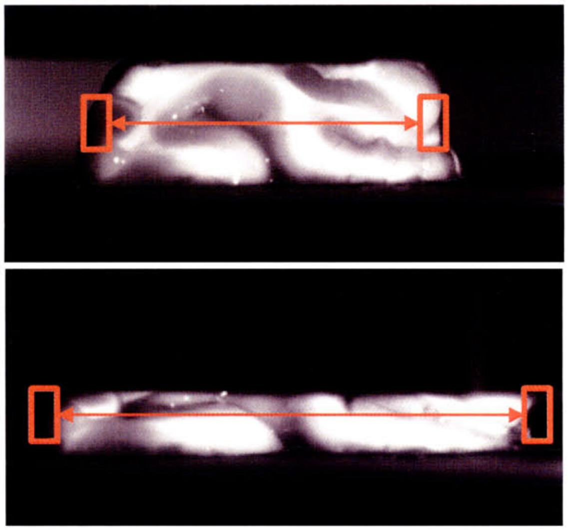

Figure 6-3: Video extensometer data acquisition

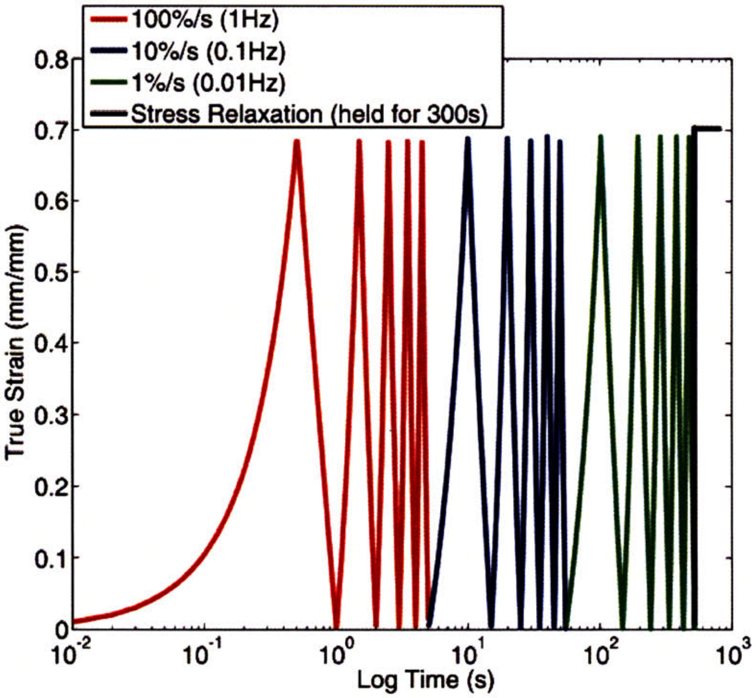

Figure 6-4: Strain (true) history for in vitro porcine brain tissue specimens testing in uniaxial compression

the brain tissue at strain rates of 1000%/s as well, however at these higher rates a perfect tuning of the PID for the control system of the machine was critical in order to minimize noise and vibrations.

6.1.2 Indentation experiments

Subsequent to the unconfined compression tests, indentation tests were performed on the remaining hemisphere of each brain specimen. The hemisphere was placed in a 50mm x 50mm container and kept hydrated using 1X PBS. The surface of the cortical region of the brain was also kept hydrated by occasionally adding PBS. A 12.5mm-diameter spherical indenter was attached to the ElectroForce machine and used for all indentation testing (Figure 6-5).

The purpose of the spherical indenter was to create a more continuous contact region. The indentation tests were typically performed at 3 different regions of the cortical surface. Initially, tests were repeated in order to understand the ability of the tissue to recover. It was

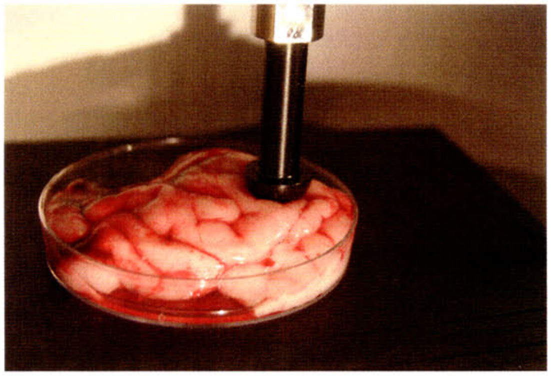

Figure 6-5: Indentation on a porcine brain hemisphere using a 12.5mm-diameter spherical indenter

discovered that the tissue would typically not recover within the testing period, therefore the cortical surface was never tested at the same location. The indentation displacement history, as shown in Figure 6-6, generally resembles that of the uniaxial compression displacement history. The differences are that the total depth of indentation was always set to 6.5mm for every brain sample tested and the specimens were not loaded at a constant rate. The in vivo tool developed for testing was designed to perform sinusoidal indentation, therefore the displacements for the indentation tests were sinusoidal with time. The tuning of the PID is also more favorable with a sinusoidal loading history because the motion controller does not need to accommodate instantaneous changes in direction as required with a triangular (constant rate) loading profile. The first 5 cycles were tested at 100%/s (1Hz), the next cycle was tested at 10%/s (0.1Hz), the final load-unload cycle was tested at 1%/s (0.01Hz) and finally the stress relaxation test was performed by imposing a displacement of 6.5mm and holding the indenter in position for 5 minutes (300s).

The displacement history for the indentation protocol is shown in Figure 6-6. Following the indentation testing, the indented tissue was cut into compression samples in order to determine whether the tissue fully recovered after being indented. The same unconfined compression protocol (as described above) was applied to these samples, and the results were compared to freshly cut samples.

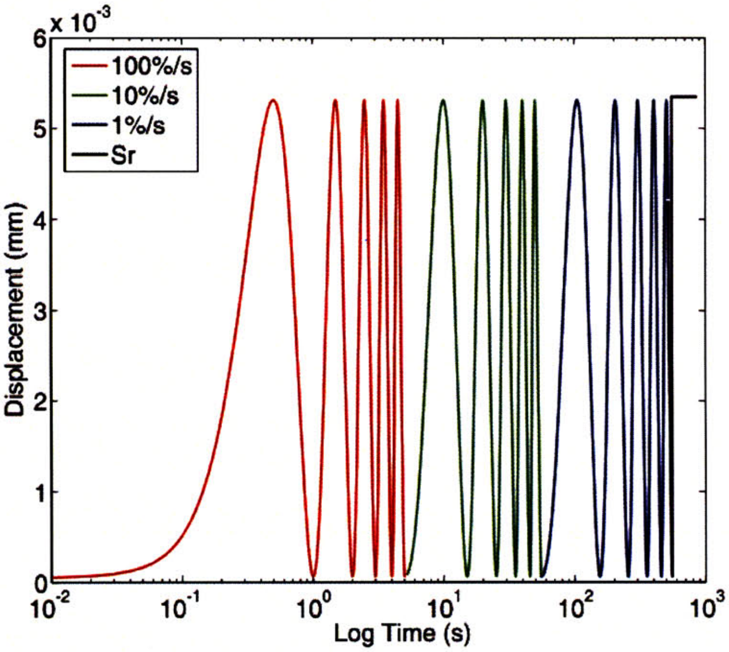

Figure 6-6: Displacement history for in vitro indentation experiments on a hemisphere of porcine brain tissue

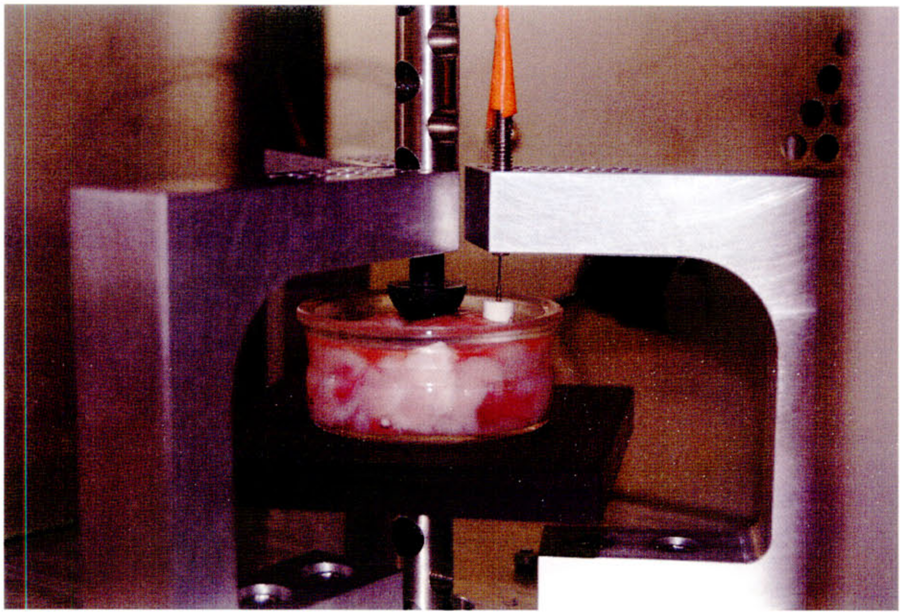

Figure 6-7: Setup of indenter and secondary sensing device testing brain tissue on ElectroForce Machine

6.1.3 Indentation with secondary sensor experiments

The goal of adding the secondary sensor was to capture the volumetric response of the tissue to the indentation loading. Indentation testing using the secondary sensing device was conducted on the ELF machine using the experimental setup described in Section 5.2. Figure 6-7 shows the experimental setup.

One hemisphere of the porcine brain was placed in a 44mm-diameter cylindrical glass dish which constrained the radial motion of the tissue. The total height of the specimen in the dish was approximately 22mm. Both the indenter and the secondary sensor were brought into contact with the tissue. Because the surface of the brain is not flat, it is possible that the vertical starting position of the indenter and the secondary sensor would start at different planes. To test the effectiveness of the secondary sensor, the tissue was indented by 5mm at 1Hz for 5 cycles. Upon initiating this protocol, the resulting indenter force and change in displacement of the secondary sensor were recorded. The future design of incorporating three secondary sensors at 120° apart will assist in ensuring orthogonal loading; however in the current design, only one sensor was used.

The repeatability of the response when placing the indenter and secondary sensor at different locations relative to the specimen was observed. In addition, the effect of indentation depth on the force and secondary sensor response was observed by performing experiments at four different depths, 2mm - 5mm. The results for these experiments are presented in the following section.

6.2 In vitro results

The results of this in vitro study are unique; no other studies have been performed at the prescribed large strain as well as the relatively large strain rates. Much of the brain tissue results in the literature refer to specimens that were tested at high frequencies (0-100Hz) and low strains (order of 0.1-1%) or high strains (10-20%) and lower frequencies (0.1Hz). In this work, we aim to fill this gap of learning more about brain tissue behavior in the regime of relatively large deformations and higher strain rates.

6.2.1 Results: Uniaxial unconfined compression

The results of the aforementioned study of unconfined compression and indentation were in good agreement with each other given a tightly defined protocol and a systematic approach to testing each specimen. The brains obtained from the slaughterhouse yielded approximately 13 square (25.4mm x 25.4mm) specimens. A description of all the specimens tested is shown in Table 6.1.

Most uniaxial compression specimens were tested within 6 hrs of sacrifice. In one case, the brain was tested one day (24h) after sacrifice. Also, all but one of the specimens were obtained from a young Yorkshire swines of approximately three months age. Specimen D was from an older female swine that was larger in size and the results from those specimens are noticeably higher in stress as compared to the smaller Yorkshire samples. The mean values for all specimens excluding specimen D in the form of true stress and strain with the corresponding standard deviations are given in Figure 6-8.

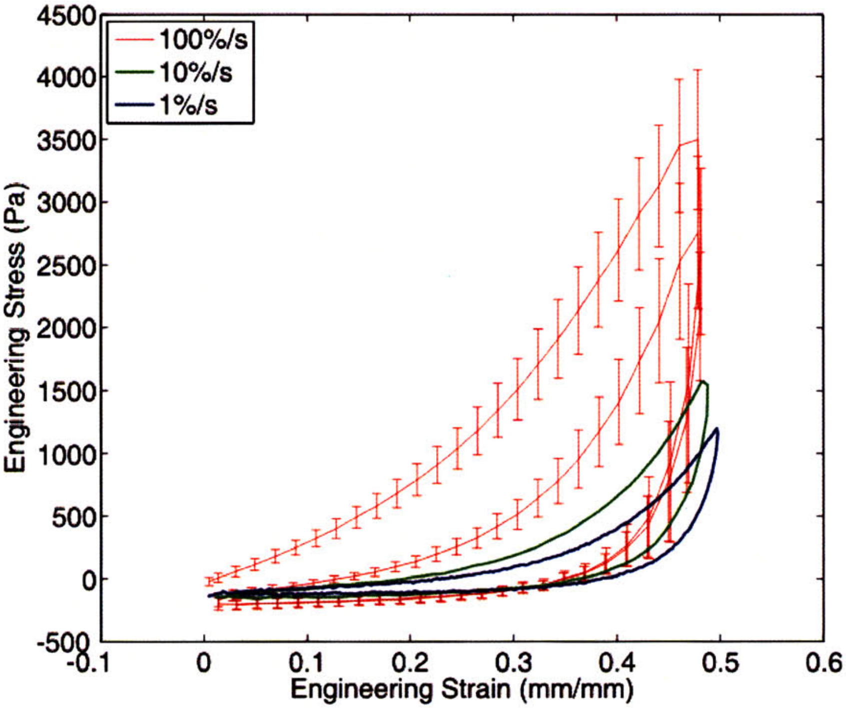

Figure 6-8: Load-Unload mean with standard deviations for nine specimen tested in uniaxial unconfined compression

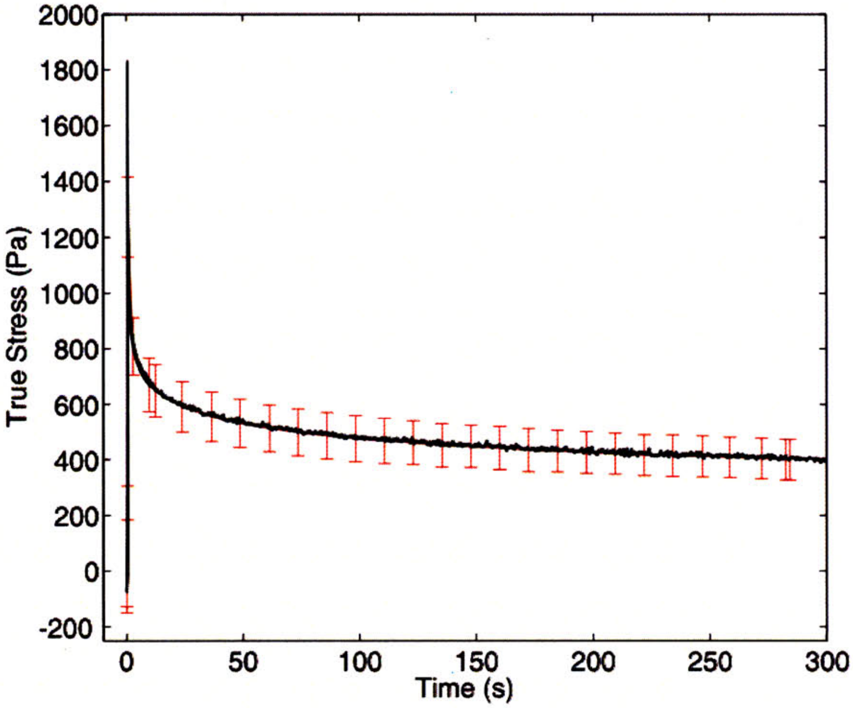

Figure 6-9: Stress relaxation mean and standard deviation for 9 samples of porcine brain tissue tested in uniaxial compression

n	Brain ID	State F=Fresh I=Indented	Location p=Parietal f=Frontal	Post-mortem time (hrs)	Type	Age (months)	Weight (kg)
1	B	F	p	24	Yorkshire	3	30
2	B	F	f	24	Yorkshire	3	30
3	B	I	p	24	Yorkshire	3	30
4	B	I	p	24	Yorkshire	3	30
5	F	F	f	6	Yorkshire	3	30
6	F	I	f	6	Yorkshire	3	30
7	F	I	p	6	Yorkshire	3	30
8	H	F	f	6	Yorkshire	3	30
9	H	F	p	6	Yorkshire	3	30
10	D	F	f	6	Lorac	18	90
11	D	F	p	6	Lorac	18	90
12	D	I	f	6	Lorac	18	90
13	D	I	p	6	Lorac	18	90

Table 6.1: Comprehensive description of in vitro compression specimens

Figure 6-10 shows the resulting stress history for the strain history given in Figure 6-4 for a representative sample of brain tissue. There are several aspects of these results that must be further discussed. As explained in the earlier section, the specimens were all tested at three different strain rates (100%/s, 10%/s, and 1%/s) at 5 cycles for each. The material exhibits a significant amount of nonlinearity at such high strains (50% nominal, 67% true). Often times brain tissue is modeled as a linear material, but clearly we observe that at such high strains, the material response becomes very nonlinear.

In the initial cycle, we observe a substantial conditioning effect of the material whereby the stress the material exhibits is much higher than the subsequent cycles as seen in Figure 6-11. The remaining cycles still exhibit the effect of conditioning, however, not to the same degree to which the initial cycle experiences it. Another observation is of material's strain rate dependence; whereby the samples tested at higher rates experience higher stresses, while the testing at the lower rates cause the material to respond at lower stresses. This is clearly seen by the responses given in different colors for different rates in Figure 6-11. The final strain input is that given by the stress relaxation. The stress relaxation ramp is performed at 100%/s, the same strain rate as the first five cycles. However, this is done after testing at the 10%/s and 1%/s rates are completed. Because the material is viscoelastic and viscous strain accumulates

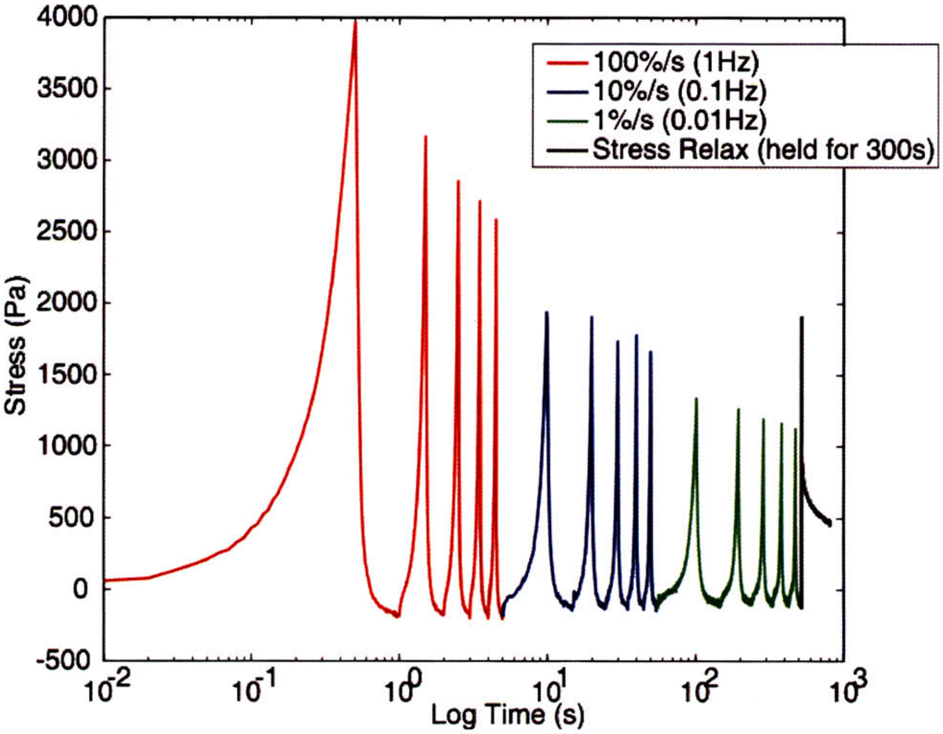

Figure 6-10: Resulting stress history from strain history given in Figure 6-4 on a representative specimen of brain tissue

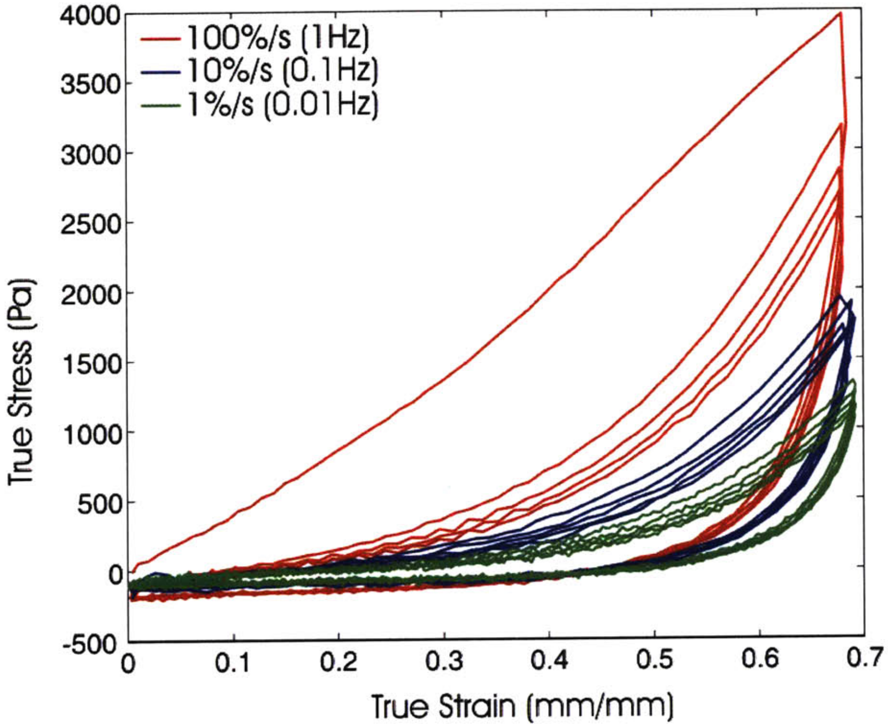

Figure 6-11: Representative stress-strain result of a specimen tested in uniaxial compression

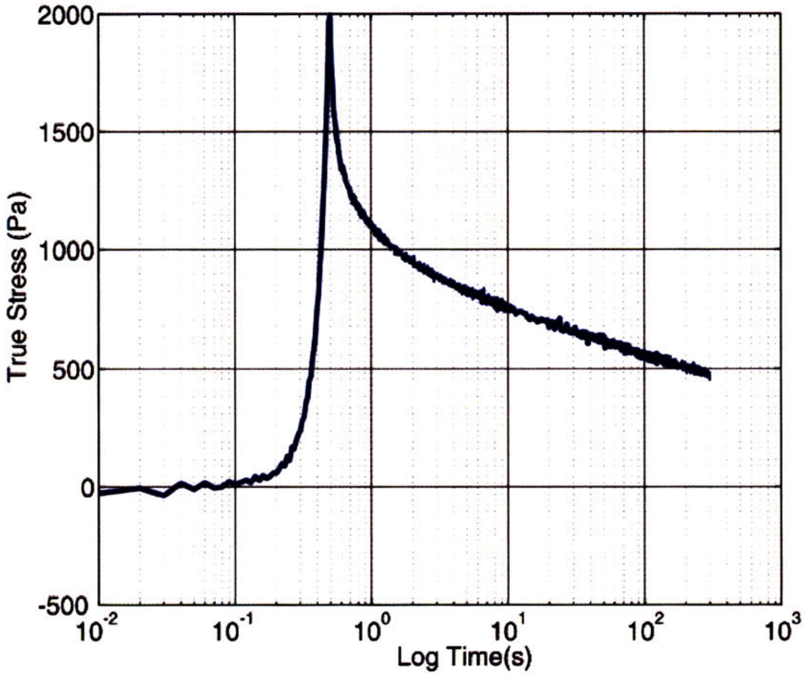

Figure 6-12: Stress relaxation results from a representative sample tested in uniaxial compression

throughout the loading history, the peak stress for the stress relaxation cycle is significantly lower than the fifth cycle performed at 100%/s.

Another interesting characteristic of this material is the dramatic drop in stress when the unloading begins to occur. The viscous strain in the material is not instantaneously recovered upon reversal of the displacement rate, and the elastic unloading causes a dramatic decrease in the stress in a very short time frame. Also from Figure 6-11, the time dependence of the material is indicated by the hysteresis loops. The degree of hysteresis is dependent on the rate at which the material is being tested. At higher strain rates, the hysteresis loops are larger because the viscous deformation cannot be entirely recovered in the unloading segment. A more detailed expansion of the resulting stress relaxation is shown in Figure 6-12. The stress relaxes dramatically in the first 10 seconds, and then continues to relax at a slower rate for the remaining 290 seconds of testing.

We observed that the differences seen between samples taken from the frontal and parietal regions of the brain were within the standard deviation given in Figure 6-8. Additionally, the samples that had been freshly used for compression versus those compression samples made from the already indented brain hemispheres displayed no statistically significant difference in behavior. We conclude from this observation that there are no detectable differences between regions of mixed (gray/white) matter tissue. We also conclude that the viscous deformation of the tissue recovers within a 1 hr period as that was the minimum time between testing an indented brain hemisphere and cutting it to test in compression. In an earlier section, it was stated that indentation tests at the same location on the cortical surface resulted in a slightly varied response, therefore indentation tests were always performed on a new site. This leads us to believe that the tissue takes somewhere up to about 1 hour of time to recover.

As stated earlier, the results from Brain D were eliminated in the mean and standard deviation results because the age difference between the animals was about 15 months. This age effect can be seen on Figure 6-13 where the peak stress at 100 %/s is nearly 75% higher than that of the average sample. Prange *et al.* confirm the difference between material response due to age of the animal [25][66].

Using the CCD Camera, video extensometer data was collected. Lateral stretch data was recorded by creating a spatial field in which the brightness of the sample edge can be clearly identified. The location of that field over the history of loading is recorded (see Figure 6-3).

The volumetric stretch evolution was recorded as seen in Figure 6-15. Figure 6-14 shows that while the sample is being compressed and the axial stretch is reducing to 50%, the lateral stretch is increasing by 26% yielding a 14% change in volume over the loading and unloading of the specimen. Incompressible materials would exhibit a behavior consistent with volume preservation during the loading cycle of the specimen. Brain tissue is often assumed to be incompressible [[15][26][51]], and the data are inconsistent with that assumption. Friction between the platens and the specimen is a possible source of error in the calculation of volume change. This inherent experimental source of error can be addressed using the method introduced by El-Aguizy et.al in his frictionless compression testing paper [19]. It should be noted that the maximum frame rate capacity of the video extensometer is 200 frames per second, and when testing at 100%/s loading rate, the lateral strain acquisition rate is too small to provide

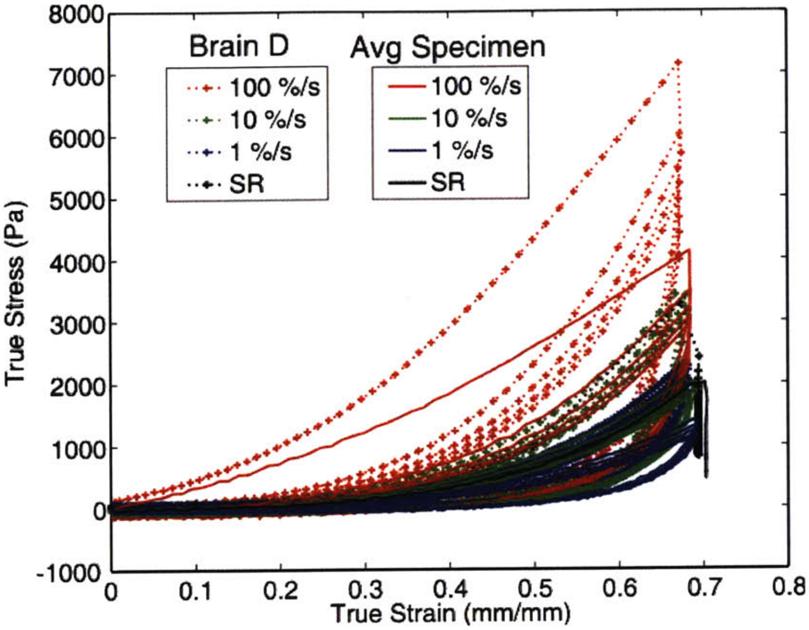

Figure 6-13: Effect of porcine age on material response: comparison between 3 months and 18 months of age

reliable data. Therefore, the lateral strain results from the 10%/s and the 1%/s loading rates are presented. The results presented in Figs.6-8 through 6-15 represent a comprehensive set of in vitro experiments that have been conducted to understand the nature of brain tissue at large deformations and high strain rates. These results will be the bases for the material model presented in Chapter 7.

6.2.2 Results: Indentation

The results of the indentation tests are similar to those presented in the previous section, however the maximum force transitions more smoothly on the load-unload result (see Figure 6-16) because of the sinusoidal displacement input. The same features of conditioning, hysteresis, strain rate dependence and nonlinearity are captured in the indentation force-output.

The result is given in the form of a force-displacement plot rather than stress-strain plots because three-dimensional finite element simulations are needed to determine the stresses and strains associated with this output.

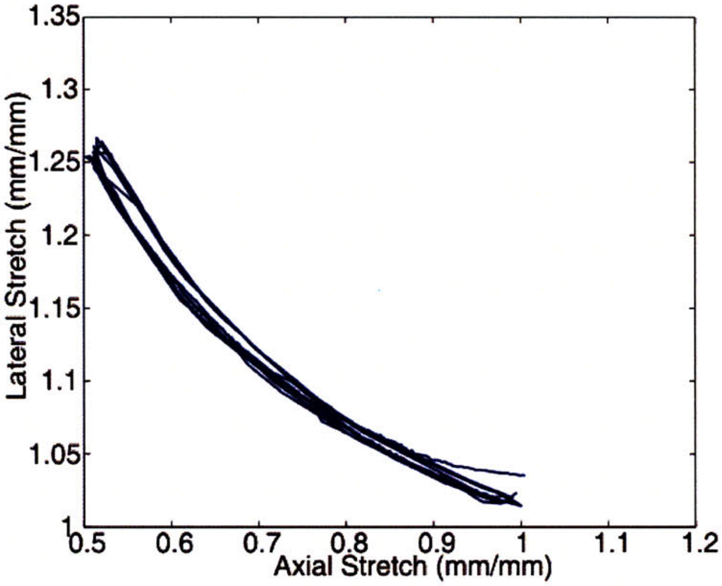

Figure 6-14: Lateral vs. axial stretch for a representative sample of brain tissue testing in uniaxial compression

Figure 6-17 shows the force history for the imposed indenter displacement history given in Figure 6-6. The trends of the material response are similar to those observed in uniaxial unconfined compression.

6.2.3 Results: Indentation with Secondary Sensor Addition

Indentation tests with the additional secondary sensor were repeated as described in Section 6.1.3. The sensor was placed at a distance of 17.5mm away from the indenter and tests were performed at four different locations on the sample specimen. The location of the sensor with respect to the indenter dictated the location of indentation with respect to the sample. The experiment was not done in perfect symmetry because of limited space on the diameter of the specimen (44mm diameter). If the indenter was placed in the center of the specimen, the secondary sensor would be about 4 - 5mm away from the edge of the dish. To avoid edge effects, we decided to offset the specimen from a symmetrical indenter placement. However, the results shown in Figure 6-18 indicate that the effect of changing the location of testing does not effect

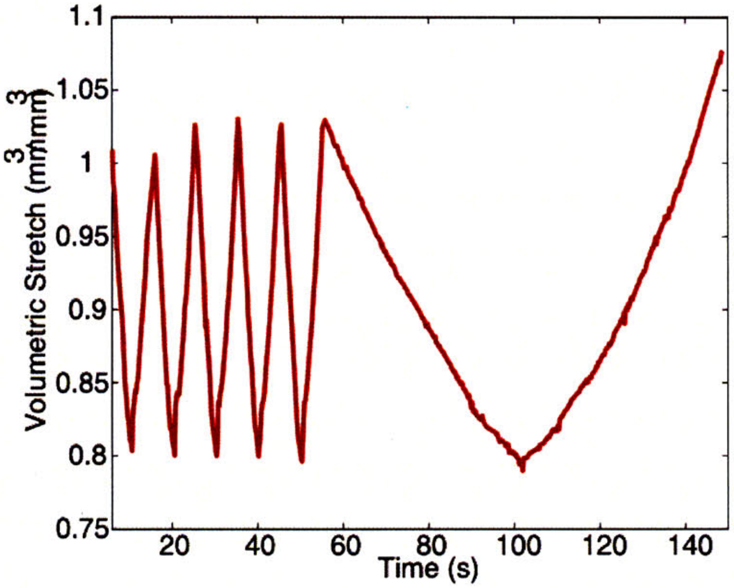

Figure 6-15: Volumetric stretch history for a representative sample of brain tissue tested in unconfined compression

the resulting force or secondary sensor displacement. The force results are within 1 - 2% of each other, and the results for the secondary sensor displacement vary about 12 - 15 %. This 15% variation can be attributed to the inhomogeneity of the material and the non-uniform curvature of the surface as it is sits in the dish. The effect of changing the depth of indentation was also investigated. The indentation depth was increased from 2mm to 5mm, and the corresponding indenter force and secondary sensor displacements were recorded. As expected, the indenter force and the secondary sensor displacement both increased with increasing depth of indentation (see Figure 6-19). This experiment was performed to show the capabilities of the secondary sensor at smaller displacements. At the small depths of indentation, there exists some noise in the the force response. The noise in the force sensor when unloaded was observed to be on the order of 10-15 mN which explains the force signal noise shown in Figure 6-19. The response of the secondary sensor generally follows a sinusoidal form, however as the sensor approaches its maximum displacement, it appears that the displacement remains constant for about 0.25 seconds. Friction caused by the shaft running against the secondary sensor barrell can explain

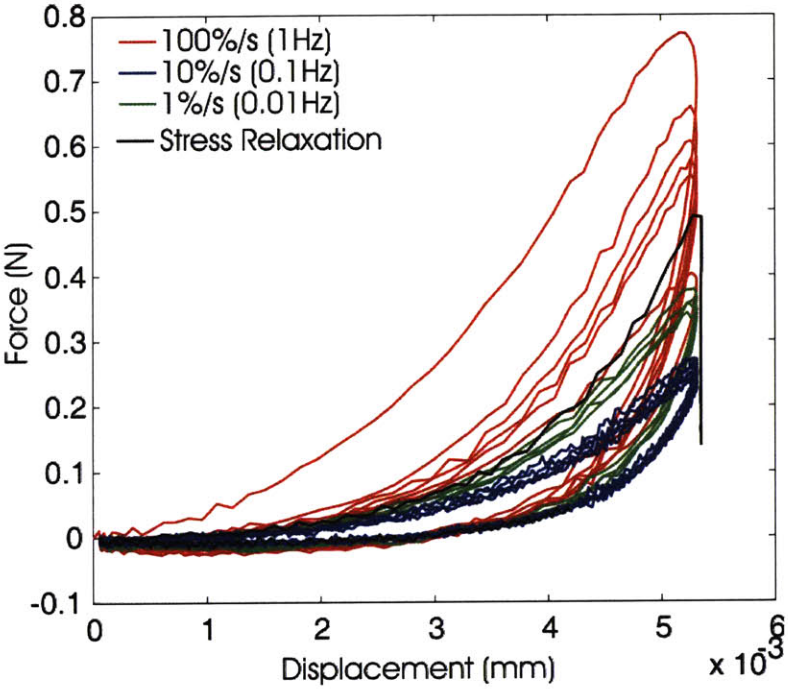

Figure 6-16: Force-displacement response of brain tissue tested in indentation

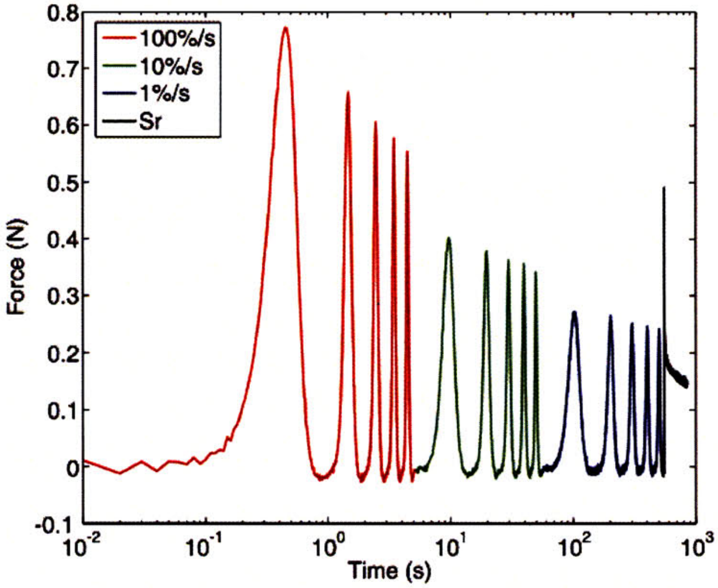

Figure 6-17: Indentation force history response based on strain history input shown in figure 6-6

this effect. In reality, the surface of the tissue is moving during that time period, however, at such small changes in surface displacement, the incremental force is not large enough to overcome what little friction exists in the sensor.

6.3 In vitro brain testing conclusions

In the first set of experiments, unconfined compression and indentation testing were performed on several in vitro brain tissue specimens. These experiments provide a comprehensive understanding of the behavior of brain tissue at large strains in two different modes of deformation (compression, indentation) tested at three different loading rates spanning 2 time decades for five cycles each. Load-unload as well as stress relaxation data are recorded. For the uniaxial compression tests, volumetric behavior of the tissue is evaluated by recording the evolution of lateral strain over the loading cycles. Using this data, the compressibility of the material can be evaluated. Similarly, the results presented in Chapter 4 show that the addition of a secondary surface tracking sensor can theoretically provide volumetric behavior of a material when tested

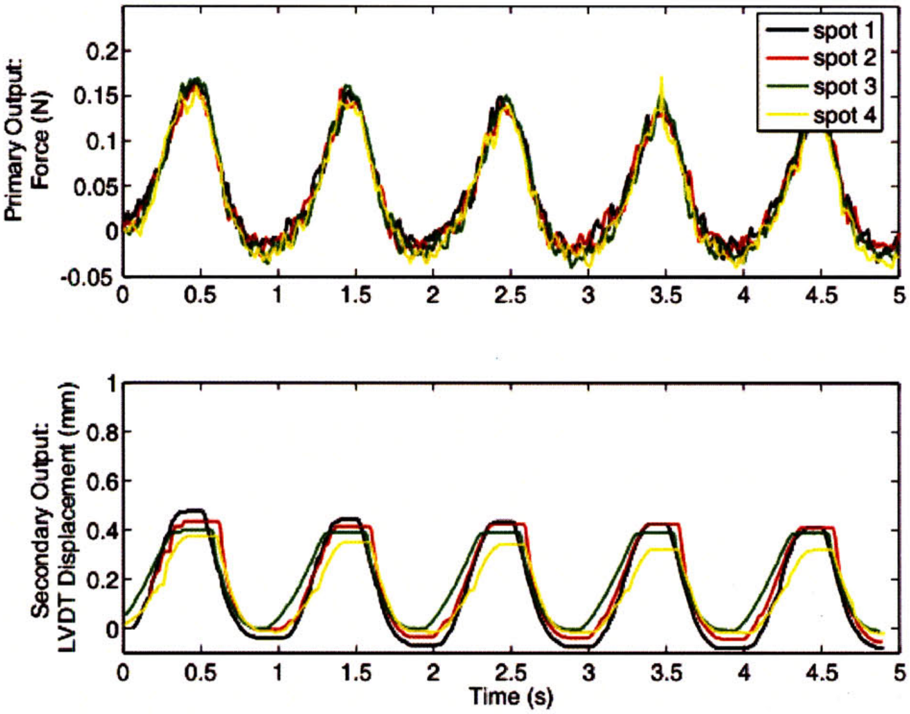

Figure 6-18: The force and secondary sensor response to changing the location of indentation on the same brain specimen

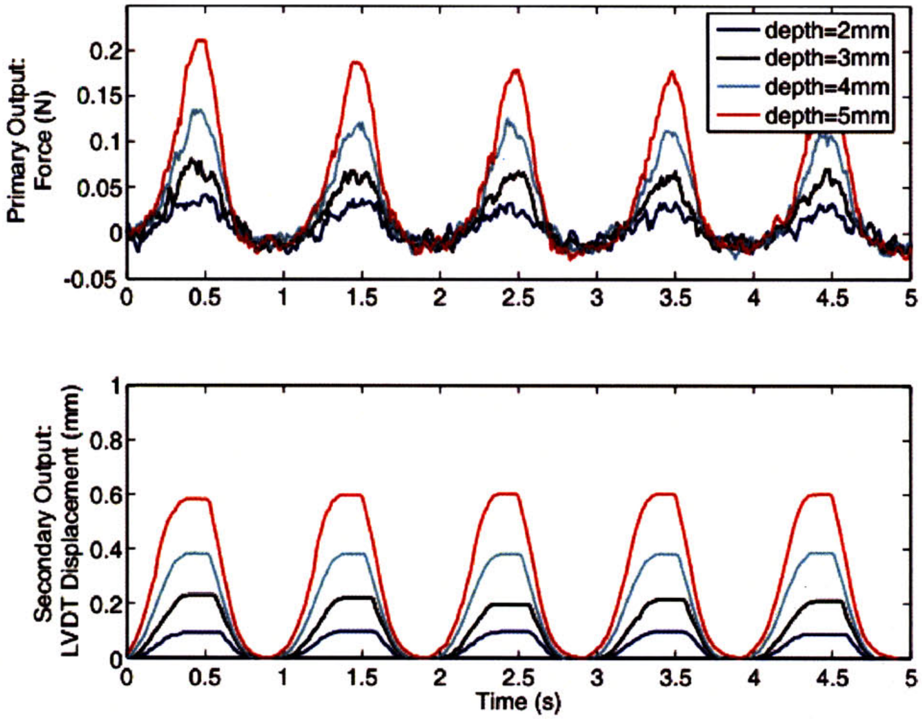

Figure 6-19: Effect of increasing depth on indenter force and secondary sensor results

in indentation. The properties for the material when tested in indentation are obtained by solving the inverse problem of fitting experimental force-displacement data to simulations of the indentation experiment. To prove that the secondary sensor displacements provide accurate volumetric information, simulations of the indentation with secondary sensor experiment must be performed and the response of the secondary sensor from the simulation must be compared to the experimental response.

Chapter 7

Brain Tissue Material Model

A robust constitutive model able to capture the material response over several decades of strain rates is a critical requisite of the project. The analytical model selected in this preliminary stage will be numerically implemented in a finite element framework for full-scale simulations of fluid-structure interaction at the macroscopic scale, as well as for multiscale simulations investigating the mechanical environment of CNS cells during blast loading.

7.1 Literature review of existing FE models

Mechanical models of brain tissue behavior have been proposed for applications of head injury assessment and neurosurgical navigation. Due to the number of brain experiments performed under different modes of deformation in various strain and frequency regimes, there are a wide range of models in the literature. Assuming infinitesimal strain behavior, the viscoelastic response of a material can be captured using basic models (Maxwell, Kelvin, Standard linear solid). However, these basic models are incapable of representing the viscoelastic behavior of such a complex material as brain tissue across a wide range of timescales and strains. Several researchers have proposed using a multi-mode Maxwell model in the form of a prony series (see Equation 7.1).

$$G_R(t) = G_0 \sum_{k=1}^{n} g_k \cdot e^{\frac{-t}{\tau_k}} \tag{7.1}$$

Mendis *et al.* was the first to apply a hyperelastic energy based approach of the Mooney-Rivlin to model the constitutive behavior of brain tissue under compression, yielding a reasonable approximation of the response [45]. Prange *et al.* showed that this same formulation was not successful in modeling the response of white and mixed gray/white matter samples to shear deformation [66]. Instead, a fifth order linear Maxwell model was fit to small strain oscillatory shear data. They modified this model with a first order generalized Ogden model to simulate experiments conducted in large deformation compression [66]. Many use a quasilinear viscoelastic (QLV) model to fit experimental test results [15][45][50][66]. Miller *et al.* employ a form of the Mooney-Rivlin model to demonstrate hyperelastic nonlinear behavior and couples this model with a prony series viscoelastic response. Uniaxial unconfined compression and tension data are fit to such a model, however only load data is recorded and the unloading effects are not discussed [51][50]. Bilston *et al.* proposed a differential one-dimensional model that couples modifying a multi-mode Maxwell, where relaxation are strain dependant and viscosities are strain rate dependent, with a modified Mooney-Rivelin hyperelastic response. This model was validated using large strain oscillatory shear experiments [6]. Based on this work, Shen *et al.* used time-temperature superposition of rheological tests to find the linear viscoelastic response of brain tissue for frequencies up to 10^4 rad/s and modified Bilston's model to predict such behavior [69]. Meaney *et al.* presented a microstructurally based model that considered the transversely isotropic response of axons in the white matter and compared this model to traditional hyperelastic formulations such as Mooney-Rivlin and the Ogden model [44]. He found that none of the hyperelastic approaches matched the tangential stiffness characteristics as well as his microstructurally based model. These are several of the approaches to modeling the behavior of brain tissue. Many of these models are then applied to the FE head impact models to determine head injury criterion and threshold for traumatic brain injury.

7.2 Three-dimensional constitutive model

7.2.1 Pre-conditioned response (primary model)

Based on the uniaxial unconfined compression response, a form of the three-dimensional model was chosen. At a minimum, a nonlinear instantaneous elastic term to capture the nonlinear

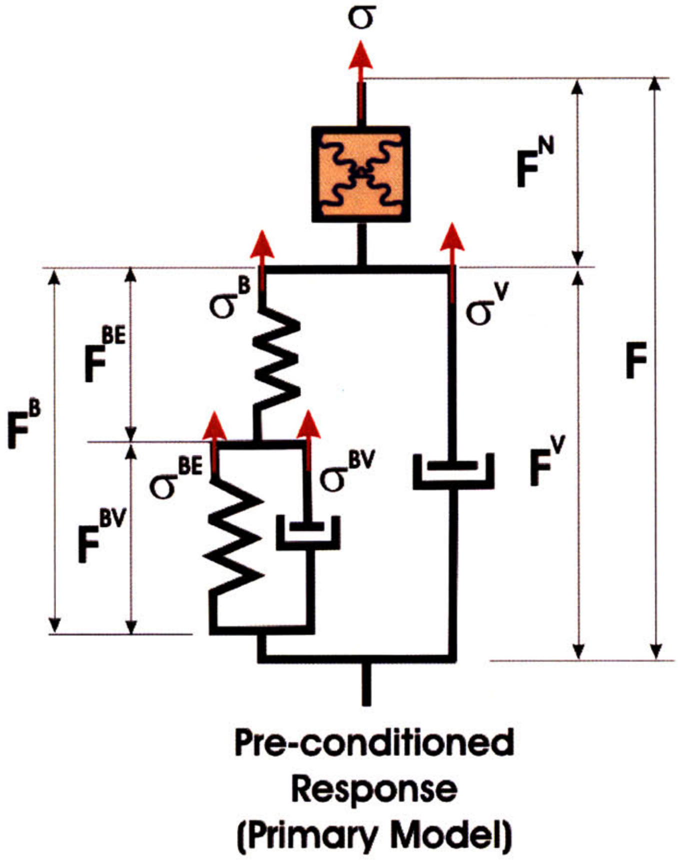

Figure 7-1: Proposed rheological model to describe the behavior of brain tissue

behavior, and a viscous term in parallel with a backstress terms is needed to capture the recoverable time dependent response. We also want to capture the fact that while the peak stresses scale with strain rate, they do not scale linearly. Therefore, the viscous contribution must also be nonlinear. Strain is recovered in load-unload cycles at higher rates, and there is still substantial hysteresis at lower strain rates. This implies that the backstress needed to fully recover the viscous contribution is rate dependent. A rate-dependent backstress also helps to capture the dramatic stress decay and very low equilibrium stress response seen in the stress relaxation experiments. These factors are the basis for the rheological model presented in Figure 7-1. The model is cast within a large-strain kinematics framework. The deformation gradient, F ,is decomposed between the elastic deformation of the nonlinear network, F^N, and an isochoric viscous contribution, F^V, as seen in Equation 7.2. Equation 7.3 describes

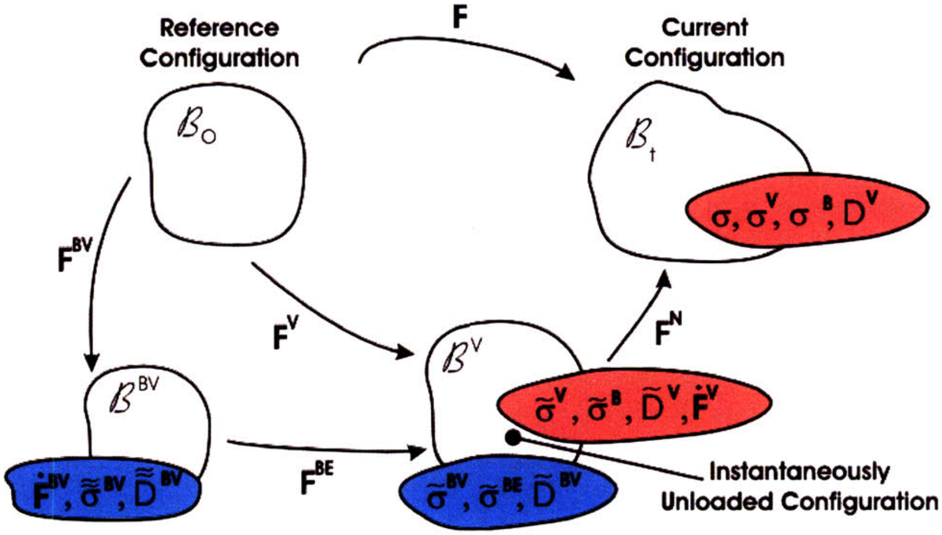

Figure 7-2: Large strain kinematics for rheological model

the viscous contribution, F^V, which can be further decomposed between the instantaneous backstress deformation, F^{BE}, and the long-term backstress deformation, F^{BV}.

$$F = F^N F^V \tag{7.2}$$

$$F^V = F^B = F^{BE} F^{BV} \tag{7.3}$$

The Cauchy stress in the current configuration is obtained from the deformation of the non-linear hyperelastic network, F^N. The formulation of the hyperelastic network is adopted from polymer theory where a statistical model is used to represent the entropic state of the individual fibers in the network. The response is based on two distinct effects occurring in the network: individual fibers stretching and fibers rotating to align themselves in the direction of the applied load. This class of hyperelastic material models rely on two fundamental steps. First, a force-stretch relationship must be defined for the individual chains of the network; second, a simple representative unit structure must be defined to account for the geometry of the network, in order to enable the link between macroscopic deformation variables and the deformation of the individual chains. Although this approach is derived for rubber elasticity, it has been successfully adopted to represent the nonlinear response of biological networks [7]. Note that in this proposed form, an additional hydrostatic contribution has been included to complement the inherent volumetric network resistance.

$$\sigma = \frac{\mu_o \lambda_L}{J^N \lambda^N} \beta B^N - \mu_o \lambda_L \beta_o \underline{1} + K \ln(J^N) \underline{1} \tag{7.4}$$

Equation 7.4 describes this nonlinear behavior where σ is the Cauchy network stress, μ_o is the initial shear modulus, λ_L is the locking stretch of the fibers, J^N is the determinant of the network's deformation gradient F^N given by Equation 7.5, B^N is the left Cauchy-Green tensor defined in Equation 7.6, λ^N is the current stretch of the network, given by Equation 7.7, K is bulk modulus corresponding to the additional volumetric resistance and β is the inverse Langevin function of the current stretch to locking stretch ratio as defined by [38] and given in Equations 7.8 and 7.9.

$$J^N = \det(F^N) = \det(F) = J \tag{7.5}$$

$$B^N = F^N F^{N^T} \tag{7.6}$$

$$\lambda^N = \sqrt{\frac{tr\,(B^N)}{3}} \tag{7.7}$$

$$\beta = \mathcal{L}^{-1} \left(\frac{\lambda^N}{\lambda_L} \right) \tag{7.8}$$

$$\frac{\lambda^N}{\lambda_L} = \cot \beta - \frac{1}{\beta} \tag{7.9}$$

A simple representative unit cube structure defines the geometry of the 8-chain network such that the response of a single chain can be linked to the overall deformation of the network (see Figure 7-3).

The unit cell deforms with the principal stretches thereby allowing the stretch of each fiber to be shared amongst the others. The material parameters which describe the behavior of this

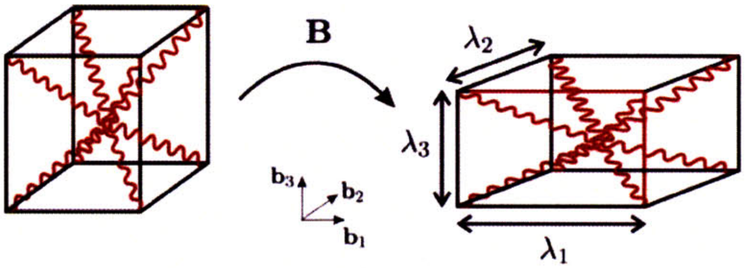

$$\mathbf{B} = \mathbf{F}\mathbf{F}^{\mathbf{T}} = \lambda_1^2\mathbf{b}_1 \otimes \mathbf{b}_1 + \lambda_2^2\mathbf{b}_2 \otimes \mathbf{b}_2 + \lambda_3^2\mathbf{b}_3 \otimes \mathbf{b}_3$$

Figure 7-3: The 8-chain fiber network unit cell and principal stretches under deformation

component of the model are μ_o, λ_L, and K. The deviatoric component of the Cauchy stress, ■′, (Equation 7.10) is balanced by the elastic backstress, σ^B and the viscous back stress, σ^V as shown in Equation 7.11. The backstress, σ^B, represents the push forward of the backstress to the current configuration and is defined in Equation 7.12.

$$\sigma' = \sigma - \frac{1}{3} tr\left(\sigma\right) \underline{1} \tag{7.10}$$

$$\sigma' = \sigma^V - \sigma^B \tag{7.11}$$

$$\sigma^B = \frac{1}{J^N} F^N \tilde{\sigma} F^{N^T} \tag{7.12}$$

The deviatoric driving stress for the viscous deformation σ^V is obtained from Equation 7.13.

$$\sigma^V = \sigma' - \sigma^B \tag{7.13}$$

The direction of the stress deviator is defined by Equation 7.14.

$$N^V = \frac{\sigma^V}{\mid \sigma^V \mid} \tag{7.14}$$

$$D^V = \dot{\gamma}^V N^V \tag{7.15}$$

The viscous stretching tensor, D^V, is constitutively prescribed to be parallel to the deviatoric viscous stress, σ^V, through 7.15 where $\dot{\gamma}^V$ is the shear strain rate of the viscous component that is driven through a power law relationship on the magnitude of the driving stress σ^V and on the material parameters σ_o and n as given in Equation 7.16.

$$\dot{\gamma}^V = f\,\dot{\gamma}^o \left(\frac{|\sigma^V|}{\sigma_o}\right)^n \tag{7.16}$$

where $\dot{\gamma}^o$ is a dimensional factor set to 1 s^{-1}. In this relation, we include a reptation factor, f, (7.17) to reflect the increased resistance to viscous deformation with accumulated viscous strain [5].

$$f = \left(\frac{\alpha}{\alpha + \varepsilon^V}\right)^2 \tag{7.17}$$

Where ε^V is a measure of accumulated viscous flow and α is a small number correcting the asymptotic behavior of f for $\varepsilon^V = 0$. ε^V is obtained in terms of the viscous stretch, λ^V, as defined by Equations 7.18 through 7.20.

$$\varepsilon^V = \lambda^V - 1 \tag{7.18}$$

$$\lambda^V = \sqrt{\frac{tr\left(B^V\right)}{3}} \tag{7.19}$$

$$B^V = F^V F^{V^T} \tag{7.20}$$

The rate of change of the viscous component of deformation $\dot{F}^V$ as expressed in Equation 7.21.

$$\dot{F}^V = \tilde{L}^V F^V \tag{7.21}$$

where $\tilde{L}^V$ is the viscous velocity gradient in the instantaneously unloaded configuration and can be expressed as the sum of the stretching tensor $\tilde{D}^V$ and the spin tensor $\tilde{W}^V$ as seen in Equation 7.22.

$$\tilde{L}^V = \tilde{D}^V + \tilde{W}^V \tag{7.22}$$

The stretching tensor in the instantaneously unloaded configuration is obtained by the pushback of the viscous stretching tensor,D^V,via Equation 7.23.

$$\tilde{D}^V = F^{N^{-1}} D^V F^N \tag{7.23}$$

The arbitrary rotation associated with the definition of the unloaded configuration is eliminated by setting $\tilde{W}^V = 0$. Note that D^V is deviatoric, and F^V remains isochoric throughout the deformation. The deviatoric backstress, $\tilde{\sigma}^B$, is defined in the instantaneously unloaded configuration in terms of the Henky strain corresponding to the F^{BE} deformation gradient given in Equations 7.24-7.26 where G_o is a material parameter.

$$\tilde{\sigma}^B = 2G_o \left[E^{BE} - \frac{tr\left(E^{BE}\right)}{3} \underline{1} \right] \tag{7.24}$$

$$E^{BE} = \ln \left(B^{BE}\right)^{\frac{1}{2}} \tag{7.25}$$

$$B^{BE} = F^{BE} F^{BE^T} \tag{7.26}$$

The viscous stretching in the backstress network $\tilde{D}^{BV}$ is defined in the instantaneously unloaded configuration. The effective stress driving, $\tilde{D}^{BV}$, is obtained as

$$\tilde{\sigma}^{BV} = \tilde{\sigma}^B - \tilde{\sigma}^{BE} \tag{7.27}$$

where $\tilde{\sigma}^{BE}$ is the push forward long term elastic back stress defined in the long-term unloaded configuration as given in Equation 7.28.

$$\tilde{\sigma}^{BE} = \frac{1}{J^{BE}} F^{BE} \tilde{\tilde{\sigma}}^{BE} F^{BE^T} \tag{7.28}$$

The viscous stretching tensor $\tilde{D}^{BV}$ is defined in Equation 7.29-7.31 as

$$\tilde{D}^{BV} = \dot{\gamma}^{BV} N^{BV} \tag{7.29}$$

where

$$N^{BV} = \frac{\tilde{\sigma}^{BV}}{\mid \tilde{\sigma}^{BV} \mid} \tag{7.30}$$

and

$$\dot{\gamma}^{BV} = \frac{\mid \tilde{\sigma}^{BV} \mid}{\eta} \tag{7.31}$$

where η is a material property. Finally, the long term elastic backstress is defined in the long-term unloaded configuration (Equation 7.32-7.34) as

$$\overset{\approx}{\sigma}^{BE} = 2G_{\infty} \left[E^{BV} - \frac{tr\left(E^{BV}\right)}{3} \underline{1} \right] \tag{7.32}$$

where

$$E^{BV} = \ln\left(B^{BV}\right)^{\frac{1}{2}} \tag{7.33}$$

$$B^{BV} = F^{BV} F^{BV^T} \tag{7.34}$$

This concludes the formulation for the conditioned (primary) response of the tissue. The model requires the definition of 9 material parameters: $\mu_o, \lambda_L, K, G_o, G_{\infty}, \eta, \sigma_o, m$,and α.

7.2.2 Conditioning Response

A substantial conditioning effect was observed in the uniaxial compression response presented in the previous chapter. The first load-unload cycle exhibited a much stiffer response than the subsequent loading cycles. Cycles 2 through 5 also continued to drop in their peak stress with every additional loading. To capture the conditioning effect, another network was added in parallel to the pre-conditioned network. The addition of this network simulates the initial conditioning response of the experiments where the stress is much higher in the first cycle of loading than the subsequent cycles.

This additional network is cast within a large-strain kinematics framework as shown in Figure 7-5.

The deformation gradient, F, is decomposed between the elastic deformation of the nonlinear network, F^C,and an isochoric viscous contribution, F^{VC} as shown in equation 7.35.

$$F = F^C F^{VC} \tag{7.35}$$

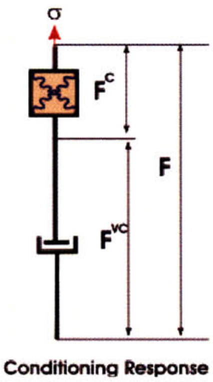

Figure 7-4: Conditioning response network to be added to pre-conditioned network

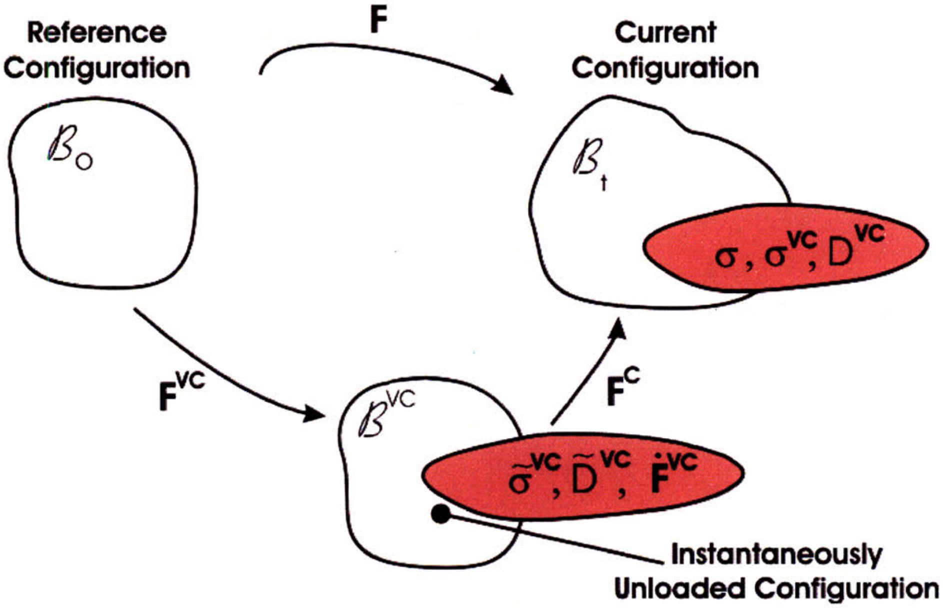

Figure 7-5: Large frame kinematic network for conditioning network

$$\sigma^C = \frac{\mu_{oR}\lambda_R}{J^C\lambda^{NC}}\beta^C B^C - \mu_{oR}\lambda_R\beta_o\underline{1} \tag{7.36}$$

Equation 7.36 describes the behavior similar to the nonlinear hyperelastic network proposed in the previous section, where σ^C is the Cauchy network stress, μ_{oR} is the initial shear modulus, λ_R is the locking stretch of the fibers, J^C is the determinant of the network's deformation gradient F^C given by Equation 7.37, B^C is the left Cauchy-Green tensor defined in Equation 7.38, λ^{NC} is the current stretch of the network, given by Equation 7.39, and β is the inverse Langevin function of the current stretch to locking stretch ratio as defined by [38] and given in Equations 7.40 and 7.41.

$$J^C = \det(F^C) = \det(F) = J \tag{7.37}$$

$$B^C = F^C F^{C^T} \tag{7.38}$$

$$\lambda^{NC} = \sqrt{\frac{tr\left(B^C\right)}{3}} \tag{7.39}$$

$$\beta^C = \mathcal{L}^{-1}\left(\frac{\lambda^{NC}}{\lambda_R}\right) \tag{7.40}$$

$$\frac{\lambda^{NC}}{\lambda_R} = \cot\beta^C - \frac{1}{\beta^C} \tag{7.41}$$

The deviatoric driving stress for the viscous deformation σ^{VC} is equal to the deviator of the Cauchy network stress, σ,as seen by Equation 7.42.

$$\sigma^{VC} = \sigma^C - \frac{1}{3}tr(\sigma^C)\underline{1} \tag{7.42}$$

The direction of the stress deviator is defined by Equation 7.43.

$$N^{VC} = \frac{\sigma^{VC}}{\mid\sigma^{VC}\mid} \tag{7.43}$$

$$D^{VC} = \dot{\gamma}^{VC} N^{VC} \tag{7.44}$$

The viscous stretching tensor, D^{VC}, is constitutively prescribed to be parallel to the deviatoric viscous stress, σ^{VC}, through 7.44 where $\dot{\gamma}^{VC}$ is the shear strain rate of the viscous component that is driven through a power law relationship on the magnitude of the driving stress σ^{VC} and on the material parameters σ_{oR} and m as given in Equation 7.45.

$$\dot{\gamma}^{VC} = f_{vc}\, \dot{\gamma}^{oc} \left(\frac{|\, \sigma^{VC} \,|}{\sigma_{oR}} \right)^{m} \tag{7.45}$$

where $\dot{\gamma}^{oc}$ is a dimensional factor set to 1 s^{-1}. In this relation, we include a reptation factor, f_{vc}, (7.46) to reflect the increased resistance to viscous deformation with respect to the accumulated viscous strain [5]. The reptation factor is like a yield condition. When the viscous strain exceeds the max viscous strain that the material has seen, the reptation factor is activated as defined by Equation 7.46. However, when the viscous strain is within the maximum viscous strain bounds, the reptation factor has no effect, as given by Equation 7.47.

$$\text{for } \varepsilon^{VC} \geq \varepsilon^{VC}_{\text{max,}} \qquad f_{vc} = \left(\frac{\xi}{\xi + \varepsilon^{VC}} \right)^{2} \tag{7.46}$$

$$\text{for } \varepsilon^{VC} \prec \varepsilon^{VC}_{\text{max,}} \qquad f_{vc} = 1 \tag{7.47}$$

Where ε^{VC} is a measure of accumulated viscous flow and ξ is a small number correcting the asymptotic behavior of f_{vc} for $\varepsilon^{VC} = 0$. ε^{VC} is obtained in terms of the viscous stretch, λ^{VC}, as defined by Equations 7.48 through 7.50.

$$\varepsilon^{VC} = \lambda^{VC} - 1 \tag{7.48}$$

$$\lambda^{VC} = \sqrt{\frac{tr\,(B^{VC})}{3}} \tag{7.49}$$

$$B^{VC} = F^{VC} F^{VC^{T}} \tag{7.50}$$

The rate of change of the viscous component of deformation $\dot{F}^{VC}$ is expressed in Equation 7.51.

$$\dot{F}^{VC} = \tilde{L}^{VC} F^{VC} \tag{7.51}$$

where $\tilde{L}^{VC}$ is the viscous velocity gradient in the instantaneously unloaded configuration and can be expressed as the sum of the stretching tensor $\tilde{D}^{VC}$ and the spin tensor $\tilde{W}^{VC}$ as seen in Equation 7.52.

$$\tilde{L}^{VC} = \tilde{D}^{VC} + \tilde{W}^{VC} \tag{7.52}$$

The stretching tensor in the instantaneously unloaded configuration is obtained by the pushback of the viscous stretching tensor, D^{VC}, via Equation 7.53.

$$\tilde{D}^{VC} = F^{C^{-1}} D^{VC} F^{C} \tag{7.53}$$

The arbitrary rotation associated with the definition of the unloaded configuration is eliminated by setting $\tilde{W}^{VC} = 0$. It should be noted that D^{VC} is deviatoric, and F^{C} remains isochoric throughout the deformation.

Combining the two networks, the pre-conditioned response network and the conditioning response network results in a comprehensive three-dimensional nonlinear viscoelastic model that can capture the material's rate dependence, nonlinearity and time dependence. The complete network is given in Figure 7-6.

7.2.3 Model Fit: Uniaxial compression using pre-conditioned network

The model described in the preceding section was implemented in a numerical formulation using commercial finite element software (ABAQUS version 6.5.4, Providence, RI). The constitutive equations describing the three-dimensional behavior of the brain material were implemented through a user defined material (UMAT) subroutine. As a first pass to determining the appropriate constitutive model to describe the material behavior seen in the unconfined compression tests, the pre-conditioned response, or primary response, as described in Section 7.2.1 was first used. The constitutive form of the model with corresponding model parameters is given in Figure 7-7. Values for the parameters are determined by fitting the simulation output to the representative material response (see Figure 6-10-6-15).

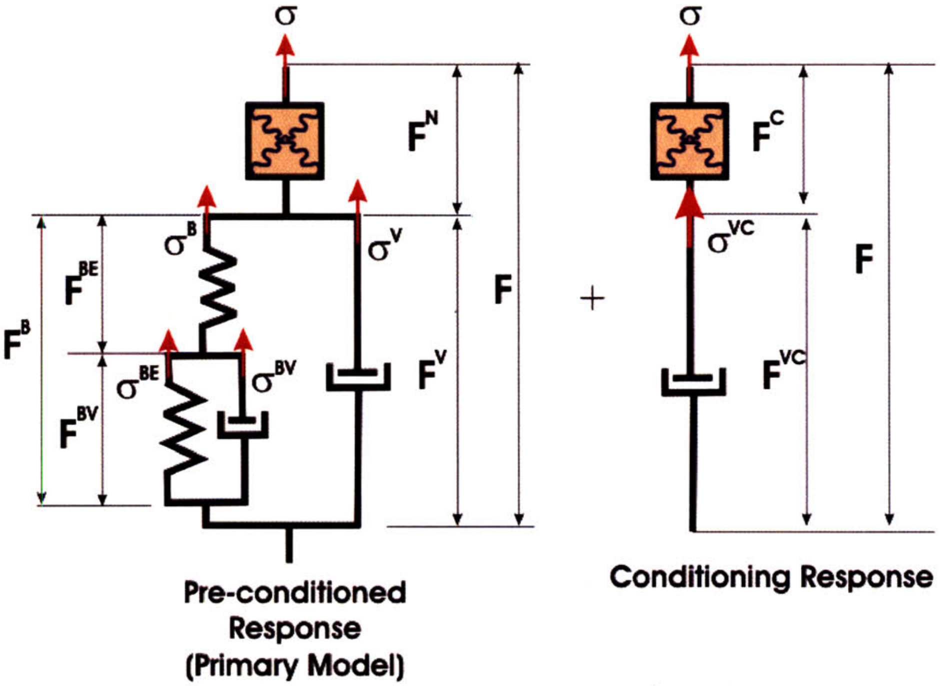

Figure 7-6: Complete three-dimensional model capturing both the pre-conditioned and conditioning responses of the material

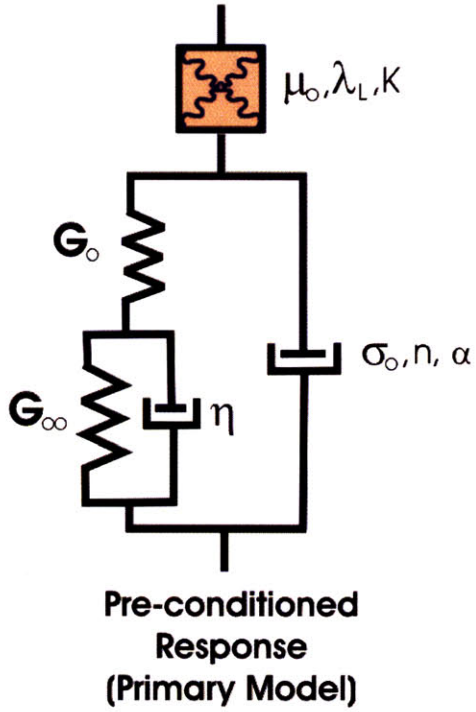

Figure 7-7: Proposed three-dimensional consititutive model with material properties

Figures 7-8 through 7-10 show the fit of the model simulations to the constant rate load-unload representative compression test response. The stress relaxation model fit and experimental response are given in Figure 7-11, while the fit and experimental bulk response from the lateral stretch measurement is given in Figure 7-12. Using each of these five experimental responses, the parameters that provided the best fit to the corresponding responses were selected. The initial shear modulus, μ_o, is adjusted to fit the initial loading ramp of the curve. To obtain the appropriate level of peak stress, the locking stretch, λ_L, and the additional bulk term, K, are adjusted. Because there is time dependence in the material, a viscous term is added in series with the nonlinear spring, however since the stress is recoverable, a backstress term is added in parallel with the viscous term. As the peak stresses at each rate do not vary linearly, a nonlinear dashpot and a decaying backstress, in the form of a standard linear solid are assigned. The nonlinear dashpot with a normalizing shear stress, σ_o, and an exponent, n, are the parameters that can be varied as seen in Equation 7.16. These two parameters are selected to match the model fit to the hysteresis loops. In addition, a reptation factor, f, that is described by the parameter, α, is also utilized to reflect the increased resistance to viscous deformation with increased accumulated viscous strain. A table of the parameter values that capture the best overall fit for all five experimental responses is given in Table 7.1.

For this set of parameters and with this constitutive model, the peak levels of stress are obtained at each loading rate, however the conditioning response of the material at the very first loading ramp is not captured. The predicted short and long term relaxation responses are in good agreement with the experimental results as seen in Figure 7-11. Finally, the lateral expansion of the material is predicted and fits well with the experimental lateral strain history as shown in Figure 7-12.

The effect of changing the bulk modulus, K, in the simulation is investigated. In the model simulations, several bulk moduli are selected and the resulting stress history and lateral strain history are observed as shown in Figure 7-13. Observations can be made more clearly when looking at a single load-unload cycle, as shown in Figure 7-14. The bulk moduli are varied between 100 and 10000Pa and the optimal bulk modulus that fit both the stress and the lateral strain responses was a bulk modulus of 3000Pa. At K=100Pa, the lateral strain response is negative indicating that the material response is highly compressible. On the other end of the

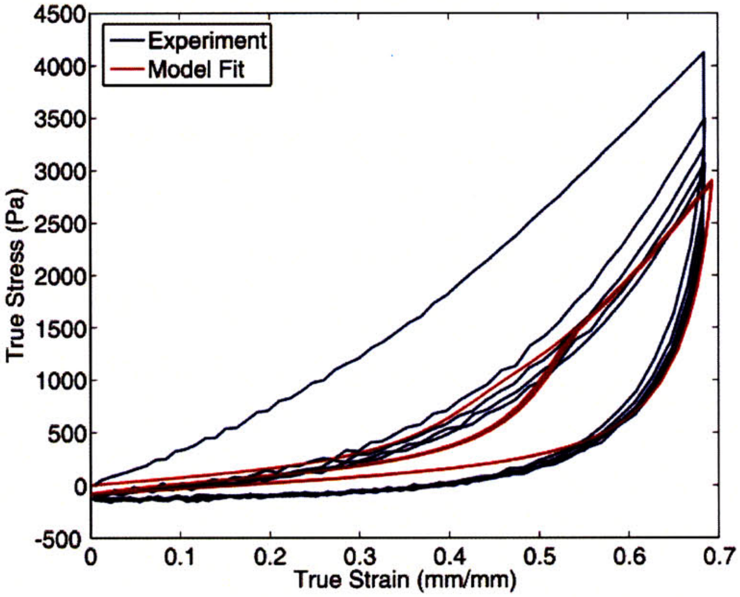

Figure 7-8: Experimental data with model fit for uniaxial compression response of brain tissue at a 100%/s loading rate

Material parameters		
1	μ_o	20Pa
2	λ_L	1.1
3	K	3000Pa
4	G_o	2000Pa
5	G_∞	500Pa
6	η	200000Pa-s
7	σ_o	20Pa
8	n	3
9	α	0.005

Table 7.1: Values for the material parameters of the proposed three-dimensional model

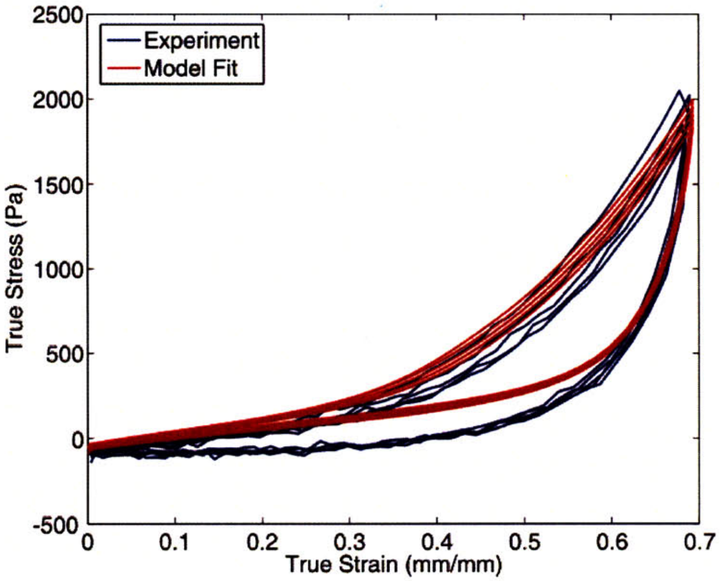

Figure 7-9: Experimental data with model fit for uniaxial compression response of brain tissue at a 10%/s loading rate

spectrum, at K=10000Pa the simulation peak stress corresponds well to the experimental peak stress, however the lateral strain prediction appears to overshoot the experimental data. For this reason, a bulk modulus of 3000Pa was selected.

Overall, the pre-conditioned model fit to the experimental response is one that is suitable at the three different rates, however, the initial loading ramp, or the conditioning ramp, is not captured. To capture this initial loading ramp, the additional network presented in Section 7.2.2 is included in the simulation.

7.2.4 Model Fit: Uniaxial compression response with both pre-conditioned and conditioning networks

The conditioning response seen by the initial loading ramp is captured in the model through the additional network shown in Figure 7-4. This network describes this loading response through incorporating a nonlinear spring and a nonlinear viscous term in series. The parameters for the nonlinear spring are the initial shear modulus, μ_{oR}, and the initial locking stretch, λ_R, as given

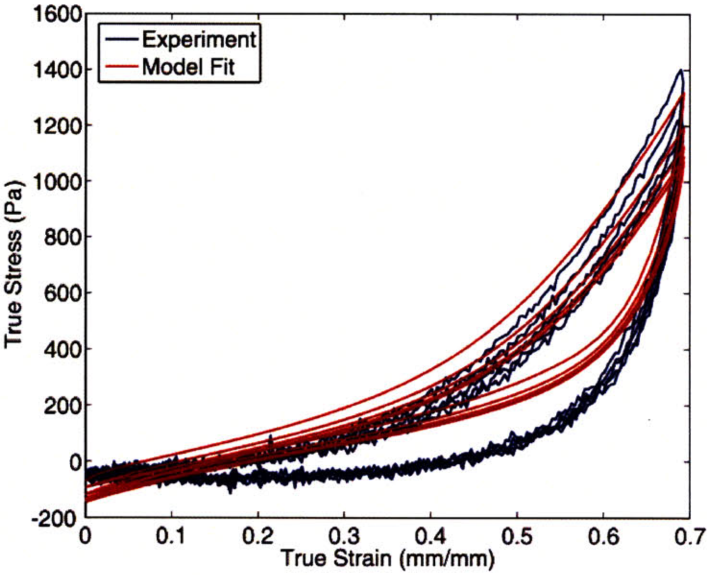

Figure 7-10: Experimental data with model fit for uniaxial compression response of brain tissue at a 1%/s loading rate

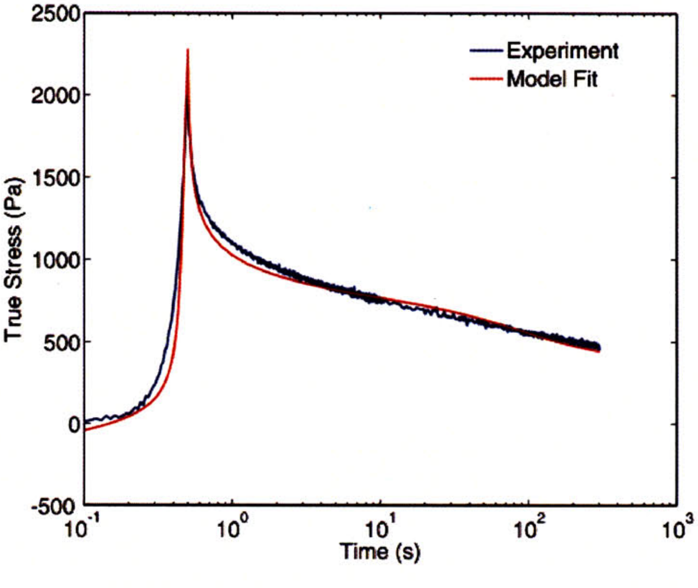

Figure 7-11: Experimental data with model fit for uniaxial compression stress relaxation response of brain tissue

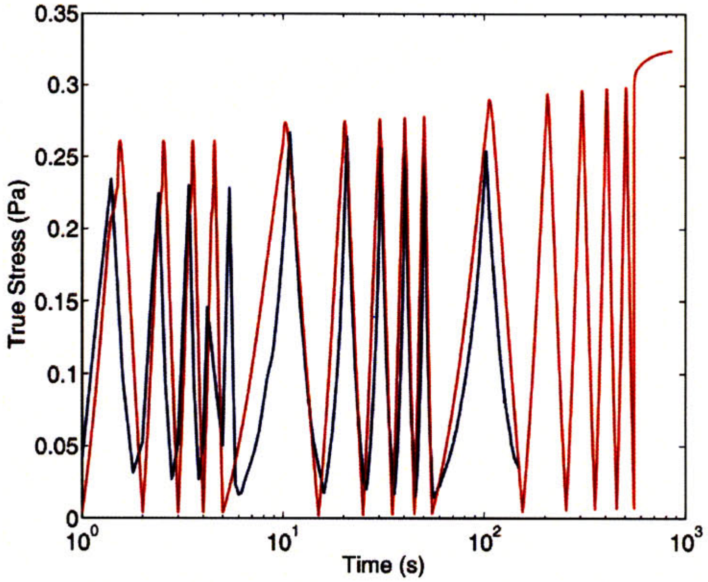

Figure 7-12: Experimental data with model fit for the lateral strain response of brain tissue compression testing

μ_{oR}	14 Pa
λ_R	1.05
σ_{oR}	28 Pa
ξ	0.007
m	3

Table 7.2: Specifications of dynamic indentation surface tracking (DIST) tool design

in Equation 7.36. Similar to the pre-conditioned network, the viscous term is implemented using the normalizing shear modulus parameter, σ_{oR} and an exponent parameter, m. A reptation factor, f_{vc} is also added to the viscous term in the form given in Equations 7.46-7.47, and is defined by the parameter, ξ. The reptation factor acts like a yield condition. When the viscous strain is within the maximum viscous strain bounds, the factor has no effect on the response. However, when the viscous strain exceeds the maximum viscous strain experienced by the material, the reptation factor is activated.

The parameters that best fit to the initial conditioning ramp of the experiment are given in Table 7.2. The contribution of this network to the load-unload model fit and the stress relaxation

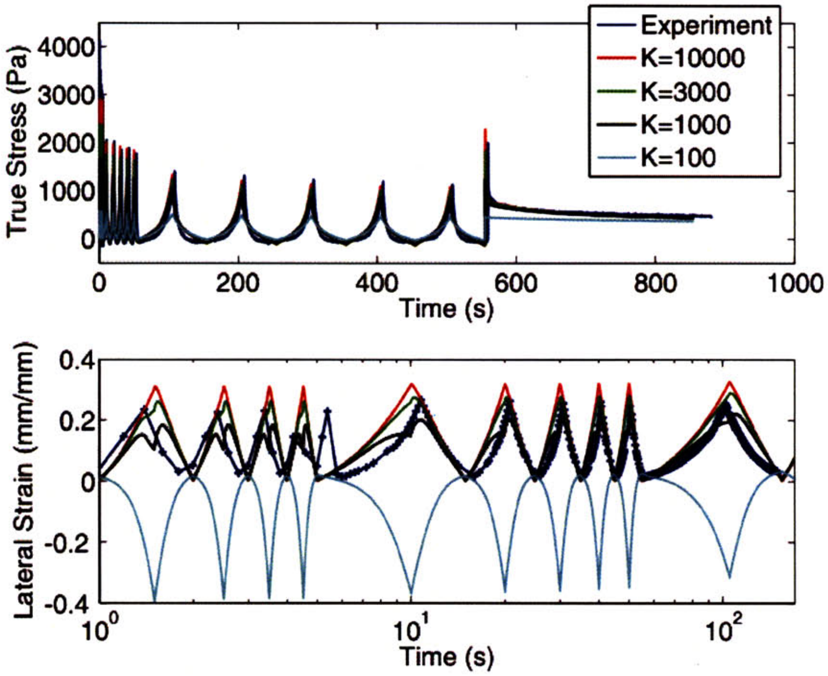

Figure 7-13: The effect of varying the bulk modulus on the stress history and lateral strain history of the simulation

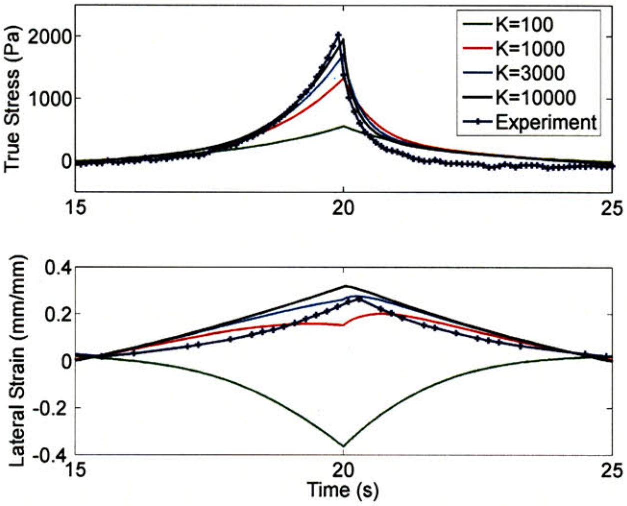

Figure 7-14: A single load-unload cycle indicating the effect of changing the bulk modulus on the true stress history and lateral strain history of the similation results

fit are given in Figure 7-15 and 7-16, respectively. The load-unload fit of the simulation to the model when considering both networks in parallel, as shown in Figure 7-6, is given in Figure 7-17. The complete fifteen parameter model fit to the stress relaxation response and lateral strain history are given in Figures 7-18 and 7-19, respectively.

The addition of the conditioning network appears to capture the initial conditioning ramp as well as a slight decreasing peak stress with every subsequent loading. By employing a model that considers the new network in parallel with the original pre-conditioned network, the major aspects of this complex material response, the strain rate dependence, the stiffening of the stress at large strains, the hysteresis and the nonlinear relaxation are captured. The complete model uses fifteen material parameters. Depending on the application of the model, capturing this initial loading behavior may or may not be of critical relevance. In the case where modeling the pre-conditioned tissue response is more relevant, it is more effective to consider only the pre-conditioned model thereby eliminating six additional parameters into the model fit.

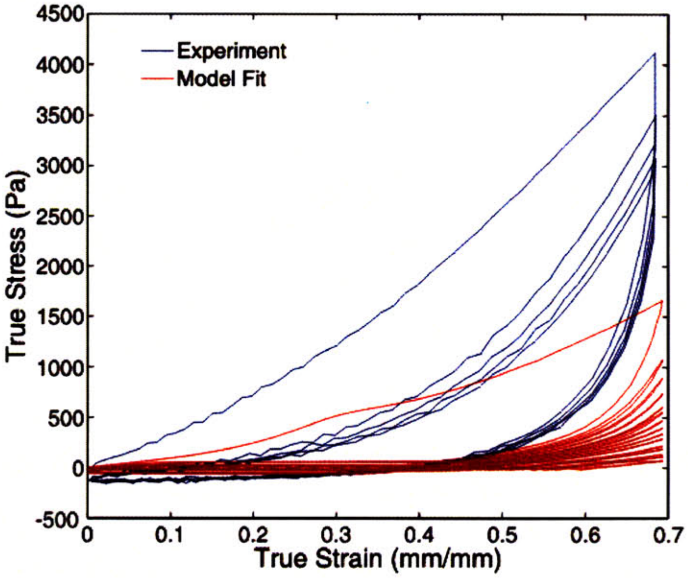

Figure 7-15: Model fit to experiments using the conditioning network model

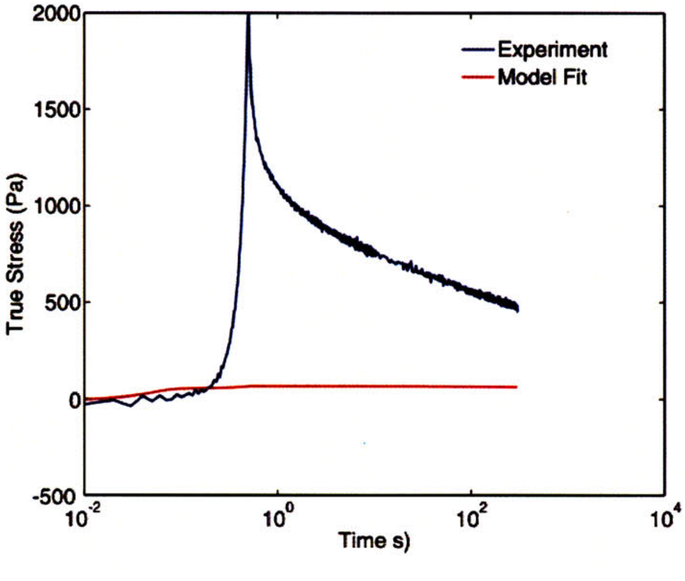

Figure 7-16: The contribution of the additional network to the stress relaxation response

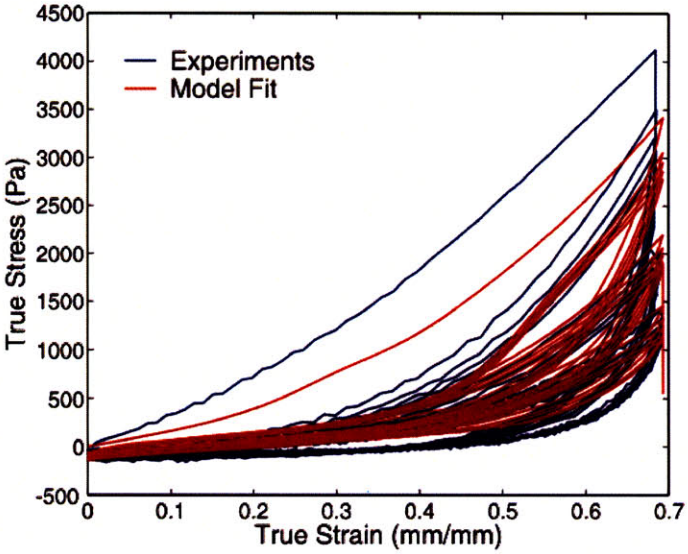

Figure 7-17: The model fit to the experimental load-unload response using both the preconditioned and conditioning networks in parallel

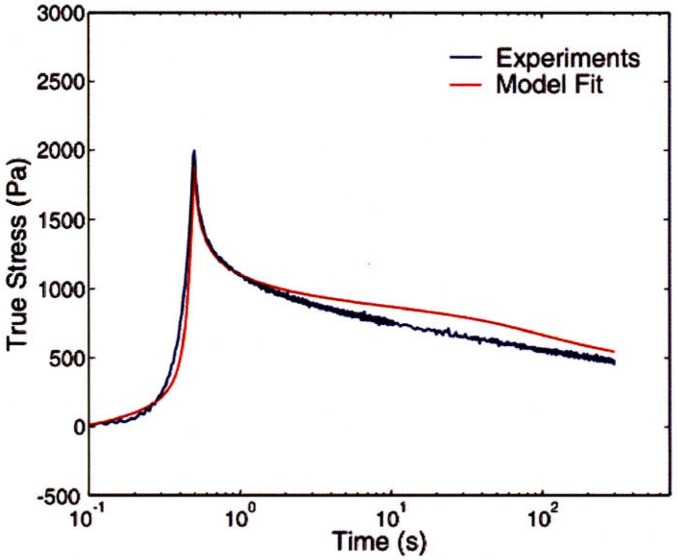

Figure 7-18: The model fit of the experimental stress relaxation response to both the preconditioned and conditioning networks in parallel

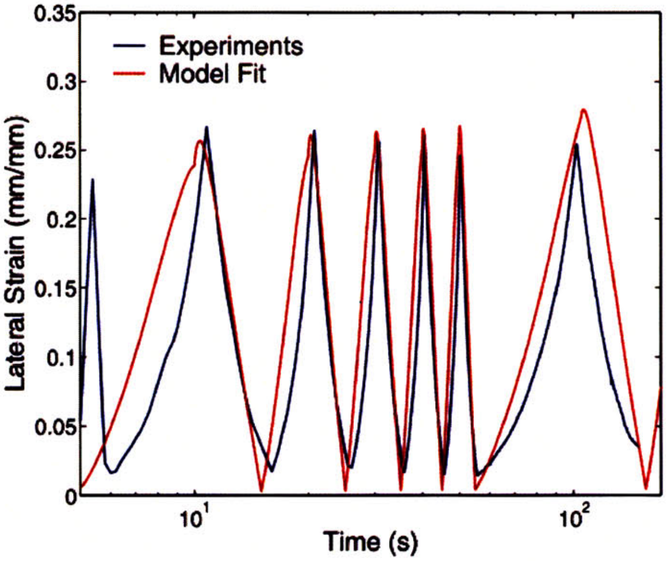

Figure 7-19: The model fit to the experimental lateral strain history using both the pre-conditioned and conditioning networks in parallel

7.2.5 Model Fit: Indentation with secondary sensor experiments

The lateral strain response, a critical measure of a material's compressibility, can be captured when testing specimens in uniaxial compression or tension using the video extensometer setup. When performing in vivo or in situ indentation experiments, a similar experimental apparatus that captures the volumetric response for a given material does not exist. Adding the secondary sensor to a traditional indentation experiment aims to measure the bulk response of a material when tested in the in vivo or in situ configuration. In section 6.2.3, the results of the in vitro indentation experiment with the secondary sensor is presented. Figure 6-18 shows the experimental response of the indenter force and secondary sensor displacement to an indentation displacement protocol.

To assess the effectiveness of adding the secondary sensor to track surface deformations, a three-dimensional FE simulation of the experiment as presented in Figure 7-20 is conducted. The material model for the pre-conditioned response, with nine parameters, presented in section 7.2.3, is applied to the simulated brain tissue underneath the indenter. The dimensions for the

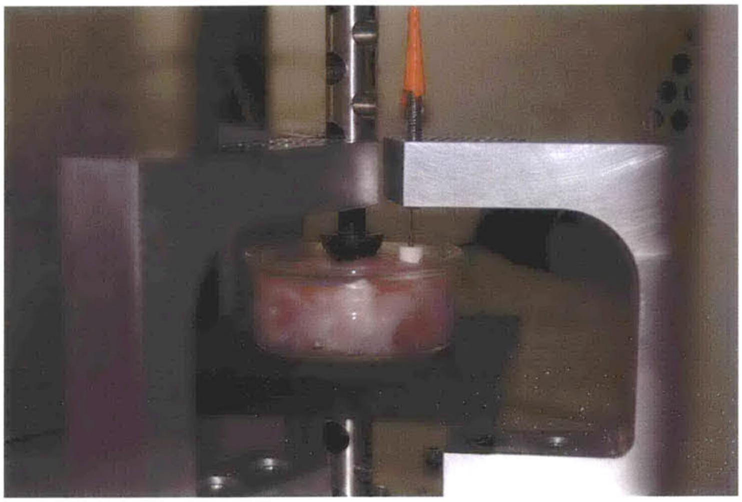

Figure 7-20: Experimental setup of brain indentation test with secondary sensor

tissue, indenter and secondary sensor and their relative locations and boundary conditions are consistent with the experimental setup. Details of the simulation can be found in Figure 7-21. The tissue lies on a flat rigid substrate. The radial motion at the outer diameter of the tissue is constrained, but the tissue is allowed to slide radially along the bottom surface and vertically along the side walls. The geometry of the simulation is dimensionally consistent with the experiment. In the experimental setup, a few axisymmetric experiments were performed, but the majority of experiments were conducted with the indenter slightly offset from the center of the tissue. This is because the distance between the indenter and the optimal location for the secondary sensor was greater than the radius of the specimen, such that if the indenter was placed in an axisymmetric configuration, the secondary sensor would interfere with the side of the specimen dish. The spherical indenter tip and the secondary cylindrical tip are modeled as analytical rigid surfaces. Contact between the indenters and the tissue surface is modeled as frictionless, with an exponential normal compliance. The tissue FE mesh consists of 5520 linear, hexahedral elements (C3D8). The LVDT spring of the secondary sensor is modeled by a single truss element (T3D2) so that the spring stiffness is defined by the area and length of the truss, and by a linear elastic modulus. For all simulations we selected values for these parameters to provide an LVDT stiffness k_{LVDT}=0.01N/m.

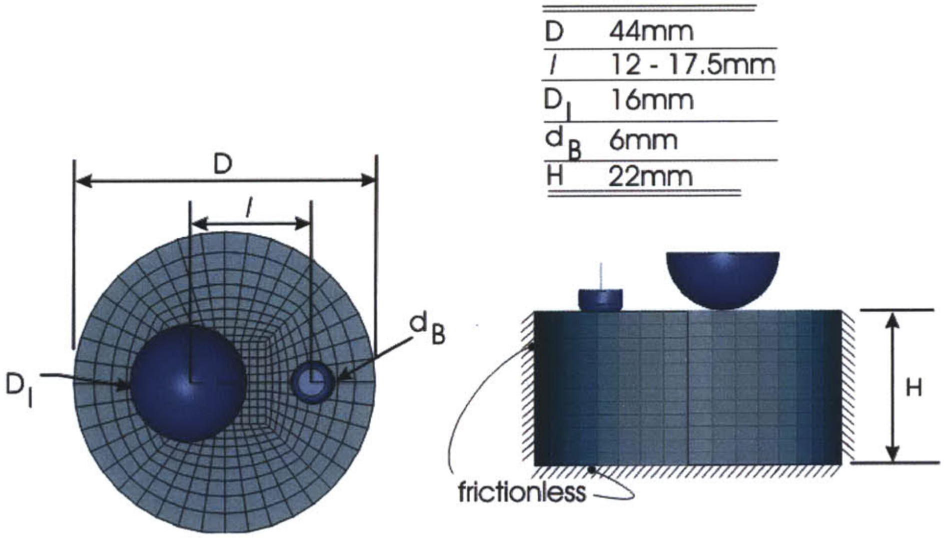

D	44mm
l	12 - 17.5mm
D_I	16mm
d_B	6mm
H	22mm

Figure 7-21: FE simulation of indentation experiment with secondary sensor

The simulation displacement input steps are consistent with the experiment described in Section 6.2.3. In the first step of the simulation, the indenter and the secondary sensor are brought into contact with the material. In the following step, the indenter is given a sinusoidal displacement with an amplitude of 5mm into the tissue, while the secondary sensor remains in contact with the tissue surface. The resulting indenter force and secondary sensor displacement are recorded and their values are compared to the experimental results in Figure 7-22. The results show that the force sensor model prediction is in good agreement with the experiments, while the secondary sensor response is about 20% lower than the predicted response. This discrepancy can be attributed to several issues. There exists nominal friction in the sensor which would likely cause the effect of the tops of the peaks being cut off. This is because at the very top of the sensors motion, there is likely not enough force generated by the tissue on the sensor to overcome the frictional effects. Also, the fact that the tissue is treated as a cylinder, when in fact, the shape of the brain hemisphere is much more complex. The simulation assumes a flat surface of the tissue so that the initial location of the indenter and secondary sensor are in the same plane. In reality, the secondary sensor sits slightly lower than the starting position of the indenter.The contour plot for this simulation is given in Figure 7-23, and shows that while the indenter has a negative imposed displacement in the 2- direction, the

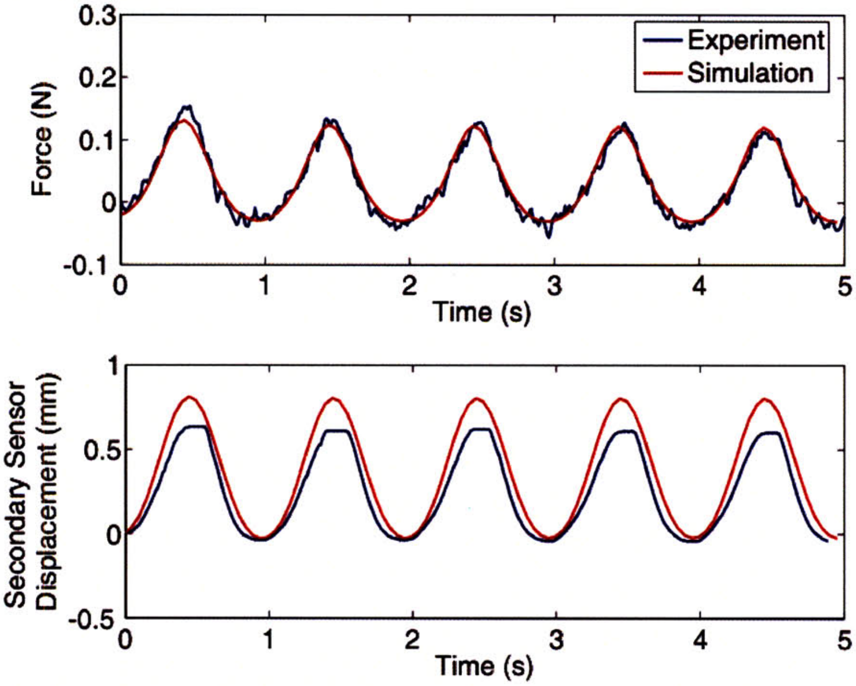

Figure 7-22: The model-predicted indenter force and secondary displacement response to the experimental results

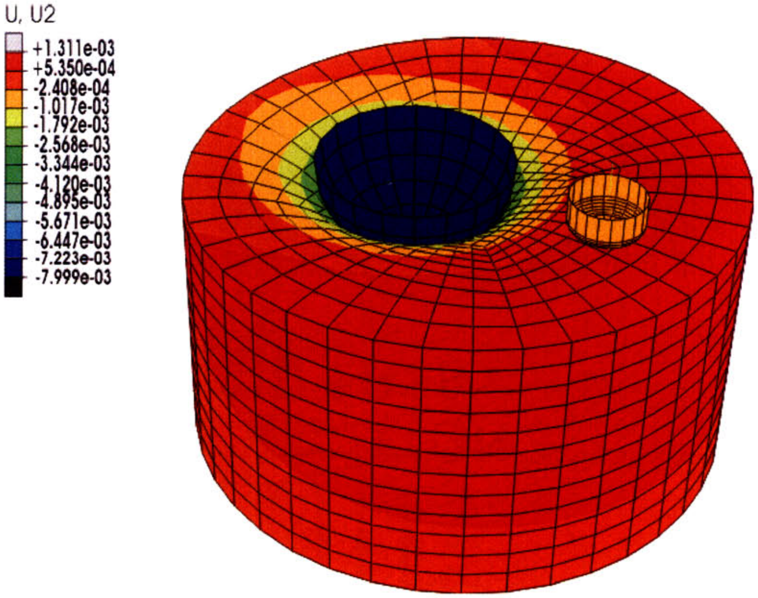

Figure 7-23: Contour plot of the displacement of the indenter and secondary in the loading direction

surrounding tissue, as shown in red, displaces in the positive 2- direction. Because the spring constant on the simulated secondary sensor is very low, the secondary sensor moves with the surface of the tissue. Similar to the bulk modulus sensitivity study conducted for the uniaxial compression simulations, a series of simulations to assess the effect of the bulk modulus on the predicted secondary sensor displacement are conducted. Figure 7-24 describes the results of this study. As in the uniaxial compression case shown in the previous section, the bulk modulus is varied between K=100Pa and K=10000Pa and the resulting indenter force and secondary sensor displacements are observed. For K>3000Pa, the secondary sensor displacement is in the positive direction, indicating that the tissue travels vertically exhibiting a more incompressible behavior. For the cases where K=100Pa and K=1000Pa, the secondary sensor seemed to extend or travel vertically downward, indicating a more compressible material behavior. This trend is consistent with that shown in Figure 7-13 for the case of the lateral stretches in uniaxial compression.

When superimposing the results of changing the bulk modulus on the three-dimensional indentation with secondary sensor simulation to the experimental results, as shown in Figure

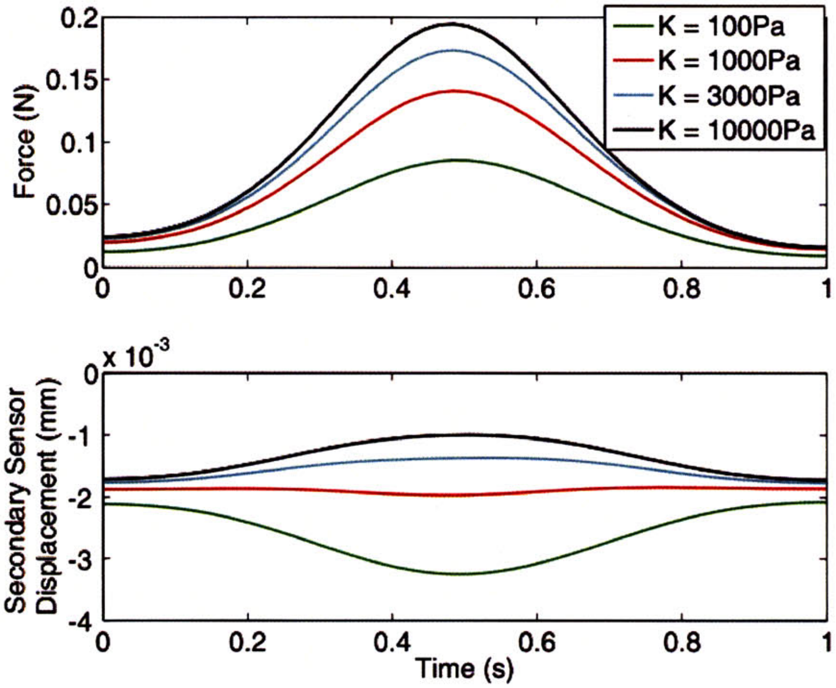

Figure 7-24: The effect of varying the bulk modulus on the indenter force and secondary sensor displacement

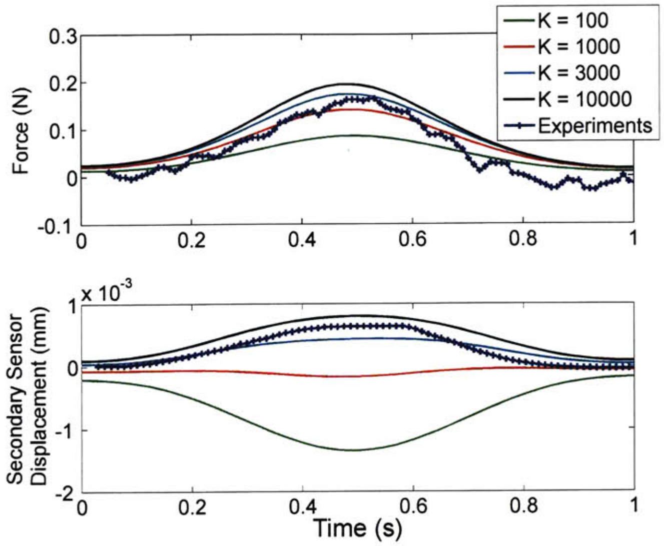

Figure 7-25: The effect of changing the bulk modulus on the resulting force and secondary sensor displacement in the simulation compared with the experimental response

7-25, it is clear that a bulk modulus of approximately K=3000Pa provides the best choice. The optimal parameter value for K, the bulk modulus, in the uniaxial compression experiments is also K=3000Pa, as seen in Figure 7-14. This result is a major step in the validation of the indentation experimental setup with the secondary sensor as a measure of the volumetric material response. The parameter values for the pre-conditioned model were found by fitting the uniaxial compression experiments to the pre-conditioned model simulation. This same material model with the determined parameter values were assigned to the indentation simulation. Therefore, the results seen in 7-22 validates that the pre-conditioned model that is assigned to the material in the simulations has parameter values that are consistent in predicting the indentation response. The results shown in Figure 7-25 further strengthen this assertion as the predicted value of the bulk modulus, K, is K=3000Pa.

7.2.6 A secondary sensor placement sensitivity study

A sensitivity study was conducted to understand the effect of placement accuracy of the secondary sensor in the radial direction on the prediction of the bulk modulus, K. In a realistic

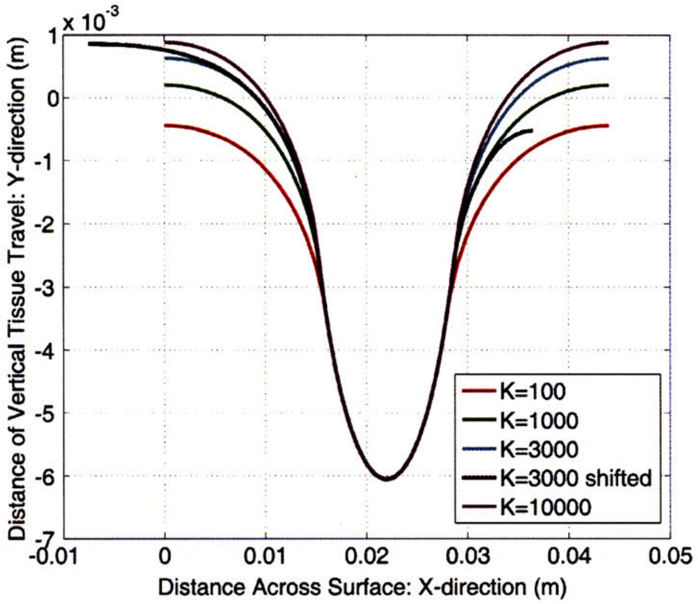

Figure 7-26: The sensitivity of the bulk respose of the material as indicated by the distance of vertical surface travel to location of the sensor in the radial direction

setting, with manufacturing tolerances for the placement of the secondary sensor, it is important to verify that this simulated concept can be used. To do this, a series of indentation with the secondary sensor simulations were performed using the different bulk moduli. The results of this study is given in Figure 7-26. Because this is a theoretical study, these simulations were done in an axisymmetric setup where the indenter was placed at the center of the material. To show the effect of adding the "shift" of the specimen dish with respect to the indenter as performed in the experiments, one additional simulation with the "shift" was conducted. The results show that for the different bulk moduli, the vertical surface displacement differences can be differentiated when the secondary sensor is placed at least 7mm away from the indenter. The ability to differentiate between the bulk moduli increases as the secondary sensor is placed further away from the main indenter, as seen by the flattening of the curve. Were the secondary sensor placed in a location close to the indenter, for example at 5mm away, the sensor would not be able to differentiate bulk modulus differences. The simulation that included the "shift" of the specimen dish off axis shows an interesting result as there is a diminishing return on how far away the secondary sensor is placed. In this simulation, placing the secondary sensor 30mm away or 20mm away would result is the same bulk modulus prediction. This is because this specimen is at a small enough diameter and confined to not move in the radial direction, so the resulting motion is almost entirely in the vertical direction. When imagining a realistic scenario where in vivo indentation experiments are conducted, there would also be an upper limit to the distance between the indenter and the secondary sensor where the near field effects of indentation would diminish.

7.3 Three-dimensional model conclusions

This chapter presents the development of a nonlinear hyper-viscoelastic constitutive model for the brain under large deformations. Many others have proposed models [6][15][44][45][49][66][69], and have showed that for their particular set of experiments, the model agrees well with the data. The unique aspect of the model presented in this chapter is that it has demonstrated its ability to predict the large strain, nonlinear and hysteresis response at three rates of deformation, and it can capture the short and long terms stress relaxation response of a representative specimen of tested brain tissue. Additionally, it can predict the lateral strain response of the material when tested in uniaxial unconfined compression.

Chapter 8

Conclusions and Future Work

8.1 Concluding remarks

Performing in vivo experiments on brain tissue can give insight into improved material models used in efforts to understand traumatic brain injury caused by automobile crashes or blast injuries. Characterizing the material behavior of brain tissue remains challenging because the requisite model must describe tissue responses in various modes of deformations, strain levels and and frequency ranges. This characterization is particularly pertinent for brain injuries sustained by dynamic loads in which criteria for damage and injury thresholds for the brain are of great interest. The broader impact of this work is to design against and to better understand the mechanisms that cause injury. To achieve this, realistic material models for critical organs must be developed. The models can then be applied to finite element meshes that contain accurate anatomical geometries, and various loading conditions can be simulated.

To gain more realistic understanding of the behavior of brain tissue, in vivo studies on porcine animal models are often conducted. To measure the response of brain tissue in vivo, a portable DIST tool was designed to operate within a wide range of strains and strain rate levels. The validation of the DIST tool was performed on stable, tissue simulants. Very often, in vivo experiments involve the use of indentation testing, however this method is limited to measuring a single output for a given input. Much information from this single input test is lost by not measuring more interaction effects. To address this opportunity, incorporating an additional sensor that tracks the surface deformation in the near field of the indentation is proposed. The additional sensor provides more insight into the volumetric response of the material. This theory is validated in a simulation study of materials with different volumetric behavior

To develop the appropriate model for the complex nonlinear, time-dependent response of brain tissue, large strain uniaxial compression experiments at multiple loading rates were conducted. Lateral strains were measured and used to understand the volumetric response of the tissue. The appropriate three-dimensional form of the model was selected based on the nonlinear, strain-rate dependent, time-dependent material behavior of the tissue under uniaxial compression loading. Appropriate parameter values were assigned to the model by fitting the model response to the experiment. The same model and parameter values were then assigned to predict the indentation force and secondary sensor displacement response of the material when subject to indentation loading. The predictions are in very good agreement with the actual experiments, leading to the conclusion that the three-dimensional model developed in this work not only captures the peak stress levels and viscous deformation at three different strain rates, but also has the breadth to capture the volumetric response seen by the material. The indentation simulations strengthen the validity of this model by predicting the force-displacement response and the secondary sensor displacement response measured in the indentation experiments. The results indicated a correlation between the measurement of lateral stretch in an unconfined compression experiment and a surface tracking displacement measurement of the material at an offset range away from the main indenter. This measure of lateral stretch or vertical surface displacements give insight into the degree of compressibility of a material tested. This finding becomes very valuable when transitioning the indentation with secondary sensor setup to an in vivo material property tester such as the proposed DIST tool. In vivo testing is not often conducted because experimental setups are complex and approval from animal review boards are difficult to obtain. Therefore, many reseachers focus on in vitro testing of biological materials. The benefit and lure of in vitro testing is that conditions for experimentation can be more controlled using sophisticated equipment and more straightforward specimen preparation, however the shortcomings of this approach is that cell death can lead to altered mechanical behavior of biological tissues. In the scenarios where in vivo material responses are being captured, it is desirable to have as much information about the mechanical test as possible and the proposed design with the secondary sensor addresses this need.

8.2 Recommendations for future work

Future work should include further design iterations on the DIST tool. The control architecture of the DIST tool can be revamped such that the tool can operate in open-loop as well as closed-loop mode. Also, some effort into designing appropriate attachments to house the secondary sensors should be undertaken. The tool development is nearly at the level where it can be used in the animal lab setting, however these few modifications need to be done. Secondly, more indentation experiments using the secondary sensor to track the surface deformations need to be conducted. A statistically significant number of samples must be tested and obtained within the same experimental conditions including post-mortem time and specimen preparation. The experiment performed gives a very compelling proof of concept, however further investigation is needed to gain confidence in the method. Another aspect of experimentation that could be further developed is expanding the concept of the secondary sensors to include multiple sensors at different distances away from the main indenter. This proposed design could provide even greater insight into the behavior of the tissue as multiple outputs for a single input could help further characterize the material. Finally, there is opportunity to improve the three-dimensional material model presented in this work. The pre-conditioned model with nine parameters lays a very good framework for the simulations, however the additional network to capture the conditioning effect can be more elegantly incorporated by eliminating this second conditioning network and replacing it with a term modeling the fluid diffusion into and out of the tissue.

Bibliography

[1] A Al-Bsharat, C Zhou, KH Yang, T Khalil, and AI King. Intracranial pressure in the human head due to frontal impact based on a" finite element model. *Proceedings of ASME Summer Bioengineering Meeting* page 159 (1999).

[2] KB Arbogast and SS Margulies. Material characterization of the brainstem from oscillatory shear tests. *J Biomech* **31**(9), 801–7 (1998).

[3] FA Bandak and RH Eppinger. A three-dimensional finite element analysis of the human brain under combined rotational and translational accelerations. *SAE transactions* **103**(6), 1708–1726 (1994).

[4] M Bengisu. "Engineering Ceramics." Springer (2001).

[5] JS Bergstrom and MC Boyce. Constitutive modeling of the large strain time-dependent behavior of elastomers. *J Mech Phys Sol* **46**(5), 931–954 (1998).

[6] LE Bilston. Large strain behaviour of brain tissue in shear: Some experimental data and differential constitutive model. *Biorheology* **38**(4), 335–345 (2001).

[7] JE Bischoff, EM Arruda, and K Grosh. Constitutive modeling of human skin allowing for anisotropy andgrowth. *Eng Med Biol* **1** (1999).

[8] M Bolduc and S Tylko. Hybrid III head response of an undefeated combat helmet in a ballistic environment. *Proceedings of the 2nd meeting of the NATO Task Group: Behind Armour Blunt Trauma* (2003).

[9] G Bolzon, G Maier, and M Panico. Material model calibration by indentation, imprint mapping and inverse analysis. *Intl J Solids Struct* **41**, 2957–2975 (2004).

[10] DWA Brands, GWM Peters, and PHM Bovendeerd. Design and numerical implementation of a 3-D non-linear viscoelastic constitutive model for brain tissue during impact. *J Biomech* **37**(1), 127–134 (2004).

[11] M Bro-Nielsen. Finite element modeling in surgery simulation. *Proceedings of the IEEE* **86**(3), 490–503 (1998).

[12] L Cheng, X Xia, W Yu, LE Scriven, and WW Gerberich. Flat-punch indentation of viscoelastic material. *J Polym Sci Pol Phys* **38**(1), 10–22 (2000).

[13] S Cheng and LE Bilston. Unconfined compression of white matter. *J Biomech* **40**(1), 117–124 (2007).

[14] M Claessens, F Sauren, and J Wismans. Modeling of the human head under impact conditions: A parametric study. *SAE transactions* **106**(6), 3829–3848 (1997).

[15] KK Darvish and JR Crandall. Nonlinear viscoelastic effects in oscillatory shear deformation of brain tissue. *Med Eng Phys* **23**(9), 633–45 (2001).

[16] C Davatzikos, D Shen, A Mohamed, and SK Kyriacou. A framework for predictive modeling of anatomical deformations. *IEEE T Med Imaging* **20**(8), 836–843 (2001).

[17] BR Donnelly and J Medige. Shear properties of human brain tissue. *J Biomech Eng* **119**(4), 423–32 (1997).

[18] PJ Edwards, DL Hill, JA Little, and DJ Hawkes. A three-component deformation model for image-guided surgery. *Med Image Anal* **2**(4), 355–67 (1998).

[19] T El-Aguizy, JS Plante, AH Slocum, and JD Vogan. Frictionless compression testing using load-applying platens made from porous graphite aerostatic bearings. *Rev Sci Instrum* **76**, 075108 (2005).

[20] MS Estes and JH McElhaney. Response of brain tissue of compressive loading. *ASME Paper* **70**, 1–4 (1970).

[21] GT Fallenstein, VD Hulce, and JW Melvin. Dynamic mechanical properties of human brain tissue. *J Biomech* **1969**, 217–26 (2003).

[22] SR FINFER AND J COHEN. Severe traumatic brain injury. *Resuscitation* **48**(1), 77–90 (2001).

[23] WP FLETCHER AND AN GENT. Non-Linearity in the Dynamic Properties of Vulcanised Rubber Compounds. *IRI Transactions* **29**, 266–280 (1953).

[24] JE GALFORD AND JH MCELHANEY. A viscoelastic study of scalp, brain, and dura. *J Biomech* **3**(2), 211–21 (1970).

[25] A GEFEN, N GEFEN, Q ZHU, R RAGHUPATHI, AND SS MARGULIES. Age-Dependent Changes in Material Properties of the Brain and Braincase of the Rat. *J Neurotraum* **20**(11), 1163–1177 (2003).

[26] A GEFEN AND SS MARGULIES. Are in vivo and in situ brain tissues mechanically similar. *J Biomech* **37**, 1339–1352 (2004).

[27] A GOULDSTONE, N CHOLLACOOP, M DAO, J LI, AND AM MINOR. Indentation across size scales and disciplines: Recent developments. *Acta Matera* **55**(12), 4015–4039 (2006).

[28] AS GURDJIAN AND JE WEBSTER. "Head Injuries: Mechanisms, Diagnosis, and Management". Churchill (1958).

[29] HIBBIT. "ABAQUS/Standard 6.4 User's Manual". Hibbitt and Karlsson and Sorenesen, Inc. (2004).

[30] R HICKLING AND ML WENNER. Mathematical model of a head subjected to an axisymmetric impact. *J Biomech* **6**(2), 115–32 (1973).

[31] G HUANG AND H LU. Measurements of Two Independent Viscoelastic Functions by Nanoindentation. *Exp Mech* **47**(1), 87–98 (2007).

[32] G HUANG, B WANG, AND H LU. Measurements of Viscoelastic Functions of Polymers in the Frequency-Domain Using Nanoindentation. *Mech Time-Depend Mat* **8**(4), 345–364 (2004).

[33] FA JOLESZ. Image-guided procedures and the operating room of the future. *Radiology* **204**(3), 601–612 (1997).

[34] D Kalanovic, MP Ottensmeyer, J Gross, G Buess, and SL Dawson. Independent testing of soft tissue visco-elasticity using indentation and rotary shear deformations. *Proc. MMVR* **11** (2003).

[35] AE Kerdok, SM Cotin, MP Ottensmeyer, AM Galea, RD Howe, and SL Dawson. Truth cube: Establishing physical standards for soft tissue simulation. *Med Imag Anal* **7**(3), 283–291 (2003).

[36] AE Kerdok, MP Ottensmeyer, and RD Howe. Effects of perfusion on the viscoelastic characteristics of liver. *J Biomech* **39**(12), 2221–2231 (2006).

[37] S Kleiven and WN Hardy. Correlation of an FE Model of the Human Head with Experiments on Localized Motion of the Brain–Consequences for Injury Prediction. *46th Stapp Car Crash Journal* (2002).

[38] W Kuhn and Gruhn F. Beziehungen zwischen elastischen konstanten und dehnungsdoppelbrechung hochelastischer stoffe. *Kolloid-Z* **101**, 248–271 (1942).

[39] LP Li and W Herzog. Arthroscopic evaluation of cartilage degeneration using indentation testing Ű influence of indenter geometery. *Clin Biomech)* **21**, 420–426 (2006).

[40] H Lu, B Wang, J Ma, G Huang, and H Viswanathan. Measurement of Creep Compliance of Solid Polymers by Nanoindentation. *Mecha Time-Depend Mat* **7**(3), 189–207 (2003).

[41] BN Lucas, JC Hay, and WC Oliver. Using multidimensional contact mechanics experiments to measure PoissonŠs ratio. *J Mater Res* **19**(1), 58–65 (2004).

[42] KE Lunn, KD Paulsen, DR Lynch, DW Roberts, FE Kennedy, and A Hartov. Assimilating intraoperative data with brain shift modeling using the adjoint equations. *Med Image Anal* **9**(3), 281–93 (2005).

[43] JH McElhaney, JL Fogle, JW Melvin, RR Haynes, VL Roberts, and NM Alem. Mechanical properties on cranial bone. *J Biomech* **3**(5), 495–511 (1970).

[44] DF Meaney. Relationship between structural modeling and hyperelastic material behavior: application to CNS white matter. *Biomech Model Mechan* **1**(4), 279–293 (2003).

[45] KK Mendis, RL Stalnaker, and SH Advani. A constitutive relationship for large deformation finite element modeling of brain tissue. *J Biomech Eng* **117**(3), 279–85 (1995).

[46] H Metz, J McElhaney, and AK Ommaya. A comparison of the elasticity of live, dead, and fixed brain tissue. *J Biomech* **3**(4), 453–8 (1970).

[47] K Miller. Biomechanics of soft tissues. *Med Sci Monit* **6**(1), 158–67 (2000).

[48] K Miller. Method of testing very soft biological tissues in compression. *J Biomech* **38**(1), 153–158 (2005).

[49] K Miller and K Chinzei. Constitutive modelling of brain tissue: experiment and theory. *J Biomech* **30**(11-12), 1115–21 (1997).

[50] K Miller and K Chinzei. Mechanical properties of brain tissue in tension. *J Biomech* **35**(4), 483–490 (2002).

[51] K Miller, K Chinzei, G Orssengo, and P Bednarz. Mechanical properties of brain tissue in-vivo: experiment and computer simulation. *J Biomech* **33**(11), 1369–1376 (2000).

[52] Huber N, Konstandinidis A, and Tsakmakis Ch. Determination of Poisson's ratio by spherical indentation using neural networks. Part I: Theory. *J Appl Mech* **68**, 218–223 (2001).

[53] Huber N, Konstandinidis A, and Tsakmakis Ch. Determination of Poisson's ratio by spherical indentation using neural networks. Part II: Indentation Method. *J Appl Mech* **68**, 224–229 (2001).

[54] A Nabavi, PM Black, DT Gering, CF Westin, V Mehta, RS Pergolizzi, M Ferrant, SK Warfield, N Hata, RB Schwartz, et al.. Serial intraoperative magnetic resonance imaging of brain shift. *Neurosurgery* **48**(4), 787–798 (2001).

[55] A Nava, E Mazza, F Kleinermann, N Avis, and J McClure. Determination of the mechanical properties of soft human tissues through aspiration experiments. *MICCAI 2003* (2003).

[56] S Nicolle. Shear linear behavior of brain tissue over a large frequency range. *Biorheology* **42**(3), 209–223 (2005).

[57] C Nimsky, O Ganslandt, S Cerny, P Hastreiter, G Greiner, and R Fahlbusch. Quantification of, visualization of, and compensation for brain shift using intraoperative magnetic resonance imaging. *Neurosurgery* **47**(5), 1070–1079 (2000).

[58] GM Odegard, TS Gates, and HM Herring. Characterization of viscoelastic properties of polymeric materials through nanoindentation. *Exp Mech* **45**(2), 130–136 (2005).

[59] WC Oliver and GM Pharr. Improved technique for deternining hardness and elastic modulus using load and displacement sensing indentation experiments. *J Mater Res* **7**(6), 1564–1583 (1992).

[60] WC Oliver and GM Pharr. Measurement of hardness and elastic modulus by instrumented indentation: Advances in understanding and refinements to methodology. *J Mater Res* **19**(1), 3–20 (2004).

[61] AK Ommaya, AE Hirsch, and JL Martinez. The role of whiplash in cerebral concussion. *Proceedings of the 10th Stapp Car Crash Conference* pages 8–9 (1966).

[62] MP Ottensmeyer. An instrument for measuring solid organ soft tissue properties. *Exp Techniques* **26**, 48–50 (2002).

[63] MP Ottensmeyer and KJ Salisbury. In vivo data acquisition instrument for solid organ mechanical property measurement. *MICCAI 2001* pages 975–982 (2001).

[64] MR Pamidi and SH Advani. Nonlinear constitutive relations for human brain tissue. *J Biomech Eng* **100**, 44–48 (1978).

[65] G Peters, H Meulman, and A Sauren. Application of the time temperature superposition theory on brain tissue. *Biorheology* **34**, 127–138 (1997).

[66] MT Prange and SS Margulies. Regional, directional, and age-dependent properties of the brain undergoing large deformation. *J Biomech Eng* **124**, 244 (2002).

[67] HJ Qi, K Joybe, and MC Boyce. Durometer hardness and the stress-strain behavior of elastomeric materials. *Rubber Chem Technol* **76**(2), 419–435 (2003).

[68] JS Ruan, TB Khalil, and AI King. Finite Element Modeling of Direct Head Impact. *SAE International* (1993).

[69] F Shen, TE Tay, JZ Li, S Nigen, PVS Lee, and HK Chan. Modified Bilston Nonlinear Viscoelastic Model for Finite Element Head Injury Studies. *J Biomech Eng* **128**, 797 (2006).

[70] LZ Shuck and SH Advani. Rheological response of human brain tissue in shear. *J Basic Eng-T ASME* **94**, 905–911 (1972).

[71] AH Slocum. "Precision machine design". Prentice Hall Englewood Cliffs, NJ (1992).

[72] RL Spilker, JK Suh, and VC Mow. A finite element analysis of the indentation stress-relaxation response of linear biphasic articular cartilage. *J Biomech Eng* **114**(2), 191–201 (1992).

[73] RL Stalnaker. "Mechanical properties of the head". PhD Dissertation, West Virginia University, 2 edition (1969).

[74] D Tabor. "The Hardness of Metals". Oxford University Press (2000).

[75] EG Takhounts, JR Crandall, and K Darvish. On the Importance of Nonlinearity of Brain Tissue Under Large Deformations. *Stapp Car Crash* **47**, 79–92 (2003).

[76] EG Takhounts, RH Eppinger, JQ Campbell, RE Tannous, ED Power, and LS Shook. On the Development of the SIMon Finite Element Head Model. *Stapp Car Crash* **47**, 107–133 (2003).

[77] PA Taylor and CC Ford. Simulation of head impact leading to traumatic brain injury. *Army Science Conference* (2006).

[78] KL Thibault and SS Margulies. Age-dependent material properties of the porcine cerebrum: effect on pediatric inertial head injury criteria. *J Biomech* **31**(12), 1119–26 (1998).

[79] R VAIDYANATHAN, M DAO, G RAVICHANDRAN, AND S SURESH. Study of mechanical deformation in bulk metallic glass through instrumented indentation. *Acta Mater* **49**(16), 3781–3789 (2001).

[80] D VALTORTA AND E MAZZA. Measurement of rheological properties of soft biological tissue with a novel torsional resonator device. *Rheologica Acta* **45**(5), 677–692 (2006).

[81] WM VANNAH AND DS CHILDRESS. Indentor tests and finite element modeling of bulk muscular tissue in vivo. *Development* **33**(3), 239–252 (1996).

[82] IM WARD AND J. SWEENEY. "An Introduction to the Mechanical Properties of Solid Polymers". John Wiley and Sons (2004).

[83] SK WARFIELD, F TALOS, A TEI, A BHARATHA, A NABAVI, M FERRANT, P McL BLACK, FA JOLESZ, AND R KIKINIS. Real-time registration of volumetric brain MRI by biomechanical simulation of deformation during image guided neurosurgery. *Comput Visual Sc* **5**(1), 3–11 (2002).

[84] MD WARNER, WR TAYLOR, AND SE CLIFT. Finite element biphasic indentation of cartilage: a comparison of experimental indenter and physiological contact geometries. *Proceedings of the Institution of Mechanical Engineers, Part H: Journal of Engineering in Medicine* **215**(5), 487–496 (2001).

[85] RJ WAXWEILER, D THURMAN, J SNIEZEK, D SOSIN, AND J O'NEIL. Monitoring the impact of traumatic brain injury: a review and update. *J Neurotraum* **12**(4), 509–16 (1995).

[86] DG WEIGHT. Minor head trauma. *Psychiatr Clin North Am* **21**(3), 609–24 (1998).

[87] R WILLINGER AND D BAUMGARTNER. Human head tolerance limits to specific injury mechanisms. *Int J Crashworthines* **8**(6), 605–617 (2003).

[88] JZ WU, W HERZOG, AND M EPSTEIN. Evaluation of the finite element software ABAQUS for biomechanical modelling of biphasic tissues. *J Biomech* **31**(2), 165–9 (1998).

[89] L ZHANG, KH YANG, AND AI KING. A Proposed Injury Threshold for Mild Traumatic Brain Injury. *J Biomech Eng* **126**, 226 (2004).

[90] LY ZHANG, W. HARDY, K. OMORI, K.H. YANG, AND A.I. KING. Recent advances in brain injury research: a new model and new experimental data. *Proc Bioeng Conf* **50**, 833–834 (2001).

[91] C ZHOU, TB KHALIL, AND AI KING. A new model comparing impact responses of the homogeneous and inhomogeneous human brain. *Proc 39th Stapp Car Crash Conference* **SAE Paper 952714** (1995).